The Galaxies Missed by Hubble and ALMA: The Contribution of Extremely Red Galaxies to the Cosmic Census at $3 < z < 8$

Christina C. Williams[1,2], Stacey Alberts[2], Zhiyuan Ji[2], Kevin N. Hainline[2], Jianwei Lyu[2], George Rieke[2,3], Ryan Endsley[4], Katherine A. Suess[5,6], Fengwu Sun[2], Benjamin D. Johnson[7], Michael Florian[2], Irene Shivaei[8], Wiphu Rujopakarn[9,10], William M. Baker[11,12], Rachana Bhatawdekar[13], Kristan Boyett[14,15], Andrew J. Bunker[16], Alex J. Cameron[16], Stefano Carniani[17], Stephane Charlot[18], Emma Curtis-Lake[19], Christa DeCoursey[2], Anna de Graaff[20], Eiichi Egami[2], Daniel J. Eisenstein[7], Justus L. Gibson[21], Ryan Hausen[22], Jakob M. Helton[2], Roberto Maiolino[11,12], Michael V. Maseda[23], Erica J. Nelson[21], Pablo G. Pérez-González[8], Marcia J. Rieke[2], Brant E. Robertson[5], Aayush Saxena[16,24], Sandro Tacchella[11,12], Christopher N. A. Willmer[2], and Chris J. Willott[25]

[1] NSF's National Optical-Infrared Astronomy Research Laboratory, 950 North Cherry Avenue, Tucson, AZ 85719, USA; christina.williams@noirlab.edu
[2] Steward Observatory, University of Arizona, 933 North Cherry Avenue, Tucson, AZ 85721, USA
[3] Dept of Planetary Sciences, University of Arizona, 933 North Cherry Avenue, Tucson, AZ 85721, USA
[4] Department of Astronomy, University of Texas, Austin, TX 78712, USA
[5] Department of Astronomy and Astrophysics, University of California, Santa Cruz, 1156 High Street, Santa Cruz, CA 95064, USA
[6] Kavli Institute for Particle Astrophysics and Cosmology and Department of Physics, Stanford University, Stanford, CA 94305, USA
[7] Center for Astrophysics | Harvard & Smithsonian, 60 Garden Street, Cambridge, MA 02138, USA
[8] Centro de Astrobiología (CAB), CSIC-INTA, Ctra. de Ajalvir km 4, Torrejón de Ardoz, E-28850 Madrid, Spain
[9] National Astronomical Research Institute of Thailand, Don Kaeo, Mae Rim, Chiang Mai 50180, Thailand
[10] Department of Physics, Faculty of Science, Chulalongkorn University, 254 Phayathai Road, Pathumwan, Bangkok 10330, Thailand
[11] Kavli Institute for Cosmology, University of Cambridge, Madingley Road, Cambridge, CB3 0HA, UK
[12] Cavendish Laboratory, University of Cambridge, 19 JJ Thomson Avenue, Cambridge, CB3 0HE, UK
[13] European Space Agency (ESA), European Space Astronomy Centre (ESAC), Camino Bajo del Castillo s/n, 28692 Villanueva de la Cañada, Madrid, Spain
[14] School of Physics, University of Melbourne, Parkville, 3010 VIC, Australia
[15] ARC Centre of Excellence for All Sky Astrophysics in 3 Dimensions (ASTRO 3D), Australia
[16] Department of Physics, University of Oxford, Denys Wilkinson Building, Keble Road, Oxford OX1 3RH, UK
[17] Scuola Normale Superiore, Piazza dei Cavalieri 7, I-56126 Pisa, Italy
[18] Sorbonne Université, CNRS, UMR 7095, Institut d'Astrophysique de Paris, 98 bis bd Arago, 75014 Paris, France
[19] Centre for Astrophysics Research, Department of Physics, Astronomy and Mathematics, University of Hertfordshire, Hatfield AL10 9AB, UK
[20] Max-Planck-Institut für Astronomie, Königstuhl 17, D-69117, Heidelberg, Germany
[21] Department for Astrophysical and Planetary Science, University of Colorado, Boulder, CO 80309, USA
[22] Department of Physics and Astronomy, The Johns Hopkins University, 3400 N. Charles St., Baltimore, MD 21218, USA
[23] Department of Astronomy, University of Wisconsin-Madison, 475 N. Charter St., Madison, WI 53706, USA
[24] Department of Physics and Astronomy, University College London, Gower Street, London WC1E 6BT, UK
[25] NRC Herzberg, 5071 West Saanich Rd, Victoria, BC V9E 2E7, Canada

Abstract

Using deep JWST imaging from JADES, JEMS, and SMILES, we characterize optically faint and extremely red galaxies at $z > 3$ that were previously missing from galaxy census estimates. The data indicate the existence of abundant, dusty, and poststarburst-like galaxies down to $10^8\ M_\odot$, below the sensitivity limit of Spitzer and the Atacama Large Millimeter/submillimeter Array (ALMA). Modeling the NIRCam and Hubble Space Telescope (HST) photometry of these red sources can result in extremely high values for both stellar mass and star formation rate (SFR); however, including seven MIRI filters out to 21 μm results in decreased masses (median 0.6 dex for $\log_{10}(M^*/M_\odot) > 10$) and SFRs (median $10\times$ for SFR $> 100\ M_\odot$ yr^{-1}). At $z > 6$, our sample includes a high fraction of "little red dots" (LRDs; NIRCam-selected dust-reddened active galactic nucleus (AGN) candidates). We significantly measure older stellar populations in the LRDs out to rest-frame 3 μm (the stellar bump) and rule out a dominant contribution from hot dust emission, a signature of AGN contamination to stellar population measurements. This allows us to measure their contribution to the cosmic census at $z > 3$, below the typical detection limits of ALMA ($L_{IR} < 10^{12}\ L_\odot$). We find that these sources, which are overwhelmingly missed by HST and ALMA, could effectively double the obscured fraction of the star formation rate density at $4 < z < 6$ compared to some estimates, showing that prior to JWST, the obscured contribution from fainter sources could be underestimated. Finally, we identify five sources with evidence for Balmer breaks and high stellar masses at $5.5 < z < 7.7$. While spectroscopy is required to determine their nature, we discuss possible measurement systematics to explore with future data.

Unified Astronomy Thesaurus concepts: High-redshift galaxies (734); Active galaxies (17); AGN host galaxies (2017)

1. Introduction

Our picture of galaxy formation and growth during the first 2 billion years of the Universe is, currently, an incomplete one. The Hubble Space Telescope (HST) is only sensitive to the

rest-frame ultraviolet (UV) light for galaxies at $z > 3$, which at "Cosmic Noon" $(1 < z < 3)$, is known to miss the overwhelming majority of star formation activity and energy output from galaxies due to dust obscuration (e.g., Madau & Dickinson 2014). While the addition of submillimeter and radio measurements has greatly improved our understanding of the star formation census at Cosmic Noon (e.g., Hodge & da Cunha 2020), the difficulty in making these measurements increases dramatically at $z > 3$. This is in part due to a decline in the abundance of the bright, submillimeter galaxies that are detectable by wide-area submillimeter surveys (e.g., Simpson et al. 2014; Brisbin et al. 2017; Danielson et al. 2017; Dudzevičiūtė et al. 2020; Casey et al. 2021). It is also in part because of the large uncertainty in the abundance of more common, but less extreme galaxies, that are below the detection limits of typical multiwavelength surveys (and difficulties in determining their counterparts and redshifts; e.g., Smail et al. 2021). As the abundance of massive galaxies declines, less massive and fainter sources (e.g., Pope et al. 2017, 2023) could plausibly harbor an increasing fraction of the obscured star formation at early times. Progress has been made by identifying fainter, dusty galaxies with ever increasing Atacama Large Millimeter/submillimeter Array (ALMA) area (in particular using longer-wavelength, >2–3 mm selections to filter out lower-redshift sources; Béthermin et al. 2015; Casey et al. 2021; Cooper et al. 2022). Despite these advances, recent ALMA-based estimates at $z > 4$ still rely on relatively few detections, strong lensing, or extrapolations of the infrared luminosity function (e.g., Zavala et al. 2021; Algera et al. 2023; Barrufet et al. 2023a; Fujimoto et al. 2023a; Traina et al. 2024). Uniform and large-area surveys are still needed for unbiased samples, and remain challenging with ALMA's small field of view. Thus, the pre-JWST census of galaxies in the first 2 Gyr of cosmic history remained highly biased to relatively unobscured, star-forming sources. A complete understanding of the evolution of the early Universe requires accurate accounting of the abundance, the growth rate, and the energy output from a complete and unbiased census of the galaxy population.

Prior to the launch of JWST (Gardner et al. 2023), observations at the limit of Spitzer Space Telescope and ALMA capabilities indicated the existence of surprisingly abundant, massive galaxies that are very red, enough so to evade HST selection. Some of these massive galaxies are serendipitously identified at submillimeter wavelengths to faint limits, thanks to ALMA's extremely sensitive receivers (otherwise lacking counterparts at shorter wavelengths; i.e., optical/near-infrared faint, or "dark"). Submillimeter or radio sources lacking counterparts have been known for decades and hypothesized to be high redshift (e.g., Hu & Ridgway 1994; Hughes et al. 1998; Dey et al. 1999; Dunlop et al. 2004; Frayer et al. 2004). However, in recent years, ALMA's sensitivity, small field of view, and ever deeper surveys at optical/near-infrared wavelengths suggest that massive, dust-obscured, red galaxies were even more common at high redshift than previously thought (Williams et al. 2019; Umehata et al. 2020; Fudamoto et al. 2021; Sun et al. 2021). The number densities and redshift distributions of these red sources are still highly uncertain, but imply that previous HST surveys might have missed up to 90% of massive galaxies $(\log_{10}(M/M_\odot) > 10.5)$ at $z > 3$ (Wang et al. 2016, 2019). While the idea that the distant Universe may contain abundant

massive galaxies waiting to be discovered is tantalizing, ALMA left many open questions regarding the properties of the stellar populations, morphologies, and potential for these missing galaxies to harbor black holes. These questions remain unanswered without deep near- to mid-infrared data.

The first year of JWST observations has now confirmed the existence of very red galaxies missed by HST. First-look papers indicated that the properties of these sources are consistent with being dusty or quiescent galaxies at $z \sim 3$–7, with some fraction of bluer sources turned red by strong emission lines boosting long-wavelength filters (Barger & Cowie 2023; Barrufet et al. 2023b; Fujimoto et al. 2023b; Endsley et al. 2023; Glazebrook et al. 2023; Pérez-González et al. 2023; Rodighiero et al. 2023; Smail et al. 2023). The new discovery of these red galaxies demonstrated conclusive evidence that HSTs limited wavelength coverage had left us with a critical blind spot.

Interestingly, NIRCam imaging is revealing that distant red and optically faint galaxies are remarkably diverse as a population. In particular, a number of galaxies with peculiar or surprisingly shaped red spectral energy distributions (SEDs) have been discovered. Some SEDs resemble strong Balmer breaks with strong red rest-frame optical continua, leading to high inferred stellar masses despite their early observation times (e.g., Labbé et al. 2023b). Another class exhibits similarities in SED and morphology to highly reddened QSOs (visibly appearing as "little red dots" (LRDs); Furtak et al. 2023; Labbé et al. 2023a). A number of such LRDs have now been spectroscopically confirmed to host some form of active galactic nucleus (AGN) activity (Furtak et al. 2023a; Greene et al. 2023; Harikane et al. 2023; Kocevski et al. 2023; Kokorev et al. 2023; Maiolino et al. 2023; Matthee et al. 2023). Both subclasses raise important questions about how these galaxies and black holes could grow at such fast rates at early cosmic time, and motivate the identification of larger samples with expanded deep panchromatic data.

Among the broader red and massive $z > 3$ galaxy population, some first results have indicated that in fact their abundance has been previously significantly underestimated, with a factor of 20%–25% higher stellar mass density at $3 < z < 6$ and >100% at $6 < z < 8$ (Gottumukkala et al. 2023). This points to an early start to rapid stellar mass growth that is obscured by large dust columns, assuming our extrapolations from $z \sim 0$ stellar population modeling are correct (e.g., Steinhardt et al. 2023; Wang et al. 2023; Woodrum et al. 2023). This could alter the picture of early galaxy growth, requiring an increased efficiency of star formation than previously thought (Labbé et al. 2023b; Xiao et al. 2023a; Boylan-Kolchin 2023). However, further exploration remains to be done, since stellar mass and photometric redshift estimates at high mass and high redshift can also be sensitive to the data set used (e.g., the inclusion of near-infrared medium-band filters; Desprez et al. 2023), thus motivating new exploration also using an expanded wavelength coverage.

With this paper, we provide a detailed look at the SEDs and physical properties of galaxies that were missed by previous surveys using HST, and in many cases even Spitzer and ALMA, primarily due to their extremely red colors and relatively faint fluxes. The goal of this work is to determine what types of galaxies we have been missing and what fraction of the cosmic census has been unaccounted for as a result. This work will focus on a uniformly selected sample of extremely

red sources (JWST/NIRCam 1.5–4.4 μm colors > 2.2) that were previously unaccounted for by HST (fainter than 27 AB mag at 1.5 μm), a criterion that identifies massive and obscured sources primarily at $z > 3$ by bridging the Balmer break at high redshifts (e.g., Caputi et al. 2012; Wang et al. 2016; Barrufet et al. 2023b).

In Sections 2 and 3 we overview the panchromatic data we use in the characterization of these sources. In Sections 4 and 5, we measure the physical properties using SED fitting, revealing both sources with high attenuation and those with older stellar populations and dust-reddened AGN candidates. We also highlight how their extreme colors make it difficult to measure their properties using HST + NIRCam alone, and how the deepest MIRI and ALMA data (only available in this field) can alter the interpretation of these sources. Finally, in Section 6 we characterize their contribution to the galaxy census, identifying what fraction of star formation and stellar mass density was previously missing. We assume a Lambda cold dark matter (ΛCDM) cosmology with $H_0 = 70$ km s^{-1} Mpc^{-1}, $\Omega_M = 0.3$, and $\Omega_\Lambda = 0.7$, and a Kroupa (2001) initial mass function (IMF).

2. Data Sets

In this work, we focus on a select sample of optically faint galaxies identified using JWST/NIRCam imaging inside the Great Observatories Origins Deep Survey South (GOODS-S; Giavalisco et al. 2004), overlapping with the Hubble Ultra Deep Field (HUDF; Beckwith et al. 2006). Given the exceptional ancillary data that are available in this prime region of the sky, we focus on providing a detailed look at this population to give broader insight for larger samples with more limited data. In this section we outline the various data sets we use and our photometric methods used to measure fluxes in each.

2.1. Space-based Data and Photometric Catalog Construction

2.1.1. HST Imaging

In our analysis we include deep optical and near-infrared HST imaging from the Advanced Camera for Surveys (ACS) and Wide Field Camera 3 (WFC3) compiled as the Hubble Legacy Field (HLF; Illingworth et al. 2016; Whitaker et al. 2019, and references therein) imaging in GOODS-S by HST. The HLF represents the deepest composite imaging, including nine filters between 0.4 and 1.6 μm wavelength. We include data from ACS (F435W, F606W, F775W, F814W, and F850LP) and WFC3/IR (F105W, F125W, F140W, and F160W).

2.1.2. JWST NIRCam Imaging

We identify our sample using data from the JWST Advanced Deep Extragalactic Survey (JADES; Eisenstein et al. 2023b). JADES imaging with NIRCam (Rieke et al. 2023a) covers a deep 27 arcmin^2 area that includes nine filters from 0.9–5 μm (F090W, F115W, F150W, F200W, F277W, F335M, F356W, F410M, and F444W) and a medium-depth region covering an additional 40 arcmin^2 area with eight filters (F090W, F115W, F150W, F200W, F277W, F356W, F410M, and F444W). We include another 10 arcmin^2 of NIRCam imaging from the JADES program ID (PID) 1286 (PI: Lutzgendorf) that additionally includes F070W. The deep area also includes the field targeted by the JWST Extragalactic Medium-band Survey

(JEMS; Williams et al. 2023a; PID: 1963; PIs: Williams, Tacchella, and Maseda). JEMS obtained imaging in two $2.'2 \times 2.'2$ regions with five medium-band filters (F182M, F210M, F430M, F460M, and F480M). We also combine our F182M, F210M, and F444W imaging with that obtained as part of the public First Reionization Epoch Spectroscopic COmplete (FRESCO) survey (PI: Oesch; PID: 1895; Oesch et al. 2023). The NIRCam and HST astrometry have been processed with registration to that of Gaia DR2, as described in Whitaker et al. (2019) and our data reduction procedure and astrometric alignment follows the methods outlined in Rieke et al. (2023b) for the JADES data release 1.

2.2. Photometric Catalogs

Also following the methods outlined in the JADES first data release (Rieke et al. 2023b) we measure photometry jointly for the HST and NIRCam imaging based on a detection image constructed as an inverse-variance-weighted stack of the NIRCam long-wavelength filters we have across the entire GOODS-S footprint: F277W, F335M, F356W, F410M, and F444W. Source detection is performed following the deblending algorithms outlined in Rieke et al. (2023b) and B. E. Robertson et al. (2024, in preparation) that utilize `photutils`, `astropy`, `scipy`, `cupy`, and `sextractor` packages. Photometry is measured in circular apertures (on images convolved to the resolution of the F444W filter) for all detected objects. For compact or unresolved sources we use a $0.''5$ diameter aperture, which we validate is the appropriate size by visual inspection. However, by eye we identified a fraction of sources that are more extended than this aperture, and in those cases we instead use a $0.''7$ diameter aperture. To estimate photometric uncertainties, we combine in quadrature the Poisson noise and the noise estimated from the rms of 100,000 random apertures (following the methodology outlined in Labbé et al. 2005; Quadri et al. 2007; Whitaker et al. 2011). We generate aperture corrections to account for flux lost from the fixed apertures using encircled energy curves constructed using WebbPSF (Perrin et al. 2014) as described in Ji et al. (2023).

2.3. Forced Photometry

Once we identify our sample (as will be discussed in Section 3), we also include forced photometry on the following data measured based on the NIRCam positions of our galaxies.

2.3.1. JWST MIRI Imaging

We include wide-field JWST/MIRI (Wright et al. 2023) imaging at 5–25.5 μm from the Systematic Mid-infrared Instrument Legacy Extragalactic Survey (SMILES) program (PID 1207; PI: Rieke), which covers 34 arcmin^2 of the GOODS-S/HUDF region with a nearly complete overlap with JADES and JEMS imaging. For each of the 15 pointings, ~2.2 hr of science time was spread between eight MIRI filters,[26] reaching 5σ point-source sensitivities of 0.20, 0.19, 0.38, 0.59, 0.68, 1.7, 2.8, and 16 μJy for F560W, F770W, F1000W, F1280W, F1500W, F1800W, F2100W, and F2550W, respectively, in apertures containing 65% of the encircled energy for each point-spread function (PSF; see below). The survey

---

[26] F2550W is relatively shallow compared to the other bands and so it is omitted from source photometry for lack of constraining power.

design, data reduction, and source extraction are described in Alberts et al. (2024).[27] Briefly, data reduction was performed using the JWST Calibration Pipeline v1.10.0 (Bushouse et al. 2023) with custom external background subtraction (see Álvarez-Márquez et al. 2023) and astrometry correction matched to the JADES astrometric solution. Flux calibration is updated based on the new reference files released in CRDS jwst_1130.pmap, which include the time-dependent count rate loss (K. Gordon et al. 2024, in preparation). The MIRI astrometry was then registered to NIRCam using an external routine based on `tweakreg` and matched galaxy catalogs (S. Alberts et al. 2024, in preparation).

The blind MIRI photometric catalog is made using the same pipeline as the NIRCam catalog (Rieke et al. 2023b) with the differences that F560W and F770W are stacked for the detection image and the source detection and deblending are optimized for MIRI, given its noise properties and source density. Aperture corrections are applied based on model PSFs from WebbPSF (Perrin et al. 2014) for F1000W–F2550W and with empirical PSFs for F560W and F770W to account for the "cruciform" detector artifact (Gáspár et al. 2021; see Lyu et al. 2024 for more details). The JADES NIRCam sources that also have a blind SMILES MIRI counterpart are then matched within $0\farcs15$. Given MIRI's remarkable sensitivity and well-behaved noise, we also include forced photometric measurements using seven MIRI filters out to 21 μm at the NIRCam positions for sources that are not formally detected in the blind MIRI catalog, in order to enable better constraints on the observed mid-infrared SEDs (rest-frame near-infrared). To perform forced photometry, we use `photutils` to measure flux in circular apertures of size $0\farcs7$ diameter (comparable to the FWHM in F2100W, which balances the higher-resolution MIRI short-wavelength bands against minimizing the aperture corrections in the long-wavelength bands). Our forced photometry is verified by repeating this process on detected sources and comparing to the catalog fluxes, which are found to be in good agreement at the few percent level. To assess the uncertainties, we measured the median flux in boxes at random sourceless locations across the map to get the rms in units of MJy sr^{-1} and then to estimate the rms in the given aperture, we scale by the square root of the aperture area.

2.3.2. ALMA Imaging

Extensive ALMA $\sim$1 mm imaging exists within the JADES region of the GOODS-S field, including some of the deepest contiguous ALMA maps on the sky to date. We take advantage of these ancillary data in order to constrain the far-infrared emission. This critical constraint allows a more robust estimate of the dust-obscured star formation, given the relatively featureless power-law SEDs in the rest-frame optical and faintness in the rest-fame UV. In cases where galaxies are significantly detected at 1 mm in either deep ASAGAO imaging (Hatsukade et al. 2018) or the wider-area GOODS-ALMA program (Franco et al. 2018) we use the published total fluxes in our SED modeling.

For cases where galaxies are not detected in any of the available ALMA imaging, the deep data still provide strong constraints on the limiting far-infrared luminosity associated with the galaxies. To incorporate these deep ALMA limits as

constraints in our SED modeling, we perform forced photometry at the locations of our NIRCam detections using the deepest available map at each source's position. The data we use for our analysis include the deep combined map built by the ASAGAO team (Hatsukade et al. 2018) combined with data from the deep HUDF ALMA footprint (Dunlop et al. 2017) and overlapping coverage from the shallower, but much wider GOODS-ALMA program (Franco et al. 2018; Gómez-Guijarro et al. 2022). Astrometric agreement between these ALMA data sets and Gaia (used as a baseline for the HST and JWST data) has been performed in Franco et al. (2018) and Whitaker et al. (2019) and found to be in excellent agreement. We prioritize the combined map from Hatsukade et al. (2018) if objects appear in multiple data sets, and provide GOODS-ALMA limits (map $\sigma_{\rm rms} \sim 180\ \mu$Jy beam^{-1}) for the objects outside the ASAGAO coverage.

The resolution of the combined ALMA data is relatively high (beam size $\sim 0\farcs5 \times 0\farcs5$ FWHM), similar in size to our NIRCam photometric aperture (Hatsukade et al. 2018). Without knowledge of the actual size of our sources at far-infrared wavelengths, to ensure we include any extended flux, we perform forced aperture photometry at the location of the NIRCam centroid, using a $1\farcs0$ diameter. To perform forced photometry on the ALMA data, we broadly follow the methodology of Betti et al. (2019), Sun et al. (2021), and Shivaei et al. (2022). In short, we multiply the map units (flux beam^{-1}) by the number of pixels per beam, and use `photutils` (Bradley et al. 2022) to measure the flux within a circular aperture of $1\farcs0$ diameter from the primary-beam-corrected map. We assess the uncertainty as the standard deviation of the fluxes within 100 randomly placed apertures within $30''$ distance from the NIRCam source. Where the source is within $30''$ of the edge of the mosaic, we decrease this distance to $15''$, and do not assess forced photometry for sources closer than $15''$ to the edge of the map.

2.3.3. JWST Spectroscopy

For this work, we crossmatch the samples we select in Section 3 with available spectroscopy from JWST. We make use of the public spectroscopic confirmations released by the JADES-NIRSpec program (Bunker et al. 2023; Eisenstein et al. 2023a). We also use data from the FRESCO survey (PI: Oesch; PID: 1895; Oesch et al. 2023), which obtained 4 μm NIRCam wide-field slitless spectroscopy. We will discuss these further in Section 4.1.

3. Color Selection of Targets

In this paper we target extremely red sources at $z > 3$ that would have been missed by typical pre-JWST surveys given wavelength coverage and detection limits. To build an inclusive sample of red sources, we adopt a selection based on the HST/WFC3 F160W – Spitzer 4.5 μm colors ($H - [4.5] > 2.3$; e.g., Caputi et al. 2012; Wang et al. 2016, 2019). Due to redshifting of the Balmer break beyond 1.5 μm at $z > 3$, this selection targets massive and red (including both dust obscured and quiescent) high-redshift galaxy candidates. At the typical detection limits of HST, such galaxies were referred to as "H-band dropouts" (i.e., because they are red, and often not detected by HST; see Wang et al. 2019). For this work, we adopt a comparable selection based on JWST/NIRCam colors F150W – F444W > 2.2, slightly less

---

[27] Point source sensitivities differ slightly from Lyu et al. (2024) due to the updated flux calibrations used here.
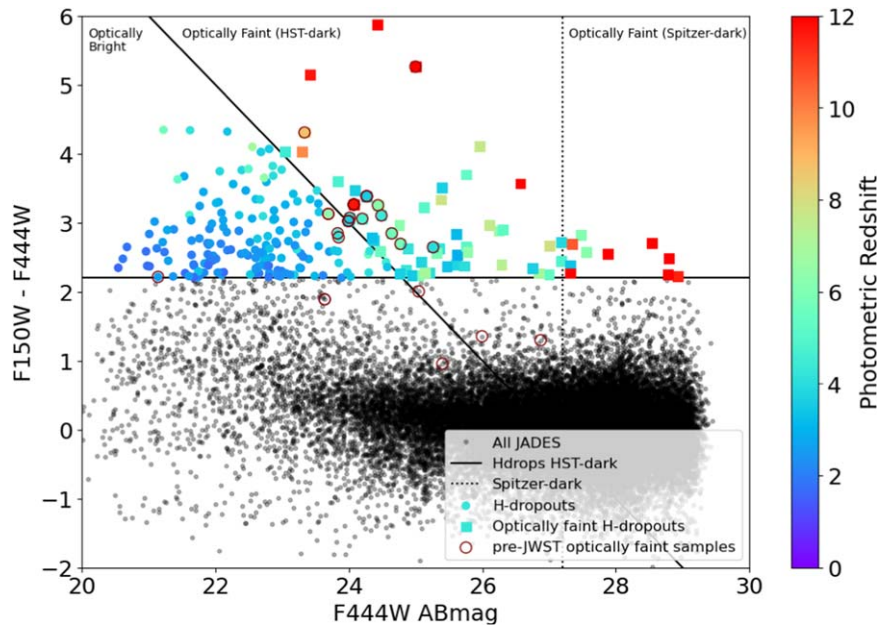
Figure 1. F150W – F444W color vs. F444W magnitude illustrating our selection from the JADES catalog with S/N > 20 in F444W (black points). We identify very red sources by their F150W – F444W > 2.2 color (all colored points) color coded by their EAZY photometric redshift. We further identify the optically fainter sample whose colors and magnitudes are consistent with z > 3 massive galaxies that were absent from earlier HST-selected samples (i.e., have F150W < 27 AB mag: the black diagonal line). In this work, we focus on the optically faint sources behind the black line marked as colored squares. Existing samples of optically faint objects (maroon open circles) are collected from the literature using pre-JWST data sets (Wang et al. 2016; Franco et al. 2018; Alcalde Pampliega et al. 2019; Wang et al. 2019; Xiao et al. 2023b). We note the detection limit of the Spitzer GREATS program (dotted line), indicating newly discovered sources by JWST.

restrictive in order to include existing objects that were identified prior to JWST based on data with larger photometric scatter. Since the first year of GOODS-S imaging from JADES yielded a smaller area coverage in F150W than in F444W, we additionally check for additional *H*-band dropouts using the F160W imaging for which we have imaging in the other NIRCam filters. We identify two additional sources which happen to fall off of our F150W footprint, but that otherwise have nearly complete NIRCam and MIRI imaging.

We present our red sources in F150W – F444W versus F444W magnitude space in Figure 1, color coded by their initial photometric redshifts measured with EAZY (see Section 4.1), along with all significant JADES NIRCam detections (black). This figure highlights the relative rarity of galaxies with this extreme red color compared to the full JADES sample, especially at the fainter F444W magnitudes (which can be seen to roughly correspond to higher-redshift sources based on the EAZY color coding). After visual inspection to remove imaging artifacts and hot pixels, our selection identifies a parent sample of 240 red galaxies across redshifts, that are both F150W – F444W > 2.2 and have a F444W signal-to-noise ratio (S/N) >20 (all colored points in Figure 1).

Following Barrufet et al. (2023b), we retain the F150W-faint sample for the primary analysis of this paper, which roughly corresponds to a redshift selection (see their Figure 1) to identify the primary targets of our study: those with an F150W magnitude fainter than 27 (the dashed diagonal line), which are sources that are below the typical detection limit of HST/F160W in GOODS-S. We will refer to this primary sample, following the convention in the literature, as "HST dark," of which we identify 66 candidate objects (colored squares in Figure 1). Additionally, we note that ~20% of those sources are also below the detection limit of the deepest Spitzer 3.6 and

4.5 μm imaging to date from the GREATS program (Labbé et al. 2015), which reached a 3σ limiting depth of 27.2 (AB magnitude). *H*-band dropouts rightward of this limit (dotted vertical line) represent galaxies that are newly discovered by JWST.

Our HST-dark sources are listed in Tables 1 and 2. NIRCam cutouts of our sample, along with the aperture used to measure their photometry, are shown in Figure 11. The corresponding HST F160W imaging is also shown.

The sample we target is very red in rest-frame optical, exhibiting significant overlap in color space with very late-type stars. Thus, we check whether any of our objects are both unresolved and have F115W, F150W, F277W, and F444W colors that look like red stellar sources (e.g., brown dwarfs with effective temperatures <1500 K) and are poorly fit with stellar population synthesis models, yet are well fit by Sonora Cholla substellar atmosphere models (Marley et al. 2021; Kalaridi et al. 2021; Hainline et al. 2023a). Only one source (ID 190413) is a highly probable brown dwarf candidate based on its colors. This source also has a 0.″62 positional offset measured between GREATS 3.6 μm Spitzer imaging and our JWST data (2σ confidence, given its low S/N in the Spitzer imaging of 5σ, suggesting the positional uncertainty is ~1.″2/5 = 0.″2–0.″3; see Hainline et al. 2023a). This source is additionally poorly fit by stellar population models with a high redshift and improbably high mass solution. Thus, based on the evidence for proper motion, we catalog its properties in Table 1 but remove it from our analysis and census measurements in Sections 5 and 6. The color similarity indicates the uncertainty involved in distinguishing red galaxies at these redshifts from late-type stars (see, e.g., Hainline et al. 2023a; Burgasser et al. 2023).

Our sample has some overlap with a number of red optically faint galaxy populations studied to date with JWST. For

Table 1
Properties of the *H*-band Dropouts That Are Identified inside the MIRI SMILES Footprint

ID[a]	R.A.	Decl.	F444W	Photo-z[b]	Photo-z[c]	Spec-z	$\log_{10}M^{*}$[d]	SFR[e]	A_V[f]	Age[g]	f_{AGN}[h]	LRD[i]
57356	53.115317	−27.859217	25.4	4.24	$5.14^{+0.06}_{-0.04}$	⋯	$10.4^{+0.2}_{-0.6}$	$82.90^{+26.6}_{-17.8}$	$2.57^{+0.35}_{-0.58}$	$0.64^{+0.23}_{-0.32}$	$0.1^{+0.3}_{-0.0}$	0
81400	53.125402	−27.839967	26.6	14.45	$6.17^{+2.28}_{-0.03}$	⋯	$9.5^{+0.2}_{-0.2}$	$31.84^{+8.1}_{-6.2}$	$1.76^{+0.23}_{-0.30}$	$0.12^{+0.03}_{-0.04}$	$0.0^{+0.1}_{-0.0}$	0
88481	53.105475	−27.830682	24.6	5.64	$4.69^{+0.06}_{-0.06}$	⋯	$10.0^{+0.1}_{-0.1}$	$123.05^{+8.8}_{-8.6}$	$1.92^{+0.22}_{-0.20}$	$0.15^{+0.12}_{-0.08}$	$0.0^{+0.0}_{-0.0}$	0
90354	53.133825	−27.828256	27.0	7.91	$\cdots^{+0.00}_{-0.00}$	7.87^{k}	$10.1^{+0.2}_{-0.2}$	$8.64^{+8.0}_{-4.5}$	$1.74^{+0.45}_{-0.37}$	$0.39^{+0.10}_{-0.09}$	$0.0^{+0.1}_{-0.0}$	1
104849	53.101881	−27.810949	26.3	5.29	$\cdots^{+0.00}_{-0.00}$	5.12^{k}	$9.1^{+0.3}_{-0.2}$	$23.95^{+5.4}_{-4.4}$	$1.90^{+0.36}_{-0.34}$	$0.15^{+0.13}_{-0.09}$	$0.0^{+0.0}_{-0.0}$	0
106502	53.145292	−27.808668	25.6	2.89	$3.28^{+0.07}_{-0.05}$	⋯	$9.8^{+0.1}_{-0.2}$	$8.26^{+1.7}_{-1.3}$	$1.82^{+0.25}_{-0.31}$	$1.41^{+0.18}_{-0.16}$	$0.0^{+0.1}_{-0.0}$	0
108239	53.160381	−27.806011	25.7	4.04	$4.52^{+0.02}_{-0.02}$	⋯	$9.7^{+0.0}_{-0.0}$	$0.62^{+0.1}_{-0.1}$	$0.02^{+0.02}_{-0.02}$	$1.28^{+0.03}_{-0.04}$	$0.0^{+0.3}_{-0.0}$	0
120484	53.125426	−27.787438	25.8	5.34	$\cdots^{+0.00}_{-0.00}$	5.00^{k}	$9.9^{+0.1}_{-0.2}$	$22.18^{+7.5}_{-5.5}$	$2.00^{+0.17}_{-0.22}$	$0.51^{+0.15}_{-0.24}$	$0.0^{+0.0}_{-0.0}$	0
121710	53.126897	−27.786153	25.4	7.78	$7.74^{+0.04}_{-0.05}$	⋯	$10.5^{+0.1}_{-0.1}$	$3.24^{+2.0}_{-1.9}$	$1.26^{+0.19}_{-0.19}$	$0.49^{+0.06}_{-0.07}$	$0.0^{+0.0}_{-0.0}$	1
122931	53.200550	−27.784925	29.0	16.07	$4.43^{+0.22}_{-0.04}$	⋯	$8.2^{+0.2}_{-0.2}$	$1.66^{+0.9}_{-0.5}$	$1.33^{+0.45}_{-0.31}$	$0.08^{+0.04}_{-0.03}$	$1.4^{+2.3}_{-0.8}$	0
126594	53.144299	−27.779856	27.3	10.64	$\cdots^{+0.00}_{-0.00}$	7.95^{k}	$9.3^{+0.1}_{-0.1}$	$54.94^{+11.6}_{-10.0}$	$2.03^{+0.22}_{-0.24}$	$0.03^{+0.03}_{-0.02}$	$0.0^{+0.3}_{-0.0}$	1
132229	53.203996	−27.772097	26.1	7.56	$\cdots^{+0.00}_{-0.00}$	7.25^{j}	$10.2^{+0.1}_{-0.1}$	$86.00^{+17.1}_{-19.7}$	$2.41^{+0.24}_{-0.22}$	$0.34^{+0.06}_{-0.07}$	$0.0^{+0.0}_{-0.0}$	1
143133	53.147950	−27.759931	27.6	6.20	$6.11^{+0.21}_{-0.26}$	⋯	$9.5^{+0.2}_{-0.3}$	$53.46^{+19.4}_{-14.3}$	$3.05^{+0.40}_{-0.51}$	$0.14^{+0.13}_{-0.08}$	$0.0^{+0.1}_{-0.0}$	1
154428	53.158173	−27.739130	25.8	6.41	$6.25^{+0.00}_{-0.00}$	⋯	$10.0^{+0.1}_{-0.1}$	$95.98^{+10.6}_{-8.9}$	$2.41^{+0.20}_{-0.15}$	$0.31^{+0.07}_{-0.10}$	$0.0^{+0.0}_{-0.0}$	1
179755	53.082131	−27.859873	24.4	3.63	$3.73^{+0.20}_{-0.03}$	⋯	$10.0^{+0.2}_{-0.2}$	$76.81^{+21.3}_{-38.6}$	$1.80^{+0.24}_{-0.62}$	$0.45^{+0.22}_{-0.24}$	$0.0^{+0.1}_{-0.0}$	0
183348	53.082937	−27.855632	27.3	14.35	$3.38^{+0.08}_{-0.05}$	⋯	$8.5^{+0.1}_{-0.1}$	$1.67^{+0.3}_{-0.3}$	$0.77^{+0.09}_{-0.12}$	$0.13^{+0.04}_{-0.04}$	$0.0^{+0.1}_{-0.0}$	0
184838	53.096419	−27.853090	27.0	5.33	$\cdots^{+0.00}_{-0.00}$	5.38^{k}	$9.5^{+0.2}_{-0.3}$	$49.91^{+11.0}_{-8.9}$	$2.82^{+0.72}_{-0.35}$	$0.17^{+0.17}_{-0.12}$	$0.0^{+0.0}_{-0.0}$	0
189489	53.173662	−27.841913	24.9	4.19	$4.15^{+0.09}_{-0.08}$	⋯	$10.1^{+0.1}_{-0.2}$	$57.72^{+11.8}_{-10.1}$	$1.92^{+0.17}_{-0.18}$	$0.60^{+0.18}_{-0.19}$	$0.0^{+0.0}_{-0.0}$	0
189494	53.162966	−27.841946	24.5	4.34	$4.50^{+0.06}_{-0.05}$	⋯	$10.4^{+0.1}_{-0.3}$	$19.31^{+10.3}_{-6.0}$	$1.49^{+0.24}_{-0.27}$	$0.65^{+0.28}_{-0.28}$	$0.2^{+0.4}_{-0.1}$	0
189775	53.087378	−27.840274	25.4	3.63	$3.56^{+0.10}_{-0.27}$	⋯	$9.6^{+0.1}_{-0.2}$	$6.41^{+3.3}_{-1.8}$	$1.75^{+0.24}_{-0.28}$	$0.83^{+0.22}_{-0.26}$	$0.0^{+0.0}_{-0.0}$	0
190413	53.084040	−27.839348	24.4	17.77	$8.70^{+0.07}_{-0.06}$	⋯	$10.8^{+0.0}_{-0.0}$	$0.08^{+0.7}_{-0.1}$	$1.50^{+0.04}_{-0.04}$	$0.19^{+0.00}_{-0.00}$	$0.0^{+0.1}_{-0.0}$	1
198459	53.119122	−27.814039	24.3	3.58	$\cdots^{+0.00}_{-0.00}$	3.59^{j}	$10.6^{+0.1}_{-0.1}$	$34.02^{+15.7}_{-9.9}$	$2.62^{+0.38}_{-0.19}$	$0.57^{+0.16}_{-0.15}$	$0.0^{+0.0}_{-0.0}$	0
200576	53.154771	−27.806522	24.4	5.5	$\cdots^{+0.00}_{-0.00}$	⋯	$10.5^{+0.0}_{-0.0}$	$3.10^{+0.2}_{-0.3}$	$0.72^{+0.03}_{-0.03}$	$0.77^{+0.02}_{-0.01}$	$0.0^{+0.0}_{-0.0}$	0
201793	53.188275	−27.801938	25.3	4.02	$4.17^{+0.06}_{-0.04}$	⋯	$10.1^{+0.1}_{-0.1}$	$188.68^{+27.9}_{-32.1}$	$2.84^{+0.17}_{-0.21}$	$0.19^{+0.13}_{-0.09}$	$0.1^{+0.2}_{-0.1}$	0
203749	53.121420	−27.794912	26.0	7.66	$7.64^{+0.18}_{-0.12}$	⋯	$10.4^{+0.1}_{-0.2}$	$56.08^{+20.7}_{-20.6}$	$1.64^{+0.17}_{-0.17}$	$0.33^{+0.10}_{-0.12}$	$0.0^{+0.0}_{-0.0}$	1
204851	53.138593	−27.790253	24.5	5.46	$\cdots^{+0.00}_{-0.00}$	5.48^{k}	$9.8^{+0.0}_{-0.0}$	$207.39^{+6.9}_{-6.7}$	$1.83^{+0.05}_{-0.06}$	$0.02^{+0.05}_{-0.01}$	$0.0^{+0.0}_{-0.0}$	1
209303	53.206314	−27.775716	25.0	5.82	$5.77^{+0.08}_{-0.08}$	⋯	$9.9^{+0.1}_{-0.1}$	$47.25^{+5.3}_{-5.4}$	$1.13^{+0.12}_{-0.11}$	$0.24^{+0.13}_{-0.11}$	$0.0^{+0.1}_{-0.0}$	0
214839	53.196571	−27.757063	24.0	3.57	$4.13^{+0.06}_{-0.05}$	⋯	$10.3^{+0.1}_{-0.1}$	$53.32^{+8.7}_{-7.9}$	$1.61^{+0.12}_{-0.12}$	$0.25^{+0.14}_{-0.08}$	$0.2^{+0.3}_{-0.1}$	0
217926	53.184783	−27.744047	26.9	6.93	$\cdots^{+0.00}_{-0.00}$	5.04^{k}	$9.3^{+0.2}_{-0.5}$	$26.59^{+5.1}_{-4.1}$	$2.34^{+0.31}_{-0.74}$	$0.06^{+0.04}_{-0.04}$	$0.0^{+0.0}_{-0.0}$	0
219000	53.161375	−27.737665	25.1	6.92	$\cdots^{+0.00}_{-0.00}$	6.81^{k}	$10.0^{+0.2}_{-0.2}$	$142.53^{+20.1}_{-24.9}$	$1.73^{+0.17}_{-0.14}$	$0.19^{+0.15}_{-0.10}$	$0.0^{+0.0}_{-0.0}$	1
279678	53.108795	−27.869027	25.0	14.65	$4.72^{+0.05}_{-0.06}$	⋯	$10.0^{+0.0}_{-0.0}$	$393.50^{+16.1}_{-14.8}$	$3.09^{+0.10}_{-0.09}$	$0.01^{+0.00}_{-0.00}$	$0.0^{+0.0}_{-0.0}$	0

Notes. Properties of our *H*-band dropout sample, measured including MIRI + ALMA data.

[a] JADES DR1 ID.

[b] Photometric redshift measured by EAZY (z_{peak}).

[c] Photometric redshift measured by prospector if no spectroscopic redshift exists for this object; ID 200576 is fixed to the EAZY redshift as discussed in Section 4.1.

[d] $\log_{10}$ of the stellar mass in units of $M_\odot$.

[e] Star formation rate (SFR) measured by prospector using the most recent 30 Myr time bin of the star formation history (SFH) in units $M_\odot$ yr^{-1}.

[f] V-band attenuation.

[g] Mass-weighted age in units of Gyr.

[h] The ratio of bolometric luminosity from the galaxy divided by that from the AGN.

[i] Flag indicates the source meets our LRD color selection.

[j] Confirmed in JADES-NIRSpec data.

[k] Confirmed in FRESCO data.

context, we note what fraction of objects in JADES identified by their criteria also meet our criteria of F150W − F444W > 2.2 and F150W < 27 AB mag. We find that only 12% of massive double-break candidates as in Labbé et al. (2023b) overlap with our HST-dark sample, likely because of their requirement of a relatively blue SED between F150W − F277W < 0.7. We will discuss this overlap further in Section 6.2. Our sources are also redder than 50% of the sources selected based on F150W − F356W > 1.5 in Pérez-González et al. (2023), owing primarily to the bluer color chosen to include sources at z > 2. Thus in comparison to these other samples, our objects tend to be those with consistently red SEDs from the rest-frame UV to near-infrared, and, our sources are typically redder across the NIRCam wavelength baseline.

3.1. Comparison with Previously Identified Optically Faint Galaxies in GOODS-S

Our sample includes the majority of known optically faint or HST-dark galaxies that were identified in previous searches in this field (see the open circles in Figure 1; Wang et al. 2016; Franco et al. 2018; Alcalde Pampliega et al. 2019; Wang et al. 2019; Xiao et al. 2023b). Five out of seven of the *H*-band dropouts identified by Wang et al. (2016, 2019) that fully overlap with our imaging are identified by our parent sample *H*-band dropout color selection (all of which also overlap with the sample of Alcalde Pampliega et al. 2019). Five optically dark sources identified by pre-JWST data were not red enough to meet our selection (which were identified using different methods; Franco et al. 2018; Wang et al. 2019; Xiao et al.

Table 2
Properties of the *H*-band Dropouts without MIRI Data

ID[a]	R.A.	Decl.	F444W	Photo-z[b]	Photo-z[c]	Spec-z	$\log_{10}M^*$[d]	SFR[e]	A_V[f]	Age[g]	f_{AGN}[h]	LRD[i]
5070	53.092006	−27.903137	24.9	4.28	$4.59^{+0.05}_{-0.05}$	...	$10.0^{+0.0}_{-0.0}$	$1.43^{+0.2}_{-0.2}$	$0.02^{+0.03}_{-0.01}$	$0.96^{+0.07}_{-0.08}$	$0.0^{+0.0}_{-0.0}$	0
5756	53.062410	−27.901838	25.6	3.78	$3.53^{+0.18}_{-0.15}$	...	$9.6^{+0.3}_{-0.5}$	$14.45^{+11.5}_{-4.7}$	$1.94^{+0.54}_{-0.51}$	$0.57^{+0.37}_{-0.35}$	$0.0^{+0.9}_{-0.0}$	0
11004	53.059444	−27.893633	28.9	11.48	$5.07^{+3.67}_{-2.35}$	...	$8.7^{+0.9}_{-0.8}$	$2.26^{+12.4}_{-1.4}$	$3.18^{+0.09}_{-1.35}$	$0.12^{+0.09}_{-0.06}$	$0.0^{+0.6}_{-0.0}$	0
11786	53.119075	−27.892556	26.3	7.34	$7.28^{+0.08}_{-0.07}$	...	$10.8^{+0.3}_{-0.3}$	$1242.03^{+876.4}_{-459.4}$	$4.30^{+0.57}_{-0.62}$	$0.10^{+0.11}_{-0.06}$	$0.0^{+0.2}_{-0.0}$	1
13436	53.068073	−27.890551	28.1	4.69	$5.60^{+0.06}_{-0.04}$	...	$8.2^{+0.2}_{-0.2}$	$0.67^{+0.1}_{-0.1}$	$0.02^{+0.05}_{-0.02}$	$0.33^{+0.17}_{-0.16}$	$0.0^{+0.4}_{-0.0}$	0
35203	53.140041	−27.874603	27.2	3.89	$4.20^{+0.20}_{-0.27}$	...	$9.0^{+0.1}_{-0.1}$	$0.11^{+0.4}_{-0.1}$	$0.51^{+0.43}_{-0.30}$	$0.79^{+0.20}_{-0.26}$	$0.0^{+0.5}_{-0.0}$	0
35453	53.057030	−27.874375	25.1	5.04	$5.09^{+0.11}_{-0.13}$	...	$10.2^{+0.1}_{-0.1}$	$1.83^{+1.7}_{-1.0}$	$1.01^{+0.27}_{-0.26}$	$0.65^{+0.11}_{-0.13}$	$0.0^{+0.3}_{-0.0}$	0
39005	53.080165	−27.871306	28.5	15.83	$0.88^{+0.22}_{-0.16}$	...	$7.2^{+0.2}_{-0.2}$	$0.01^{+0.0}_{-0.0}$	$6.82^{+2.03}_{-1.81}$	$0.17^{+0.04}_{-0.05}$	$0.0^{+0.0}_{-0.0}$	0
39376	53.064113	−27.870933	25.8	6.32	$7.36^{+0.11}_{-0.11}$	...	$11.0^{+0.2}_{-0.2}$	$1665.58^{+1148.3}_{-565.0}$	$4.24^{+0.66}_{-0.55}$	$0.12^{+0.16}_{-0.07}$	$0.0^{+0.1}_{-0.0}$	1
40983	53.046050	−27.869633	28.8	13.49	$3.52^{+0.17}_{-0.17}$	...	$8.0^{+0.1}_{-0.1}$	$0.01^{+0.0}_{-0.0}$	$0.27^{+0.31}_{-0.17}$	$0.24^{+0.03}_{-0.03}$	$0.0^{+0.2}_{-0.0}$	0
45564	53.055347	−27.866132	25.1	3.78	$3.56^{+0.11}_{-0.13}$	...	$9.7^{+0.2}_{-0.2}$	$11.96^{+6.9}_{-3.7}$	$1.56^{+0.41}_{-0.59}$	$0.56^{+0.24}_{-0.26}$	$0.0^{+0.3}_{-0.0}$	0
65559	53.041051	−27.854478	25.2	4.07	$4.46^{+0.05}_{-0.05}$	...	$9.8^{+0.0}_{-0.0}$	$1.28^{+0.1}_{-0.1}$	$0.00^{+0.00}_{-0.00}$	$1.27^{+0.03}_{-0.07}$	$0.0^{+0.0}_{-0.0}$	0
75446	53.036392	−27.846575	25.3	5.83	$6.36^{+0.30}_{-0.16}$	...	$10.2^{+0.2}_{-0.2}$	$1.89^{+27.8}_{-0.8}$	$0.16^{+1.13}_{-0.14}$	$0.62^{+0.07}_{-0.13}$	$0.0^{+0.2}_{-0.0}$	0
79086	53.044180	−27.842933	27.2	4.87	$4.68^{+0.26}_{-0.27}$	...	$8.9^{+0.1}_{-0.3}$	$0.15^{+1.1}_{-0.1}$	$0.21^{+0.34}_{-0.15}$	$0.55^{+0.19}_{-0.27}$	$0.0^{+0.2}_{-0.0}$	0
82667	53.067296	−27.838335	26.2	6.46	$6.29^{+0.16}_{-0.24}$	...	$10.5^{+0.4}_{-0.4}$	$333.17^{+415.8}_{-138.5}$	$3.82^{+0.95}_{-0.86}$	$0.21^{+0.14}_{-0.12}$	$0.0^{+0.1}_{-0.0}$	1
104849	53.101881	−27.810949	26.3	5.29	$5.12^{+0.00}_{-0.00}$	5.12[j]	$9.1^{+0.3}_{-0.2}$	$23.95^{+5.4}_{-4.4}$	$1.90^{+0.36}_{-0.34}$	$0.15^{+0.13}_{-0.09}$	$0.0^{+0.0}_{-0.0}$	0
152330	53.102742	−27.744467	25.8	5.16	$5.07^{+0.01}_{-0.01}$	...	$9.9^{+0.2}_{-0.2}$	$189.12^{+33.8}_{-29.0}$	$3.09^{+0.22}_{-0.29}$	$0.16^{+0.15}_{-0.12}$	$0.0^{+0.2}_{-0.0}$	0
161143	53.024862	−27.894925	27.3	3.34	$3.39^{+0.06}_{-0.08}$	...	$8.7^{+0.1}_{-0.1}$	$0.53^{+0.2}_{-0.2}$	$0.77^{+0.21}_{-0.29}$	$0.75^{+0.23}_{-0.27}$	$0.0^{+0.2}_{-0.0}$	0
161967	53.036504	−27.894148	25.6	3.17	$3.00^{+0.04}_{-0.04}$	...	$9.7^{+0.1}_{-0.1}$	$67.87^{+13.8}_{-12.6}$	$3.47^{+0.35}_{-0.31}$	$0.28^{+0.19}_{-0.16}$	$0.0^{+0.0}_{-0.0}$	0
168364	53.144844	−27.879612	27.5	6.08	$5.93^{+0.20}_{-0.21}$	...	$9.5^{+0.4}_{-0.4}$	$27.47^{+62.6}_{-12.4}$	$2.67^{+0.95}_{-0.82}$	$0.20^{+0.16}_{-0.12}$	$0.0^{+0.4}_{-0.0}$	0
170384	53.074866	−27.875907	24.2	4.73	$5.62^{+0.09}_{-0.05}$	...	$11.0^{+0.1}_{-0.2}$	$581.71^{+159.6}_{-135.7}$	$2.61^{+0.32}_{-0.26}$	$0.20^{+0.12}_{-0.10}$	$0.0^{+0.4}_{-0.0}$	0
171209	53.043730	−27.874185	24.8	3.65	$3.75^{+0.20}_{-0.08}$	...	$9.9^{+0.2}_{-0.1}$	$6.32^{+9.5}_{-3.6}$	$1.32^{+0.48}_{-0.34}$	$0.59^{+0.21}_{-0.21}$	$0.1^{+1.2}_{-0.0}$	0
171973	53.086837	−27.873047	23.0	4.49	$3.42^{+0.24}_{-0.15}$	...	$11.5^{+0.1}_{-0.1}$	$3843.17^{+1012.1}_{-687.9}$	$5.36^{+0.19}_{-0.23}$	$0.25^{+0.18}_{-0.13}$	$0.0^{+0.1}_{-0.0}$	0
172813	53.047201	−27.870031	23.4	11.67	$4.20^{+0.12}_{-0.15}$	...	$11.1^{+0.2}_{-0.2}$	$704.25^{+213.4}_{-155.5}$	$3.88^{+0.42}_{-0.28}$	$0.13^{+0.05}_{-0.05}$	$0.0^{+0.0}_{-0.0}$	0
173706	53.080377	−27.869467	24.1	3.64	$3.55^{+0.07}_{-0.04}$	...	$10.4^{+0.2}_{-0.3}$	$231.42^{+59.3}_{-47.4}$	$3.10^{+0.24}_{-0.26}$	$0.44^{+0.22}_{-0.23}$	$0.0^{+1.1}_{-0.0}$	0
177680	53.064791	−27.862624	23.3	8.63	$1.33^{+2.18}_{-0.02}$	...	$10.0^{+0.9}_{-0.3}$	$95.58^{+1517.9}_{-21.0}$	$5.27^{+0.55}_{-1.05}$	$0.11^{+0.13}_{-0.05}$	$0.0^{+0.0}_{-0.0}$	0
189276	53.042071	−27.842660	24.8	5.87	$5.89^{+0.29}_{-1.18}$	...	$10.3^{+0.5}_{-0.3}$	$58.38^{+73.8}_{-23.0}$	$1.12^{+1.90}_{-0.43}$	$0.22^{+0.26}_{-0.11}$	$0.0^{+0.8}_{-0.0}$	0
189494	53.162966	−27.841946	24.5	4.34	$4.50^{+0.06}_{-0.05}$	...	$10.4^{+0.1}_{-0.1}$	$19.31^{+10.3}_{-6.0}$	$1.49^{+0.24}_{-0.27}$	$0.65^{+0.28}_{-0.28}$	$0.2^{+0.4}_{-0.1}$	0
189508	53.042426	−27.841815	23.8	4.76	$4.80^{+0.04}_{-0.04}$	...	$11.7^{+0.1}_{-0.1}$	$1417.83^{+646.2}_{-688.5}$	$4.46^{+0.47}_{-0.84}$	$0.66^{+0.17}_{-0.15}$	$0.0^{+0.1}_{-0.0}$	0
212950	53.132665	−27.765488	24.0	4.18	$4.32^{+0.05}_{-0.05}$	...	$10.4^{+0.0}_{-0.1}$	$0.56^{+0.1}_{-0.1}$	$0.04^{+0.06}_{-0.03}$	$1.01^{+0.05}_{-0.05}$	$0.0^{+0.1}_{-0.0}$	0
236329	53.089004	−27.738202	24.8	6.30	$5.69^{+0.10}_{-0.13}$	...	$11.1^{+0.1}_{-0.1}$	$41.50^{+23.1}_{-15.5}$	$2.56^{+0.25}_{-0.24}$	$0.53^{+0.07}_{-0.08}$	$0.0^{+0.0}_{-0.0}$	0
237934	53.055599	−27.725428	27.9	15.67	$5.87^{+0.24}_{-0.24}$	...	$8.4^{+0.3}_{-0.5}$	$2.91^{+2.2}_{-1.1}$	$1.13^{+1.43}_{-0.42}$	$0.07^{+0.03}_{-0.03}$	$0.0^{+0.2}_{-0.0}$	0
242033	53.041931	−27.696133	28.1	4.05	$4.19^{+0.38}_{-0.55}$	...	$8.4^{+0.2}_{-0.2}$	$0.32^{+0.2}_{-0.2}$	$0.23^{+0.33}_{-0.17}$	$0.60^{+0.24}_{-0.17}$	$0.0^{+0.1}_{-0.0}$	0
242342	53.054126	−27.694044	25.5	3.37	$2.65^{+0.03}_{-0.03}$	...	$9.4^{+0.1}_{-0.1}$	$88.36^{+19.1}_{-11.6}$	$3.14^{+0.27}_{-0.21}$	$0.03^{+0.10}_{-0.02}$	$0.0^{+0.0}_{-0.0}$	0
247084	53.060897	−27.718430	24.1	11.69	$2.74^{+0.12}_{-2.31}$	...	$9.6^{+0.2}_{-1.4}$	$28.05^{+12.7}_{-18.9}$	$2.56^{+4.13}_{-0.30}$	$0.12^{+0.08}_{-0.04}$	$0.8^{+2.3}_{-0.0}$	0
283711	53.082649	−27.864812	28.8	14.56	$3.66^{+0.88}_{-0.31}$	...	$7.9^{+0.2}_{-0.3}$	$0.74^{+0.5}_{-0.3}$	$1.21^{+0.53}_{-0.62}$	$0.09^{+0.06}_{-0.04}$	$0.0^{+0.2}_{-0.0}$	0
284487	53.078688	−27.839396	26.8	3.64	$3.71^{+0.17}_{-0.13}$	...	$9.1^{+0.1}_{-0.1}$	$0.07^{+0.4}_{-0.0}$	$0.27^{+0.42}_{-0.19}$	$0.86^{+0.21}_{-0.28}$	$0.0^{+0.4}_{-0.0}$	0
284527	53.041065	−27.837737	23.3	9.84	$0.45^{+0.29}_{-0.08}$	...	$8.0^{+0.4}_{-0.2}$	$0.13^{+0.1}_{-0.1}$	$7.50^{+0.70}_{-1.34}$	$0.23^{+0.07}_{-0.05}$	$0.4^{+2.1}_{-0.2}$	0
284756	53.073995	−27.828662	24.4	3.32	$3.57^{+0.08}_{-0.11}$	...	$10.1^{+0.2}_{-0.2}$	$58.65^{+21.9}_{-18.9}$	$2.14^{+0.31}_{-0.39}$	$0.46^{+0.32}_{-0.25}$	$0.0^{+0.4}_{-0.0}$	0
286677	53.155126	−27.727785	24.9	3.51	$3.57^{+0.07}_{-0.35}$	...	$9.7^{+0.2}_{-0.3}$	$82.16^{+19.8}_{-22.7}$	$2.39^{+0.25}_{-0.28}$	$0.17^{+0.19}_{-0.11}$	$0.0^{+0.8}_{-0.0}$	0

Notes. Properties of our *H*-band dropout sample, measured including only HST + NIRCam data.
[a] JADES DR1 ID.
[b] Photometric redshift measured by EAZY (z_{peak}).
[c] Photometric redshift measured by prospector if the object does not have a spectroscopic redshift.
[d] $\log_{10}$ of the stellar mass in units of $M_\odot$.
[e] SFR measured by prospector using the most recent 30 Myr time bin of the SFH in units of $M_\odot\ yr^{-1}$.
[f] V-band attenuation.
[g] Mass-weighted age in units of Gyr.
[h] The ratio of the bolometric luminosity from the galaxy divided by that from the AGN.
[i] Flag indicates the source meets our LRD color selection.
[j] Confirmed in FRESCO data.

2023b) and a further four are brighter than our F150W magnitude limit.

We note that our sample includes the optically dark object AGS11 identified in Franco et al. (2018; our ID 279678), which had been identified based on a blind ALMA detection with no optical counterpart. JWST now demonstrates that

AGS11 has one of the most extreme red colors among our sample (F150W – F444W > 4), remains still undetected in all short-wavelength filters (despite our ultradeep imaging), and is also one of the largest, reaching nearly 1″ in extent. This source was previously hypothesized to reside in a confirmed overdensity, using ALMA spectroscopy, at $z \sim 3.4$ (Zhou et al.

2020), although the source itself was not detected in ALMA spectroscopy. Based on our photometry, we find a higher redshift of $z \sim 4.72^{+0.05}_{-0.06}$ for this source (which likely explains their finding of no spectroscopic confirmation). Based on this comparison, our selection identifies a relatively unexplored sample in this field, below the detection limits of other multiwavelength selections (including ALMA).

4. Measuring Physical Properties

4.1. Redshift Estimations

Our sample exhibits very red and sometimes featureless SEDs. To assist in our more detailed SED modeling to infer the physical properties, we first measure preliminary photometric redshifts based on the HST and JWST NIRCam photometry using EAZY (Brammer et al. 2008) as presented in Hainline et al. (2023b). We measure the redshift as the probability-weighted average peak of the photometric redshift distribution without any priors. This preliminary photometric redshift measurement with EAZY is used to set a prior on the redshift for our more detailed photometric modeling that we discuss in Section 4.2.

A small fraction of our sample also have spectroscopy. These include nine sources with one emission line with S/N > 3 in FRESCO data (Oesch et al. 2023), using spectral extractions presented in F. Sun et al. (2024, in preparation) combining JADES and FRESCO data. Two sources that received slits from the JADES-NIRSpec program also have one emission line with S/N > 3 (Eisenstein et al. 2023a; Bunker et al. 2023). Below we describe our procedure for visually inspecting the spectroscopic redshifts in conjunction with the photometric probability density function (PDF(z)) measured using EAZY, and our process for deciding how to set the redshift priors that we use in our SED modeling in the case of uncertain spectroscopic redshift solutions. We show the spectroscopic data and our redshift determination in Figure 12.

For the case of the FRESCO sources, all nine sources have only one line, resulting in ambiguity in the redshift solution. For four out of the nine, the one line is weakly detected with 3 < S/N < 5. The five brighter, significantly detected FRESCO sources also only show a single emission line. Thus for all, the solution is heavily dependent on the most probable photometric redshift measured with EAZY. We find that this often leads to a degeneracy between Hα at $z \sim 5$–6 and [O III] λ5007 at $z \sim 7$–8 (assumed to be the detected line, given it is 3× brighter than the other [O III] doublet). This is because our sources are all very red, and the Lyman break is often faint and poorly constrained; thus, photometric boosting by strong rest-frame optical line emission tends to have a strong influence on the photometric redshift solution. Thus, EAZY sometimes yields a comparable probability for both Hα or Hβ + [O III] solutions. In these cases, we visually inspect the EAZY χ^2 surface in conjunction with the SED shape and the detected line's wavelength, and we also consider whether the physical parameters derived from the SED modeling are reasonable (see the next section).

After this iterative process, we find that for four sources with confidently detected lines (IDs 219000, 154428, 184838, and 204851) the photometric evidence clearly agrees with the FRESCO redshift solutions. For a fifth confidently detected single line source, ID 217926, we find that in fact the photometry (primarily near the Lyman break) supports an altered redshift solution at $z = 5.04$ rather than $z = 7.6$,

assuming the securely detected line is Hα, and not [O III] λ5007. For three of the less securely identified objects (IDs 90354, 120484, and 104849), the marginal emission lines are more difficult to interpret so close to the limiting S/N, although the candidate lines do have solutions that are consistent with the EAZY photometric redshifts. We decide to explore the SED-modeling solutions that are retrieved for both the case where the redshift is a free parameter, and also while fixing to the tentative redshift. We get consistent results within the uncertainties either using the tentative spectroscopic redshifts or leaving the redshift free. We therefore consider these spectroscopic redshifts as robust, but in any case this choice does not impact our results.

For the last marginal case (ID 126594) we find a low-confidence marginal emission line, which, assuming it is the stronger of the [O III] doublet, puts this source at $z = 7.9$. For this source, the redshift probability lines up with one of three plausible (narrow) photometric redshift solutions based on the presence of emission line boosting to the photometry, although this redshift solution is not the one most favored by the photometry (which prefers a higher photometric redshift of $z = 9.9$). However, at the redshift preferred by EAZY (which is also the redshift preferred by our SED modeling when the redshift is left as a free parameter), the galaxy is quite bright and in excess of expected stellar masses given our small survey area (based on our SED-modeling procedure outlined in the next section). Thus, we take the approach of comparing stellar masses measured for both cases. We find that at the $z = 7.9$ redshift solution, which is in agreement with the tentative line detection in the FRESCO data, the SED modeling yields a more realistic stellar mass given our small area (see Section 6.2). Thus, we opt for this more conservative redshift constraint and fix to the marginal spectroscopic redshift.

In addition, two of our sources were observed as part of the JADES-NIRSpec campaign (Eisenstein et al. 2023a; Bunker et al. 2023). ID 198459 was spectroscopically confirmed at $z = 3.588$, which is consistent with the photometric redshift we measured using EAZY ($z = 3.65$). For the second source, ID 132229, however, the solution is less obvious. While the redshift is tentative (based on detection of the [O III] λ5007 line at $z = 7.247$), and consistent with the EAZY redshift ($z \sim 7.5$), we found that leaving the redshift as a free parameter yielded an inconsistently high photometric redshift of $z \sim 8.1$. If modeled at such a high redshift, we find that the inferred stellar mass is $\log_{10}(M^*/M_\odot) \sim 10.7$, unphysically high for a $z \sim 8$ source in a small area (which we will discuss further in Section 6.2), lending some credibility to the lower-redshift solution. Therefore, for this source we chose to accept the tentative spectroscopic redshift at $z = 7.247$ in the modeling and results.

We finally discuss the photometric redshift of a source without spectroscopy, ID 200576. This galaxy has a significant detection at 0.7 μm, indicating a photometric redshift with a hard upper limit at $z < 6.05$ (the transmission of HST/ACS F775W filter drops below 10% of the maximum at 8570 Å, corresponding to a Lyman α redshift of 6.05). In agreement with this, EAZY modeling of just HST + NIRCam returns $z = 5.5$. However, when leaving the redshift as a free parameter in our prospector modeling with MIRI and ALMA data included, we find that the code gives preference to higher-redshift solutions, perhaps driven by a flux excess at much higher S/N in F356W and the decrease in relative weighting of

the low-S/N HST data once more filters are included. However, the excess of F356W combined with the lack of obvious excesses seen in F335M or F410M from [O III] + Hβ limit the redshift to be at either $z \gtrsim 6.5$ or $z \sim 5.4$–5.5 (see, e.g., Endsley et al. 2023). Noting that none of the SED solutions to this source are an excellent fit to the available data, we opt to put a stronger prior on the EAZY solution at $z = 5.5$, and fix the redshift in the prospector modeling. We further make this choice because it is also the most conservative assumption in terms of the recovered physical properties; even at the lower-redshift $z = 5.5$ solution, the source is very massive for our limited survey area. Adopting higher-redshift solutions would only increase the mass and create additional tension (explored in Section 6.2).

4.2. Spectral Energy Distribution Modeling

To measure the more detailed physical properties, we use the prospector Bayesian code to model the SEDs (Johnson et al. 2021) using the Flexible Stellar Population Synthesis models (Conroy et al. 2009), MIST stellar isochrone libraries (Choi et al. 2016; Dotter 2016), and the stellar spectral libraries MILES (Falcón-Barroso et al. 2011). We use the Markov Chain Monte Carlo sampling code DYNESTY (Speagle 2020), adopting the nested sampling procedure (Skilling 2004). Our fiducial prospector setup broadly follows that outlined in Ji et al. (2023) with a few alterations. We adopt the Madau (1995) intergalactic medium absorption model. We briefly summarize the other model assumptions and priors used here.

We use a nonparametric star formation history (SFH) composed of nine time bins with a constant star formation rate in each bin. We fix the first two bins to be at 0–30 and 30–100 Myr. Throughout this work, we will refer to the star formation rate (SFR) as modeled by our SED fitting as that inferred in the most recent 30 Myr (the latest time bin). The last time bin is assumed to be $0.85t_H - t_H$ where t_H is the Hubble time at the time of observation; the remaining six bins are evenly spaced in logarithmic space between 100 Myr and $0.85t_H$. It has been shown that the recovered physical properties are largely insensitive to the number of bins used, when it is greater than five (Leja et al. 2019). We further adopt the continuity prior (to weight for physically plausible SFH forms, thus mitigating overfitting the data), which has been demonstrated to work well across various galaxy types (Leja et al. 2019).

We adopt the Byler et al. (2017) nebular continuum and line emission model. We set both the stellar metallicity and gas phase metallicities as free parameters and assume flat priors in logarithmic space (with $\log(Z_*/Z_\odot) \in (-2, 0.19)$ and $\log(Z_{gas}/Z_\odot) \in (-2, 0.5)$). The ionization parameter U is also left as free parameter using a flat prior with $\log U \in (-4, 1)$.

We adopt the Draine & Li (2007) dust emission model with priors as defined in Williams et al. (2019) to allow for more flexible, hotter dust temperatures, which may be prevalent at higher redshift (da Cunha et al. 2013). These include flat priors on the starlight intensity on dust grains $U_{min} \in (1, 25)$, and the faction of stars at U_{min}, $\gamma \in (0.01, 0.99)$. These parameters are related to $T_{dust} \sim 18 \times <U>^{1/6}$ K as in Draine et al. (2014). We also adopt flat priors on the polycyclic aromatic hydrocarbon (PAH) mass fraction, $qpah \in (0.5, 4)$.

We assume a two-component dust attenuation model where the dust attenuation of nebular emission and young stellar populations, and of old stellar populations, are treated

differently (Charlot & Fall 2000). For stellar populations older than 10 Myr, we assume the dust attenuation using the parameterization from Noll et al. (2009; i.e., a modified Calzetti et al. 2000 dust attenuation law). Stellar populations younger than 10 Myr are assumed to have the same dust attenuation law as for the nebular emission (for further details on the various dust parameter priors, dependencies, and prior ranges, see Tacchella et al. 2022a; Ji et al. 2023). The dust model priors are set such that the V-band attenuation (A_V) can vary between $A_V \in (0, 10)$ with a flat prior.

We also include AGN dust torus templates from Nenkova et al. (2008a) and Nenkova et al. (2008b), with flat priors in logarithmic space for both the ratio of bolometric luminosity from the galaxy divided by that from the AGN ($f_{AGN} \in (10^{-5}, 3)$), and the optical depth of clumps in the AGN dust torus at 5500 Å ($\tau_{AGN} \in (5, 150)$).

We use the photometric redshift measured using EAZY in the last section as a photometric redshift prior for prospector modeling (the mean of a Gaussian prior width ± 0.5). For the cases where the EAZY fit resulted in a redshift $z > 8$, we instead use a flat prior on the redshift to allow the possibility of lower-redshift solutions. For the sources with spectroscopic redshift constraints, we fix to the spectroscopic redshift that was identified in the last section. We further limit the S/N of any photometric point, which is capped at 20 (minimum 5% uncertainty, reflecting uncertainties in the relative photometric calibration between filters).

5. Results

5.1. Impact of MIRI + ALMA Data

To date, photometric studies of similarly red galaxies at $z > 3$ have been restricted to NIRCam and HST data, with some limited wavelength coverage from 1–2 MIRI bands (Akins et al. 2023; Barro et al. 2023; Barrufet et al. 2023b; Endsley et al. 2023; Labbé et al. 2023b, 2023a; McKinney et al. 2023; Pérez-González et al. 2023; Rodighiero et al. 2023). To explore the impact on recovered properties when using this more limited wavelength coverage, we run our prospector modeling for the 29 sources inside the MIRI footprint using only the HST + NIRCam data, and again including also the MIRI + ALMA data.

In Figure 2 we present a comparison of the inferred best-fit parameters: photometric redshift, stellar mass, and SFR using HST + NIRCam data only, with the result obtained when including the MIRI + ALMA data. We find that including photometry from both the seven MIRI filters and ALMA 1 mm data overall results in consistent redshifts as with just the HST + NIRCam data (with a few outliers; left panel of Figure 2). However, including MIRI + ALMA data significantly alters other key parameters recovered using SED modeling. We find that the addition of MIRI + ALMA data serves to lower both the stellar masses and SFRs of galaxies compared with using HST + NIRCam data alone. In particular, we find a systematic reduction in stellar mass (median decrease of 0.6 dex, and as large as 1 dex) for galaxies with HST + NIRCam–measured $\log_{10}(M^*/M_\odot) > 10$. We similarly find that for SFRs in excess $\sim 100\ M_\odot\ yr^{-1}$ as measured by HST + NIRCam data alone we calculate a median factor of 10 decrease in the SFR inferred when including MIRI + ALMA data. These findings indicate that studies based on the more limited data sets are likely to overestimate both the star
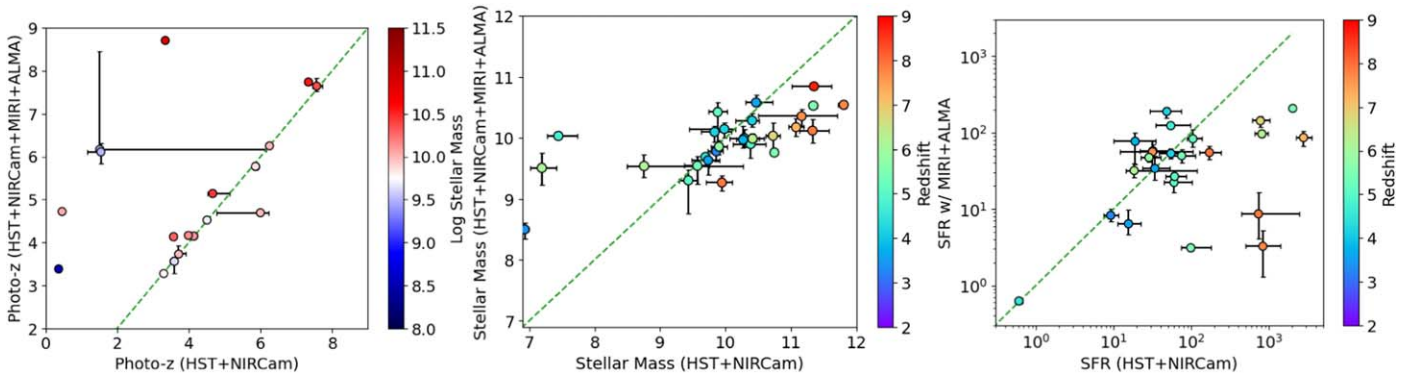
Figure 2. For sources with MIRI and ALMA coverage, we compare the inferred photometric redshift, stellar mass, and SFR from our `prospector` modeling of HST + NIRCam + MIRI + ALMA data vs. just the HST + NIRCam photometry. The left panel shows the inferred photometric redshift (sources with spectroscopic redshifts are excluded from this panel). The middle panel shows the stellar mass, and the right panel shows the SFR. At the very high-mass and SFR end, we find that including the MIRI + ALMA data lowers the extreme masses and SFRs that are otherwise inferred (median decrease of 0.6 dex for sources above $\log_{10}(M^*/M_\odot) > 10$, and median 10× less for SFR $> 100\ M_\odot\ \mathrm{yr}^{-1}$). This figure shows that stellar masses and SFRs can be wrong for extreme and red sources when using NIRCam data without longer-wavelength constraints.

formation rate density (SFRD) and the stellar mass density, at high redshift significantly, in particular for galaxies where the HST + NIRCam data infer high masses and SFRs. This seems to be the case even despite the excellent medium-band coverage of JADES and JEMS.

We note that this finding may not be representative of the general galaxy population, since our sample has much more extreme red colors than typical galaxies at these redshifts. A systematic assessment of the impact of multiple MIRI bands on mass and SFR across redshifts has not yet been undertaken (although see simulations based on mock galaxies in Bisigello et al. 2019; Kemp et al. 2019; Kauffmann et al. 2020; and an analysis of MIRI-selected $z \lesssim 3$ sources in Li et al. 2024). However, analyzes with more limited filters (F560W and/or F770W) suggest mixed results. A similar impact to ours was noted in Papovich et al. (2023) using a more representative sample of galaxies at similar redshifts (although comparing to modeling with a much more limited set of only HST plus IRAC data). Those authors find that, on average, the stellar mass decreases by $\langle \Delta \log M_* \rangle = 0.25$ dex at $4 < z < 6$ and 0.37 dex at $6 < z < 9$. Those authors also find a systematic reduction in the SFR of $\langle \Delta \log \mathrm{SFR} \rangle = 0.14$ dex at $4 < z < 6$ and 0.27 dex at $6 < z < 9$. MIRI likely has a large impact in this case owing to a lack of NIRCam photometry, which can break degeneracies between continuum and emission lines, and which translates to a less robust constraint on rest-frame optical continuum at high redshifts. While their result is qualitatively in line with what we find for the most extreme of our red sources, accumulating evidence indicates that including some MIRI data (in particular, F770W, covering rest frame $\sim$1–2 μm) may not be essential to achieving more accurate estimates for typical galaxies. J. M. Helton et al. (2024, in preparation) find that for $7 < z < 9$ galaxies (using our same NIRCam filter set), that the stellar population models with and without MIRI data are similar. Additionally, Alberts et al. (2023) find that stellar masses of $\log_{10}(M^*/M_\odot) > 9$ galaxies at $3 < z < 6$ also demonstrate no systematic difference when F770W is included. This is likely due to the fact that our sources are very red in the rest-frame optical, and without the long baseline of MIRI coverage the modeling tends to overestimate the dust attenuation (thus the modeling returns a higher stellar mass with higher attenuation for a fixed rest-frame optical flux).

Regardless, since in this study we have both multiple NIRCam medium bands plus multiple MIRI filters (mitigating uncertainties in constraining the stellar mass from both angles), our measurements are likely to be relatively reliable despite the exceptional character of our very red sources. However, this exercise demonstrates that the MIRI and ALMA data are of particular importance for sources with extreme red colors. Thus, caution should be exercised when interpreting the SED modeling of sources with red (and often featureless) SEDs without mid- and far-infrared wavelength coverage. Further, the uncertainties that arise from lacking the fuller wavelength coverage are not reflected in the error bars of mass and SFR measured with HST + NIRCam data alone.

5.2. Properties of Optically Faint (HST-dark) Galaxies

In this section, we characterize the properties of our sample of very red sources, in particular highlighting the diversity of our sample. Our `prospector` modeling indicates that our sources range from $3 < z < 8$, revising all of the higher-redshift solutions that were measured using EAZY (owing to nondetections in the observed optical and near-infrared; Figure 1). We also find that our sample includes galaxies at a range of stellar masses from $\log_{10}(M^*/M_\odot) \sim 8.2$–10.8, with moderate median SFRs ($\sim$50 $M_\odot$ yr^{-1}), high attenuation ($A_V \sim 2$), and moderately evolved stellar populations (mass-weighted age $\sim$ 250 Myr). These are similar to initial JWST explorations (Barrufet et al. 2023b; Pérez-González et al. 2023; Rodighiero et al. 2023).

As shown in Figure 11, our sample of *H*-band dropouts have incredibly diverse morphologies, ranging from large extended disks (e.g., J. L. Gibson et al. 2024, submitted; Nelson et al. 2023), to potentially merging clumps or groups, while a large fraction are remarkably compact, close to the resolution limit of F444W. This diversity is in line with expectations from simulations that (1) whether dusty galaxies are "dark" is a strong function of viewing angle for a range of galaxy types and (2) the most massive galaxies will pass through this phase early in the Universe's history due to prodigious dust production (Cochrane et al. 2023). In the subsections below, we review the subcategories of objects that we identify in our sample.
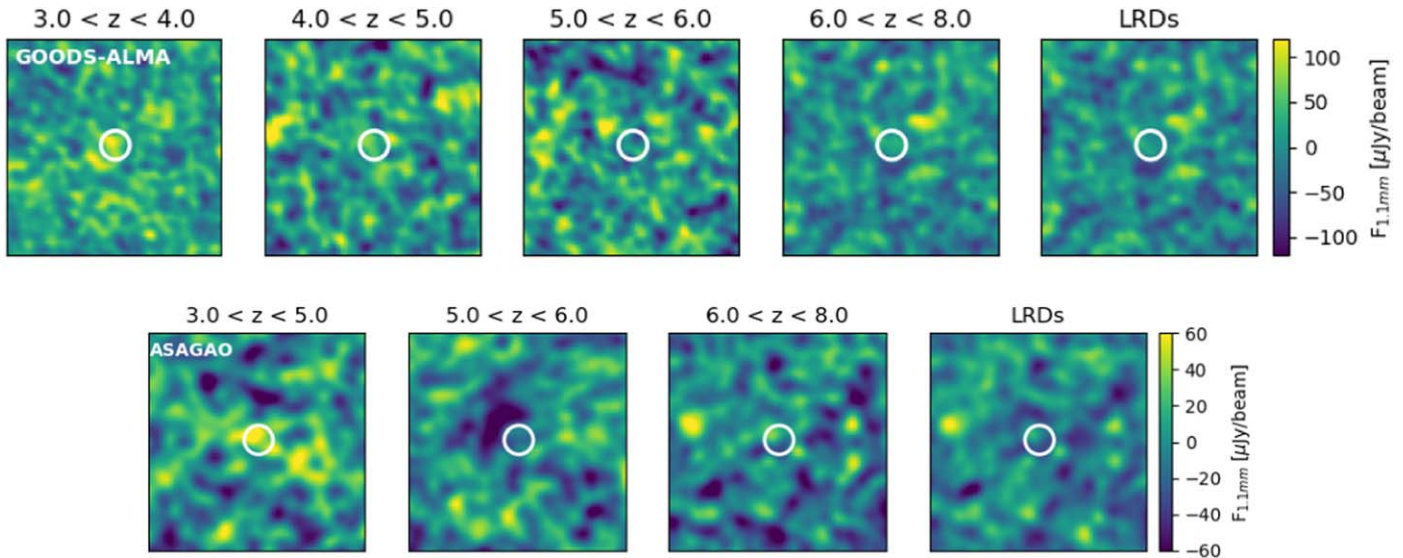
Figure 3. Top panel: ALMA 1.1 mm stacks of our entire sample of galaxies (including NIRCam-only sources, with individual detections removed) using the GOODS-ALMA data from Franco et al. (2018), which cover our entire sample. Bottom panel: ALMA 1.1 mm stacks of a subset of our galaxies that are inside the footprint of the deeper ASAGAO imaging (individual detections removed). Only one source is inside the footprint at $3 < z < 4$, so we instead show a combined $3 < z < 5$ redshift bin. Our sample below $z < 5$ exhibits possible cold dust emission (2.2–3σ for both maps, respectively), consistent with low-luminosity DSFGs. Sources at $z > 5$ (including all LRDs) do not show detectable dust emission. The far right panels show the ALMA stack of all nine LRDs, which reaches a nondetection upper limit of 32 μJy beam^{-1}.

5.2.1. Dusty Star-forming Galaxies in Our Sample

A minority of our sources exhibit detectable ALMA emission, indicative of dust-obscured star formation at the level typical of dusty, star-forming galaxies (DSFGs; SFR $> 100\ M_\odot$ yr^{-1}; Casey et al. 2014). Four sources between $3.6 < z < 5$ show significant ALMA detections ($>4\sigma$) in the range 0.5–1.0 mJy beam^{-1}, well below those of prototypical submillimeter galaxies (their ALMA properties have been studied elsewhere; Franco et al. 2018; Hatsukade et al. 2018; Xiao et al. 2023b). The NIRCam and MIRI cutouts (Figure 11) show that 3/4 ALMA sources are the most extended disk-like objects in our sample, while the fourth (ID 201793) is compact but clearly resolved in the short-wavelength filters. These sources are qualitatively similar to ALMA-only objects that have been identified by 2–3 mm ALMA imaging at $z > 4$, total infrared luminosity $\log_{10}(L_{\rm IR}/L_\odot) \sim 12$–12.5, $\log_{10}(M^*/M_\odot) \sim 10.5$–11, SFR ~ 200–300, and ~ 25 AB mag at 4 μm (e.g., Williams et al. 2019; Manning et al. 2022, among others). Noting that our MIRI area is quite small, we find a similar abundance of ~ 0.1 square arcmin^{-1}.

However, the overwhelming majority of our sources are not detected in any of the 1 mm ALMA data (25 out of 29) and thus have only upper limits to their total infrared luminosity. These upper limits are $\log_{10}(L_{\rm IR}/L_\odot) \lesssim 12$, based on integrating the 8–1100 μm (rest frame) best-fit SED from pro-spector (see Section 6.1.). While this means we cannot robustly constrain how much lower is the exact level of obscured star formation individually, we stack the 1.1 mm ALMA images for all sources that are not individually detected (calculating the inverse-variance-weighted average) from the GOODS-ALMA program ($\sigma_{\rm rms} \sim 180\ \mu$Jy beam^{-1}; Franco et al. 2018) for which we have coverage of our entire MIRI footprint. We do not find a significant detection in the stacked data at $3 < z < 4$ or $4 < z < 5$, and only a 2σ detection from the combined redshift range. However, a majority of the sources sit inside the deeper ASAGAO footprint. We perform the stack again for sources inside ASAGAO, finding again a marginal

detection for $3 < z < 5$ sources in our sample with $55 \pm 24\ \mu$Jy beam^{-1}. The ASAGAO results from inside the MIRI footprint are shown in Figure 3.

It is possible that our limited sample size is too small for a significant detection. Therefore, we repeat the stacking while including our broader NIRCam-only sample within the GOODS-ALMA footprint, which roughly doubles the sample size. We also show the GOODS-ALMA stack from the broader NIRCam-only sample in Figure 3. We find that this test does yield a more significant (3σ) stacked detection in ALMA in the lowest-redshift bin, $3 < z < 4$. Collectively, we interpret these stacking experiments to indicate that our sample is likely dominated by faint sources with some small level of dust-obscured star formation that is (individually) below the detection limit of ALMA at the low-redshift end, $z < 5$.

The NIRCam imaging is sufficiently deep to have detected lower-luminosity analogs of DSFGs at even higher redshifts of $z \sim 6$–7 (e.g., the serendipitous sources identified in Fudamoto et al. 2021). These ALMA-only sources were thought to have ~ 25–26 AB mag at 4 μm, with obscured SFRs in the range ~ 40–70 $M_\odot$ yr^{-1} (based on $f_{1\ {\rm mm}} \sim 110$–190 μJy) and $\log_{10}(M^*/M_\odot) \lesssim 10.3$. We identify nine sources with inferred properties that are consistent with these, noting that the stellar population modeling for three of those indicate substantially lower specific SFRs relative to those found by Fudamoto et al. (2021). To determine whether, on average, our sources at $6 < z < 8$ may be comparable, we repeat the ALMA stacking for sources in this redshift range, and we find no stacked detection in GOODS-ALMA to a limit of $f_{1.1\ {\rm mm}} = 38 \pm 41\ \mu$Jy beam^{-1} (Figure 3; in ASAGAO, we find $f_{1.1\ {\rm mm}} = -9 \pm 28\ \mu$Jy beam^{-1}, a 1$\sigma$ upper limit that is a factor of 4–7 below the 1 mm continuum detections in that work). This result suggests that our $6 < z < 8$ sample is not actually dominated by similar lower-luminosity DSFGs.

In Figure 4 we explore further whether galaxies are red due to age, dust, or both in the rest-frame $U - V$ and $V - J$ colors of our sources. All sources exhibit substantial dust obscuration
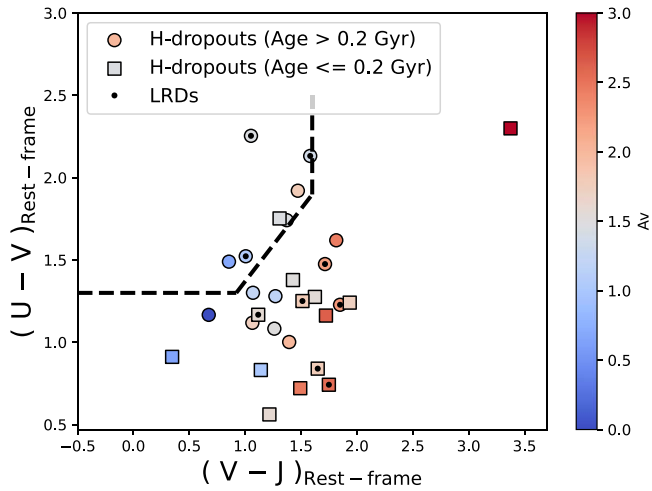
Figure 4. *UVJ* diagram of our MIRI sample. Points are color coded by their inferred A_V and symbol shape indicates old vs. young mass-weighted ages. LRDs are flagged with black dots. We omit the 1σ uncertainties from the modeling posteriors for clarity, noting the uncertainties are large (sources have low S/N near both the rest-frame *U* and *J*) enough to scatter away from the rest-frame colors of quiescent galaxies (dashed black line; Williams et al. 2009). The SEDs are consistent with our sample, including primarily star-forming sources, some with extreme dust obscuration (red in $V - J$), and some candidate older/poststarburst-like SEDs (Balmer breaks are also visible in the SEDs).

($A_V > 0.7$) except one. Although we do not see a strong dependence in A_V with redshift, we note the most extreme sources with $A_V > 2.5$ are all at $z < 6.5$. We also note that by stacking the ALMA data in redshift bins, we find that at $3 < z < 4$ and $4 < z < 5$, the stacks show weak but more significant detections. This is consistent with a majority of the sources we identified at $z < 5$ being faint dust-obscured sources.

While the stacked nondetection in ALMA at $z > 6$ could mean that the level of obscured star formation traced by cold dust is relatively low (i.e., below the ALMA detection limit, $\log_{10}(L_{IR}/L_\odot) < 12$), this is not definitive, and we unfortunately have limited data to further constrain this on an individual-galaxy basis. A lack of ALMA detection could also imply that our sources either (1) contain obscured star formation, but the dust is hotter than is typically assumed at lower redshift (see, e.g., De Rossi et al. 2018), (2) contain hot dust heated by AGN activity, or (3) the galaxies have primarily evolved or older stellar populations. In the following subsections we now explore these possible scenarios.

5.2.2. Possible Evidence of Active Galactic Nuclei among Red Galaxies

To look for AGN evidence, we have matched our sample to the pre-JWST AGN catalog built by Lyu et al. (2022) that has integrated Chandra X-ray, HST optical to near-infrared, Spitzer mid-infrared, and JVLA radio data for a comprehensive search of AGN in the GOODS-S field. In total, we found only two matches among the more extended NIRCam-only sample (Table 2): JADES 171973 and 284527; both of them are identified as AGN by their high X-ray luminosity and X-ray to radio ratio (see details in Lyu et al. 2022). As pointed out in Lyu et al. (2022), the AGN selection is complicated by the survey depth, wavelength range, and object variations, and many AGN are still likely missed.

With the improved sensitivity and wavelength coverage of JWST data, significant progress has been made to identify AGN. Based on a semiempirical SED analysis of MIRI-detected sources with JADES NIRCam and SMILES MIRI photometry, Lyu et al. (2024) have drastically improved the AGN census in the central regions of GOODS-S. For our sample, three new AGN candidates have been revealed from that study: JADES IDs 57356, 106502, and 204851. Notably, ID 204851 has been confirmed to be a broad-line AGN at $z = 5.48$ in FRESCO data (Matthee et al. 2023).

Meanwhile, several groups have demonstrated the existence of fainter broad-line AGNs by selecting sources that feature as LRDs (Labbé et al. 2023a; Greene et al. 2023; Matthee et al. 2023, among other references)—objects with strong red continuum and compact morphologies in the NIRCam bands. Although the nature of these objects is still debated (e.g., Barro et al. 2023), the success rate of AGN searches by this selection has been high (e.g., 9/12 in the sample of Greene et al. 2023 show evidence of broad Hα). While confirmed broad-line AGN may be prevalent among LRDs, it remains unclear whether the AGN dominates the host galaxy, and what its contribution is to the rest-frame UV and rest-frame optical continua. We now apply such selections to our sample and discuss their nature via a color/SED analysis with the addition of MIRI data points at longer wavelengths.

Matthee et al. (2023) describe the LRD selection criteria as relatively flat or blue at observed 1–2 μm, with a (very) red continuum from 2–4 μm. We crosscheck our sample with the following selection criteria for LRDs: $-0.5 <$ F115W – F200W < 1 and F277W – F444W > 1.6 (Greene et al. 2023). Those criteria, based on spectroscopic confirmation of broad-line AGN, should contain an estimated 80% AGN fraction (Greene et al. 2023). We find that 13 out of 66 objects in the NIRCam footprint are candidate LRDs by these criteria (nine of which lie in our MIRI coverage, excluding the probable brown dwarf candidate, ID 190413). Two of the 13 include sources with evidence of an AGN, including ID 204851 (Lyu et al. 2024; Matthee et al. 2023), as well as ID 154428, which show possible evidence of broadened Hα and a weak narrow component in FRESCO data (F. Sun et al. 2024, in preparation). While we do not fold in the explicit compactness cut of Greene et al. (2023) to identify LRDs, we note that all candidates identified by the LRD colors are visibly unresolved, or consistent with point sources, in F444W (including ID 204851, which in the single-band cutouts of Figure 11 appears blended with two neighbors). In general, our F150W – F444W selection does not pick up LRDs systematically, or, similarly, the extremely red object (ERO) selection that was used in Barro et al. (2023; F277W – F444W > 1.5). This is because while the LRDs and EROs are red in the long-wavelength NIRCam filters, some fraction are bluer in the shorter-wavelength ones due to the rising rest-frame UV SEDs. The net result is that the bluer, more "V-shaped" SED sources are preferentially excluded by our *H*-band dropout selection unless combined with a very red rest-frame optical continuum.

5.2.3. Nature of the Little Red Dots in Our Sample

Our LRD subset has distinct SEDs that appear different from most of the *H*-band dropouts. Some LRDs are also poorly fit by, e.g., single-component dusty or quiescent stellar populations. In the literature, this has prompted a number of explorations into differing origins for their blue rest-frame
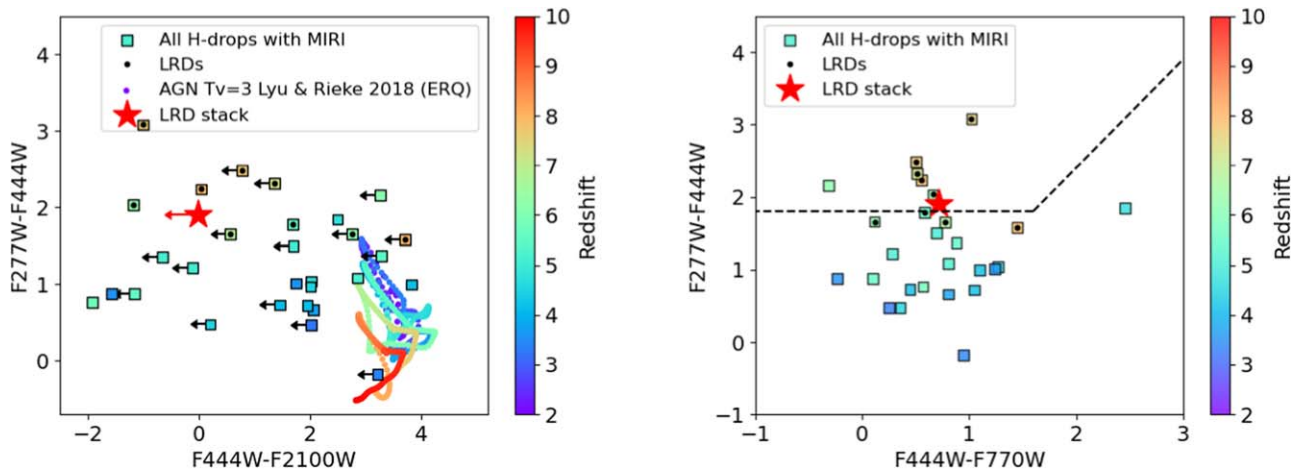
Figure 5. NIRCam–MIRI color–color diagrams for our sample (squares) with the LRDs flagged (black dots). Objects are color coded by redshift. The red star indicates the average color obtained from a median-stacked LRD SED in Figure 6. Left: F277W – F444W vs. F444W – F2100W colors of our sample. For comparison we plot a heavily obscured AGN template from Lyu & Rieke (2018; excluding stellar host) shown to match the red SED of so-called ERQs, which at $z \sim 3$–8 are extremely red in the rest-frame near-infrared. In comparison, LRDs have bluer or flat colors in F444W – F2100W than SEDs dominated by obscured AGN, more similar to SEDs dominated by stellar emission (tracing the stellar bump). Right: F277W – F444W vs. F444W – F770W colors of our sample. Most LRDs are red or flat in F444W – F770W color, inconsistent with an interpretation that emission line boosting in F444W produces the red in F277W – F444W color (which would be blue in F444W – F770W). These colors are more consistent with a flat or moderately rising red continuum driven by starlight (the dashed-line box, specifically the diagonal line, defines the color region at F444W – F770W > 1.5 that excludes heavily reddened AGN continua at $z > 3$; Akins et al. 2023). The NIRCam–MIRI colors in both plots favor SEDs that are stellar in origin.

UV SEDs (Barro et al. 2023; Endsley et al. 2023; Furtak et al. 2023; Greene et al. 2023; Labbé et al. 2023a). On the one hand, the rest-frame UV could be unobscured star formation. Alternatively, it could be scattered light from either hot stars or from an AGN accretion disk (depending on geometry). Similar ambiguity exists over the origin of their very red rest-frame optical SEDs, which could be driven by either obscured AGN continuum or dust-obscured stellar emission. Recently, deep ALMA nondetections for LRDs have provided evidence against a red continuum produced by dust-obscured star formation, because the expected amount of reprocessed dust emission in the far-infrared under typical assumptions (e.g., dust temperatures in the range $T_{\rm dust} \sim 20$–60 K) would be dramatically in excess of the deep ALMA limits (Labbé et al. 2023a). We find similar results for our LRD sample (see right panels in Figure 3). This could point to an AGN-dominant SED with hot dust emission. However, recent studies of compact DSFGs at high redshift indicate that the dust temperature can be significantly higher due to the higher density of star formation (De Rossi et al. 2018; Sommovigo et al. 2020). So, this argument in favor of AGN dominance is not definitive.

MIRI colors of LRDs. Our MIRI photometry enables us to explore whether the LRD/AGN candidates from our sample are plausibly sources whose red rest-frame optical emission is dominated by a heavily reddened AGN (e.g., $A_V \sim 1$–4, based on the shape of the rest-frame optical continuum; Greene et al. 2023). To explore this hypothesis, we plot our sources with MIRI coverage on two NIRCam–MIRI color–color diagrams in Figure 5 along with the redshift evolution in colors for a template dominated by an obscured AGN (i.e., excludes contribution from stars; Lyu & Rieke 2018). From the empirical AGN SED library built by Lyu & Rieke (2018), we choose a model template for a typical (normal) AGN obscured by an extended dust distribution featuring large grains with optical depth $\tau_V = 3$. This template matches the typical SEDs of lower-redshift "extremely red quasars" (ERQs; Ross

et al. 2015; Hamann et al. 2017) that have similarly red F277W – F444W colors as our LRD/ERO sample.

Looking at the observed colors, we find that all of our LRD candidates exhibit a turnover in their SED redward of F444W, between rest-frame 0.5–3 μm. This turnover results in a blue or flat F444W – F2100W color that is inconsistent with obscured AGN templates, which show a steeply rising shape at longer wavelengths (e.g., Lyu & Rieke 2022). These colors instead favor a scenario where the rest-frame optical emission between 0.5–3 μm rest frame is dominated by the continuum from the stellar population. This is potentially the spectral signature of the stellar bump at rest-frame 1.6 μm (caused by a minimum in the H opacity in the atmospheres of cool and low-mass stars that dominate the near-infrared spectra of galaxies with ages > 10 Myr; e.g., Sawicki 2002). Reddened AGN, in contrast, typically exhibit a steeply rising red continuum redward of rest-frame 1.6 μm, tracing hot dust emission from a torus (Alexander & Hickox 2012; Lyu & Rieke 2022).

Average MIRI SED of the LRDs. While the MIRI data are deep enough to rule out a rising red continuum from a dominant AGN for individual sources, the majority of the LRD subset are not detected in the longer-wavelength filters. To obtain a stronger constraint on the MIRI colors (on average) we median stack the MIRI imaging for the LRD subset. For this experiment we also include the 25 μm band (F2550W), which otherwise is shallow relative to the other filters, but on average, can provide a meaningful constraint at rest-frame wavelengths > 3 μm. The MIRI stacks are shown in the top panel Figure 6.

We measure average aperture photometry using the stacked MIRI images following the same procedure as Section 4. On average, the sample remains undetected at wavelengths > 18 μm, even in the deeper stacked image. For an accurate comparison to the average NIRCam SED of LRDs, we also calculate the median and interquartile ranges of the LRD photometric points (in lieu of stacking the NIRCam images, since all sources are already strongly detected in the NIRCam
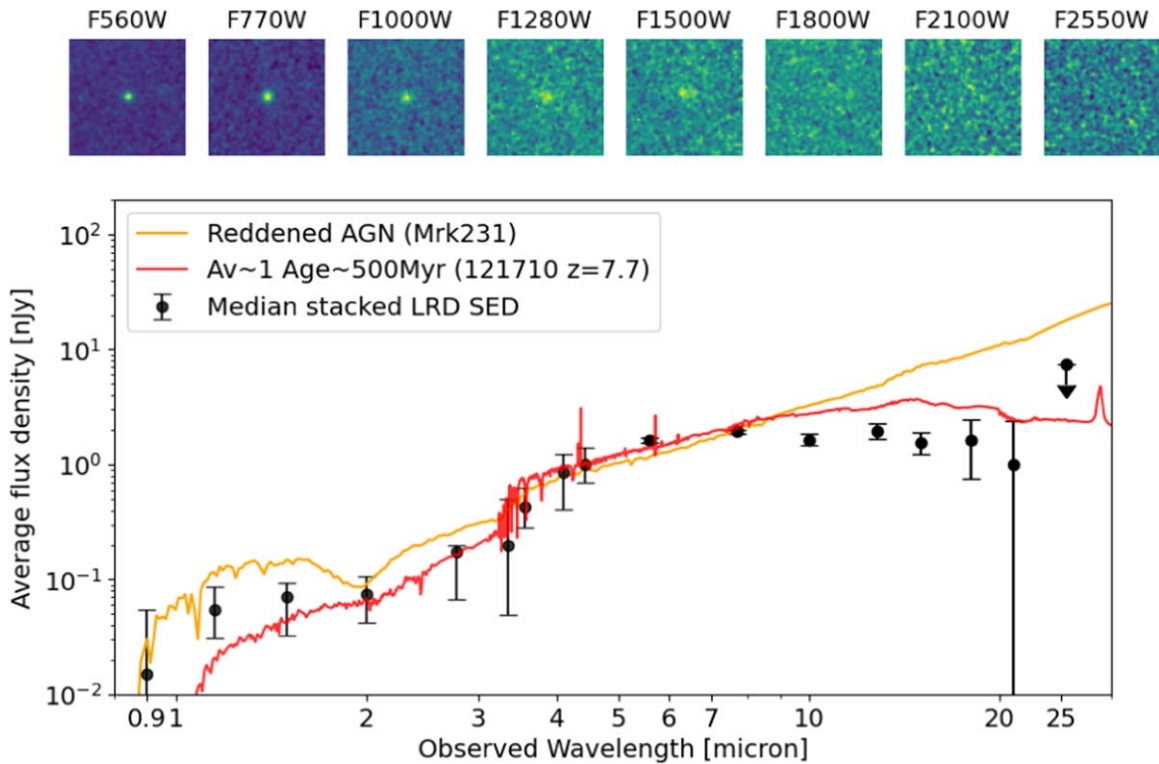
Figure 6. Top panel: stacked MIRI images from 5.6–25 μm of the LRD subset of H-band dropouts (3.6" on a side). Bottom panel: stacked observed SED of the LRD subset, where the NIRCam points are the median and interquartile range of the measured photometry, and the MIRI points are measured from the median-stacked imaging in the top panel. The stacks are consistent with flattening of the rest-frame near-infrared SED that was observed in the forced photometry of individual sources. They are not consistent with rising mid-infrared flux from a dust-obscured AGN (e.g., Mrk 231; Polletta et al. 2007) and are a better match to stellar models of moderate dust and age (red).

F444W filter). The full median-stacked SED for the sample of LRDs is shown in the bottom panel of Figure 6. For comparison, we also plot two example SEDs: one for a reddened quasar and its host galaxy, placed at the median redshift of our LRD sample (Mrk 231; Polletta et al. 2007) and a `prospector` best-fit model that is representative in shape of a number of our LRDs among the H-band dropout sample (ID 121710). It is immediately clear that the turnover in the median MIRI SED strongly disfavors a reddened AGN shape, and instead agrees better with the moderately dusty and moderately old stellar model describing ID 121710 (mass-weighted age $\sim$ 500 Myr, $A_V \sim 1$). Notably, we find that the limits in the color from the median stack indicate that the SEDs of our sources must be quite flat between F444W and F2100W, with color F444W – F2100W ~ 0 (and even consistent with a blue color, i.e., a turnover, given the lack of a significant stacked detection in F2100W).

Evidence for emission line boosting versus AGN continuum in LRDs. Emission line boosting in F444W could also generate red F277W – F444W with blue F444W – F2100W colors, either from [O III] + Hβ at $z > 7$ or Hα at $z \sim 5$. To explore this possibility, we also plot the rest-frame optical colors versus F444W – F770W (right panel of Figure 5), which should be very blue if F444W is boosted by emission lines (note that we choose F770W because F560W can also be contaminated by Hα emission when [O III] + Hβ is in F444W). We find that the majority of the LRDs have weakly red or flat F444W – F770W colors, suggesting that the F277W – F444W color is not red due to significant line boosting in F444W. We additionally find that the median SED color of F444W – F770W = 0.7, which is not consistent with the idea that F444W – F2100W is blue or

flat in spite of a red continuum because of strong emission line boosting F444W. These colors also suggest that the red rest-frame optical colors are dominated by stellar emission and not obscured AGN emission (which would predict a continual red rise into the mid-infrared from an AGN continuum rather than a turnover from the stellar bump). However, the colors cannot rule out an obscured mid-infrared-dominant AGN whose continuum begins to dominate the SED at rest-frame wavelengths > 3 μm.

We note that the theoretical AGN templates provided with `prospector` may not correspond fully to reality; an alternative approach uses empirically based templates (see the review by Lyu & Rieke 2022). To explore this approach, we run `prospector` on our full sample while using a modified and more realistic mid-infrared AGN template set (Lyu & Rieke 2018). We follow the `prospector` setup as outlined in Lyu et al. (2024). We find that, in line with our exploration of the NIRCam–MIRI colors, the contribution to the rest-frame 0.5–3 μm continuum of LRDs is not obviously dominated by an obscured AGN. In reality, individual sources may exhibit a broad variety of behavior near rest-frame 3 μm (where the presence of a mid-infrared AGN is expected to be most obvious among typical star-forming galaxies), and the analysis is complicated by the effect of strong emission lines and the low S/Ns of the longest-wavelength MIRI data.

Further, we do a similar exploration using CIGALE (Boquien et al. 2019), which for samples in the literature has found that the steep slopes of the rest-frame optical continua of LRDs have a preferred origin from AGN continua, based on HST + NIRCam photometry alone. For this experiment we use the `SKIRTOR` AGN model, a clumpy two-phase torus model

from Stalevski et al. (2012, 2016). We find that, in nearly all cases (for the LRDs) CIGALE prefers fits where AGN continuum dominates the SED between rest-frame 0.5–0.8 μm, but these AGN-dominant models significantly overpredict the MIRI-observed SED at F1800W – F2100W by a (median) typical factor of 25–40 (well in excess of the photometric uncertainties). We also find that CIGALE overpredicts the MIRI photometry for the parent H-band dropout sample, although to a lesser degree for non-LRDs (factor of 2–3). This is likely driven by the redder rest-frame optical (F277W – F444W) color of our subset of LRDs compared to the parent sample of H-band dropouts (see left panel of Figure 5).

Thus, we would find similar conclusions based on HST + NIRCam photometry alone as the AGN-dominant solution identified by other studies in the literature. This highlights that while LRDs may be redder in the rest-frame optical than the non-LRD H-band dropout sample, the MIRI data demonstrate that these SEDs are in fact mostly quite similar in the rest-frame near-infrared, suggesting a stellar origin for both subsets of H-band dropouts (see the right panel of Figure 5).

Given the consistency of the rest-frame optical and near-infrared SEDs with dust-obscured stellar emission, it remains puzzling why this does not translate to brighter far-infrared emission from reprocessed energy by dust. To explore this further, we stack the 1.1 mm ALMA imaging covering our nine LRDs from the GOODS-ALMA program (Franco et al. 2018) to obtain an average far-infrared flux (see Figure 3). We find that the 1.1 mm flux is not detected (3 ±37 μJy beam^{-1}). Similarly low stacked ALMA limits disfavoring dust-obscured star formation were found in Labbé et al. (2023a). It remains plausible that compact star formation at high redshift and low metallicity could heat dust well above typical expectations, and we discuss this scenario further in Section 6.1.

5.2.4. Evidence for Older Stellar Populations in Our Sample

Such a low far-infrared flux measured in the ALMA stacks is consistent with a primary result from the SED modeling, which is that a large fraction of LRDs in particular are preferred to have older stellar populations over high levels of dust-obscured star formation. This is presumably, at least in part, a result of prospector trying to account for these deep upper limits from ALMA (given the fixed low dust temperatures assumed by the modeling). This possibility of quiescent SED solutions for LRDs was also explored in Labbé et al. (2023a), however that work determined that the extremely red rest-frame optical continuum slope disfavored a purely quiescent stellar population. However, we find that an older and evolved stellar population (mass-weighted age > 200 Myr), in combination with significant dust attenuation ($A_V > 1$), adequately fits the SEDs of a number of H-band dropouts, as well as a large fraction of our LRD subset. This is demonstrated in Figure 4, which shows that a number of our LRDs reside near the UVJ quiescent box (Williams et al. 2009; Muzzin et al. 2013). The typical level of dust attenuation that we infer is relatively high. However, owing to their faintness, we note that the uncertainties in the rest-frame colors near both the rest-frame U and J part of the SED are quite large. Thus, we caution against overinterpretation of the location of our sources in the UVJ diagram.

Regardless of the large errors in rest-frame U and J, we note that a number of the LRD SEDs with red $U - V$ and $V - J$ colors also exhibit clear evidence at high significance for strong Balmer breaks (e.g., IDs 121710, 132229, and 219000 and perhaps also 154428) as does one non-LRD, ID 200576. The Balmer break evidence is clear in part due to the NIRCam medium-band images, which at F182M, F210M, and F335M are finely sampling the spectral region near 4000 Å across our entire redshift range. These strong Balmer breaks (all at early cosmic time, $z > 5.5$) are remarkable, in particular because we simultaneously can rule out that the breaks are degenerate with strong line emission or AGN contamination with the 4 μm medium bands and MIRI data. We will discuss their implication later in Section 6.2.

We note that for ID 154428 in particular, in addition to having evidence of a Balmer break, the FRESCO detection indicates possible evidence of broadened Hα with a weak narrow component, which could indicate a weak optical AGN (e.g., similar to the broad Hα in the quiescent galaxy confirmed at $z = 4.6$ in Carnall et al. 2023). Unfortunately, we are unable to robustly rule out the presence of a broad-line region in the other sources with FRESCO coverage, since any broad components may be dust obscured and below the FRESCO detection limit. We have stacked the FRESCO grism spectra of sources without a broad Hα detection. This sample includes four sources at $z \sim 5$ and three sources at $z \sim 7$ such that the Hα and Hβ lines are within the wavelength coverage of the FRESCO F444W grism spectra, respectively. No broad Hα or Hβ component can be robustly detected because of the limited sensitivity enhancement. The 3σ upper limit of broad Hα line luminosity is $\sim 4 \times 10^{41}$ erg s^{-1} assuming a broad-line FWHM of 1000 km s^{-1}, and therefore we cannot rule out the presence of AGN with black hole masses $M_{BH} \lesssim 10^{6.5} M_\odot$ in these $z \sim 5$ sources (assuming the Reines et al. 2013 calibration of the single-epoch spectroscopic black hole mass).

To summarize, the MIRI colors of AGN-dominated objects should be red, however, since we do not find evidence for that, we suspect that the light is instead dominated by stars. However, the conclusion that the LRDs in our sample are dominated by stellar emission is not definitive. In Section 6, we will show results including and excluding these sources from the sample, and discuss these results in the context of the assumption that these galaxies are dominated by stellar emission.

5.2.5. Excess Ultraviolet Emission

As a final note, we discuss the apparent presence of a rest-frame UV "excess" in a handful of our sources: flux which is not easily modeled without a secondary SED component (either by unobscured star formation or scattered UV light from an AGN). We find clear evidence that composite SEDs are needed to explain the flat UV slopes in a number of objects (IDs 90354, 120484, and 203749; and potentially also 81400, 132229, and 183348). Our selection based on very red F150W – F444W colors may have rejected a number of LRDs with more obvious needs for composite SEDs. The slopes of the UV SEDs are at low S/N, but nonetheless consistent with typical slopes of either AGN or young stars (see the discussion in Greene et al. 2023). Thus we cannot rule out models that have been proposed for similar sources with our data (Barro et al. 2023; Labbé et al. 2023a; Matthee et al. 2023). Spectroscopy has now confirmed that the continuum slope

alone cannot easily differentiate between a star-forming or AGN origin using similar samples (Greene et al. 2023) nor their intrinsic luminosity (which is degenerate with the fraction of light scattered). Thus we cannot hope to do better with photometry, and take the presence of excess UV emission as an indication that scattered light from either an AGN or star formation may contribute. We note that, if the origin of the UV flux is indeed from a frosting of unobscured star formation, the amount of star formation is very small (i.e., these objects are barely detected in the very deep JADES imaging, and we measured the typical implied SFR(UV) based on the flux to be $<1\ M_\odot\ \mathrm{yr}^{-1}$). Thus any assumption about the origin of the UV flux will not impact our results in Section 6.1. Pursuing an explanation for the UV emission is outside the scope of this paper.

6. Discussion: What Fraction of the Galaxy Census Was Missed Due to "Dark" Galaxies?

In this section, we explore how these previously missed galaxies may contribute to the star formation and stellar mass budget of the early Universe from $3 < z < 8$, a regime that was previously incomplete among infrared measurements, and which could not be probed uniformly with earlier data. Given the results of Section 5.1, for this section we only consider sources for which we have MIRI and ALMA constraints, since we find major uncertainties that can change the mass and SFR estimates by up to 1 dex if we have only HST + NIRCam photometry.

6.1. The Cosmic Star Formation Rate Density

Here we estimate the cosmic SFRD contribution from these sources (a previous estimate has been made for a similar sample by Barrufet et al. 2023b; we now include submillimeter and MIRI data that improve the SFR constraints compared to the HST + NIRCam data; see Section 5.1). Given that our sources are relatively bright in the detection band compared to the very deep JADES imaging (F444W S/N > 20) and the relative depths of our F444W and F150W imaging (Eisenstein et al. 2023b) we find we are sensitive to colors F150W − F444W < 3.2 even for the fainter sources that are not detected at F150W. Thus, we expect that the selection of H-band dropouts is complete for sources brighter than our limiting F444W AB magnitude of 29.4.

We do a simple estimate of the total SFRD by summing the total SFR among our sample (i.e., the SFR during the most recent 30 Myr, as derived from our SED modeling) divided by the cosmic volume within several redshift bins: $z \sim 3.5, 4.5, 5.5,$ and 7 (with $\Delta z \sim 1$, except for the highest redshift bin, which has width $\Delta z \sim 2$). Without completeness our measurements should be considered lower limits, although we pick a high S/N where we are likely complete in both magnitude and color.

These results are shown as red circles in Figure 8, and are compared to the obscured SFRD and unobscured (and not dust-corrected) SFRD from the MORA survey (orange and blue curves; Casey et al. 2021; Zavala et al. 2021). First, we find that at $3 < z < 4$, optically faint galaxies make up a relatively small fraction of the obscured contribution to the SFRD. This is similar to Cosmic Noon where the SFRD is still dominated by brighter sources such as submillimeter galaxies (e.g., Dudze-vičiūtė et al. 2021), and is consistent with earlier findings (e.g.,
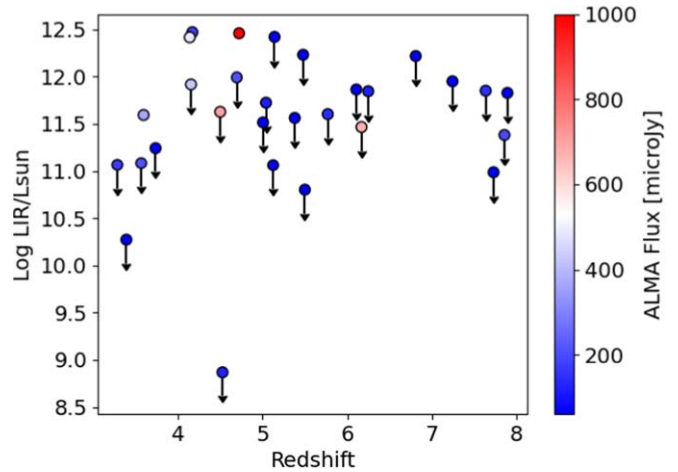
Figure 7. $\log_{10}(L_{IR}/L_\odot)$ vs. redshift of our sources with MIRI coverage that go into our estimate of the cosmic SFRD. For comparison, the average rms limit of the ASAGAO imaging used is 60 μJy and for GOODS-ALMA it is 180 μJy. The majority of sources are inferred to be upper limits to $\log_{10}(L_{IR}/L_\odot)$ based on their nondetection upper limits from the ALMA imaging.

Wang et al. 2019; Sun et al. 2021). However, at $4 < z < 6$, we find that the missing population identified by our H-band dropout selection likely contributes nonnegligibly to the obscured fraction of the SFRD. We find that in these two redshift bins, our full sample is comparable to the total obscured fraction of cosmic SFRD characterized using existing ALMA and far-infrared observations (orange line).

Since ALMA and far-infrared detections become sparse at $z > 3$, the orange region representing the obscured SFRD is measured by combining individual bright detections along with an extrapolation of the infrared luminosity function to faint infrared luminosities (Zavala et al. 2021). Since the shape of the infrared luminosity function at such early times is relatively uncertain (in particular at the faint end, $\log_{10}(L_{IR}/L_\odot) < 11$, where a number of studies report significant differences; e.g., Koprowski et al. 2017; Gruppioni et al. 2020; Zavala et al. 2021; Barrufet et al. 2023a; Fujimoto et al. 2023a; Traina et al. 2024), our data provide an opportunity to compare the contribution of populations below ALMA's detection limits to that typically extrapolated from the luminosity function.

To make this comparison, we put our sample in context of existing far-infrared measurements at $z > 3$ and estimate their total infrared luminosity by integrating the maximum like-lihood `prospector` model between rest-frame 8–1100 μm. We then convert this to SFR using the indicator based on the total infrared luminosity of Kennicutt & Evans (2012). We find that almost all of our sources are below the detection limits of earlier submillimeter surveys at $z > 3$, with the majority of our sample having upper limits to L_{IR} of $9 < \log_{10}(L_{IR}/L_\odot) < 11.8$ (see Figure 7). We have only four detected sources with a confirmed ALMA flux consistent with $\log_{10}(L_{IR}/L_\odot) > 12$. Since many of our objects are nondetections (and thus upper limits), we are likely reaching the "extrapolation" regime ($9 < \log_{10}(L_{IR}/L_\odot) < 11$) of the dust-obscured SFRD at $z > 3$ (Zavala et al. 2021).

We focus more specifically on sources with $\log_{10}(L_{IR}/L_\odot) < 12$, to make a direct comparison with the contribution from similar luminosity populations in Zavala et al. (2021). That work determined that from $4 < z < 7$, the fraction of the obscured SFRD contributed by $\log_{10}(L_{IR}/L_\odot) < 12$ sources was relatively small (20%) and this fraction was flat with redshift. To compare,
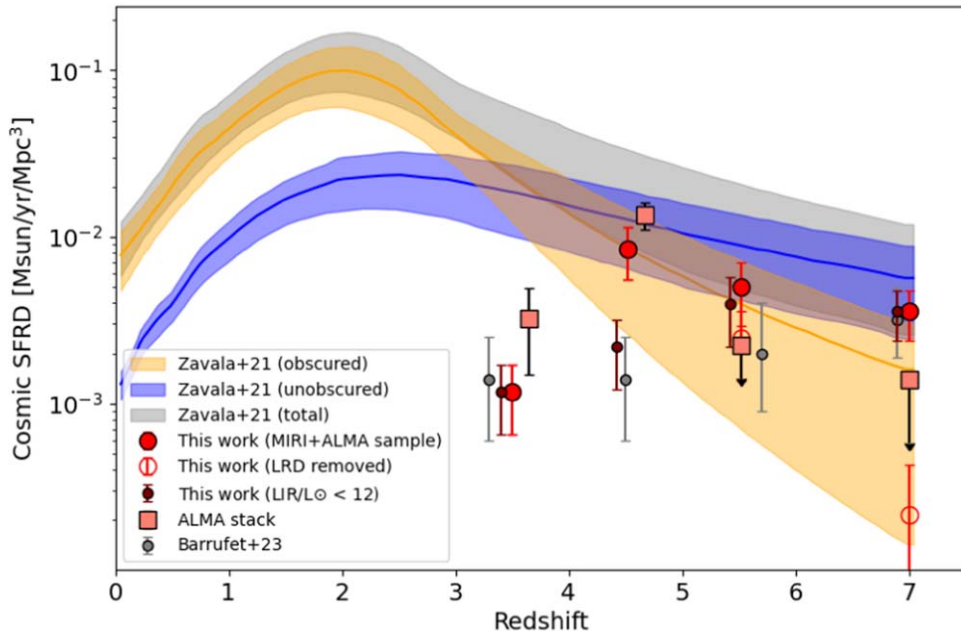
Figure 8. The cosmic SFRD of our full *H*-band dropout sample in the MIRI footprint (red points). For comparison we show far-infrared measurements (obscured SFRD; orange shaded region) based on Zavala et al. (2021), along with the UV-based compilation in that work (unobscured, uncorrected for dust; blue shaded region). We also plot the SFRD contribution from our sources with $\log_{10}(L_{IR}/L_{\odot}) < 12$ (maroon points). Although our MIRI data suggest our LRD subsets are stellar dominated, we show the SFRD when removing them since their nature is uncertain (open red circles). We also include an estimate based on the average ALMA flux from stacking the 1.1 mm imaging scaling with a hotter dust template (peach squares).

we also plot the SFRD contribution from our subset of sources with $\log_{10}(L_{IR}/L_{\odot}) < 12$ (maroon points in Figure 8). We find that our measurements indicate that $\log_{10}(L_{IR}/L_{\odot}) < 12$ sources make up a higher fraction of the obscured SFRD (26%) at $4 < z < 5$, compared to 20% estimated by Zavala et al. (2021; a relatively minor factor of 1.3 increase). However, at $z > 5$, the fractional contribution from sources with $\log_{10}(L_{IR}/L_{\odot}) < 12$ is much larger, and is comparable with the total obscured SFRD previously estimated. Compared to the earlier estimate of flat 20% fraction from $\log_{10}(L_{IR}/L_{\odot}) < 12$, this suggests that the contribution of $\log_{10}(L_{IR}/L_{\odot}) < 12$ sources could be underestimated a factor ~ 5 at $z > 5$. In comparison to the total obscured contribution from (Zavala et al. 2021, orange curve), a factor of 5 increase in the contribution from $\log_{10}(L_{IR}/L_{\odot}) < 12$ sources could double the obscured fraction of the SFRD at these redshifts.

While we note that major uncertainties exist in our measurements (see next section), our data indicate that the overall census of dust-obscured star formation from earlier studies could be underestimated. Our findings are consistent with and similar to the estimates based on pre-JWST data sets that find a higher SFRD at early times (Algera et al. 2023; Fujimoto et al. 2023a; Traina et al. 2024), in particular when including estimates based on the existence of optically faint or various "dark" sources (Williams et al. 2019; Gruppioni et al. 2020; Talia et al. 2021; Enia et al. 2022; Shu et al. 2022).

Based on our data, it may also be the case that the dust-obscured star formation is underestimated at $z > 6$. We find that at $z \sim 7$ the SFRD derived using the SED modeling is $\log_{10}\rho_{SFR} = -2.44^{+0.12}_{-0.18}\ M_{\odot}\ \mathrm{yr}^{-1}\ \mathrm{Mpc}^{-3}$. This is consistent with Algera et al. (2023), but in excess of the estimates in both Zavala et al. (2021) and Barrufet et al. (2023a). However, the fraction of our sources which are classified as candidate LRDs at these redshifts by color selection is high. While our analysis in Section 5.2.2 indicates that the NIRCam and MIRI photometry used to measure their stellar populations is not

dominated by light from AGN, as a conservative estimate we also calculate the SFRD assuming the star formation contribution of these candidate AGN cannot be robustly determined. Thus we plot a second estimate with these LRD sources removed (open red circles). We find that in doing so, at $z > 6$ the obscured SFRD is substantially lower than implied by previous studies using NIRCam and HST data alone (Barrufet et al. 2023b), and that the obscured SFRD contributed by our own sample of dark galaxies would be substantially lower. We thus caution against overinterpretation of this measurement, and note that a complete assessment of the SFRD at $z > 6$ from dust-obscured star formation using JWST-selected samples will likely remain uncertain until we understand the true nature of LRDs.

6.1.1. Impact of Modeling Assumptions on the Cosmic Star Formation Rate Density

Despite the panchromatic data and limits used in our SED fitting, our `prospector`-based SFRs may still be underestimating the intrinsic amount of SFR due to the model assumptions used to infer obscured star formation (namely, that the dust emission model assumed by `prospector` inherently prefers cold dust temperatures at the default prior settings). However, a wealth of evidence now points to hotter dust temperatures among compact, low-metallicity systems that make up a higher fraction of the population at high redshift ($T_{dust} \sim 40$–60 K; e.g., Faisst et al. 2017; Behrens et al. 2018; De Rossi et al. 2018; Schreiber et al. 2018; Bakx et al. 2020; Sommovigo et al. 2020, 2022). The effect of assuming a colder dust temperature is to underestimate the SFR, since at a fixed 1.1 mm flux, the obscured SFR can be higher if the dust is hotter. While we have adjusted our priors to allow higher dust temperatures (our `prospector` fits yielded a typical $T_{dust} \sim 37$ K), this is still below some empirical constraints from dusty galaxies at high redshifts.

Thus, to test the impact of hotter dust on our estimates, we return to our ALMA image stacking that we used to estimate the average 1.1 mm flux in the various redshift bins (see Section 5.2.1). Now including the detected sources in the stacks in order to assess the true average flux per bin, we find that in the above redshift bins, the stacked fluxes are 83 ± 44, 213 ± 39, 2 ± 48, and 25 ± 38 μJy beam^{-1}, respectively. However, to interpret the stacked 1.1 mm flux, we now assume a hotter dust SED template. To estimate the corresponding average L_{IR}, we scale a far-infrared template for Haro 11, an analog for a high-redshift DSFG that factors in elevated dust temperatures that more realistically describe compact SFGs at $z > 4$ ($T_{dust} \sim 47$ K, emissivity index $\beta \sim 1.9$; Lyu et al. 2016). To obtain L_{IR} and SFR we integrate the template scaled to the ALMA stacked flux and integrate between rest-frame 8–1100 μm and convert to SFR as earlier.

We find that our stacked ALMA fluxes are consistent with $\log_{10}(L_{IR}/L_\odot) = 11.6$, 12, <10, and <11 for redshifts $z \sim 3.5$, 4.5, 5.5, and 7, which correspond to average SFRs that are 69 ± 37, 152 ± 28, 1 ± 31, and 15 ± 23 $M_\odot$ yr^{-1} per redshift bin. For comparison, the average SFR per bin based on the `prospector` SED modeling is similar within 2σ (and consistent within 1σ at $z < 5$, although systematically underestimated). Using the number of galaxies per redshift bin, we translate these average estimates derived from the ALMA stack to an estimate of the total SFR per redshift bin contributed by this sample, scaled to the same S/N as reflected in the image stacked flux (see the peach squares in Figure 8). For the two highest redshift bins where a stacked flux is not detected, we instead plot 1σ upper limits. Generally, we find that at $z < 5$ the hotter dust template does increase our measured SFRD, which is expected since the stacked flux is converted to an average SFR using a hotter dust template than the typical dust temperature that was fit with `prospector`. Meanwhile, at $z > 5$ the stacks point to a lower SFRD than found with the SED modeling. At $z > 5$, we interpret the larger SFRD returned by `prospector` as likely reflecting that the individual ALMA nondetections are not deep enough to constrain the (lower) SFR of any given object. With the deeper stacks it becomes clear that, even assuming a template with a hotter dust temperature, the contribution from these objects must be lower than inferred by `prospector`. More data that samples the far-infrared SED to constrain the dust temperature would be needed to resolve the discrepancies between the different measurements.

One potential downstream impact of `prospector` not allowing for hotter dust in the modeling is that it likely forces a more quiescent (redder) stellar population solution (which, due to higher mass-to-luminosity ratios of older stars could result in higher mass solutions at fixed luminosity). We note that redder stars is an easy solution to justify in cases where we identified clear Balmer breaks indicative of older stellar populations. However, in cases without clear breaks, we may need dust emission modeling with hotter dust more typical of dusty galaxies observed at similar redshifts. However, we note the dust temperatures required may be even hotter (e.g., De Rossi et al. 2018), given the extremely compact nature of the objects in our $z > 6$ sample. In fact this parameter space (young compact star-forming regions driving hot dust temperature) is seen in the nearby Universe, and could potentially be analogous to these sources (e.g., Hainline et al.
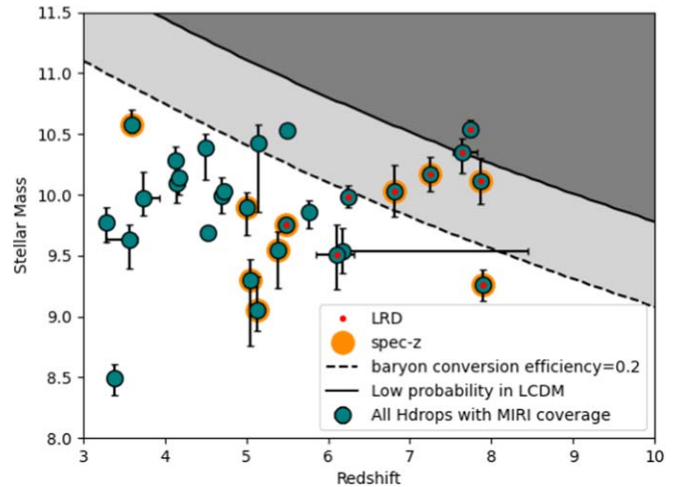
Figure 9. The stellar masses vs. redshift of our sample of galaxies with MIRI coverage (34 arcmin^2 area). For context we include the limiting stellar mass expected for a 100% baryon conversion efficiency (solid line) and 20% efficiency (dashed line). For six galaxies between $z \sim 5.5$ and 8 we measure stellar masses that likely exceed expectations for a small area, even after the stellar masses have decreased by up to an order of magnitude by including MIRI + ALMA data (see Figure 2). This comparison to the expectation curves from halo abundance and star formation efficiency show these measurements are likely still overestimated.

2016). Thus, there is likely to be a significant bias at high redshift (where our sizes are also the most compact) that would mean that these estimates of SFRs are biased low for $z > 5$. This is because galaxies are more difficult to detect based on their 1.1 mm emission than they would be if local (colder) far-infrared SEDs are used (see also Shivaei et al. 2022). Thus, our estimated contributions to the cosmic SFRD may also additionally be underestimated. Additional higher-frequency dust continuum imaging that would constrain the dust temperature would be needed to investigate this possibility further.

6.2. Stellar Mass Census: The Abundance of Massive Galaxies

Despite the findings in Section 4 that MIRI + ALMA data overall result in lower stellar masses, we still identify a remarkably large number of galaxies (16) above $z > 3.5$ with $\log_{10}(M^*/M_\odot) > 10$. The MIRI data also cover a relatively small area of 34 arcmin^2, making the identification of so many massive galaxies unlikely. In fact, 80% of our objects above $z > 7$ have $\log_{10}(M^*/M_\odot) > 10$. It has already been pointed out by Narayanan et al. (2023) and Whitler et al. (2023) that stellar masses are essentially unconstrained above $z > 7$ (and can dramatically over- or underestimate stellar mass) owing to outshining of older stars by young low-metallicity stars complicating the reconstruction of the SFH. However, we note that our high-redshift sources are not particularly young (as `prospector` preferred to model them with older stellar populations, either to allow low dust content to fit the ALMA data, or to accommodate clear Balmer breaks in a number of sources). However, even at redshifts below this problematic epoch noted by Narayanan et al. (2023), the number of high-mass objects is also surprisingly, and problematically, high.

To demonstrate this, we show the stellar mass versus redshift for our MIRI + ALMA sample in Figure 9. For context, we also plot the expected stellar mass limit (i.e., mass where we only expect one halo, given our MIRI survey area), based on

the halo mass function evolution with redshift. To estimate this we use the halo mass function calculator `HMF` published by Murray et al. ([2013](#)) and assume the halo mass function of Behroozi et al. ([2013](#)). We use the limiting halo mass to convert to a limiting expected stellar mass by assuming a fiducial baryon conversion efficiency into stars (0.2, dashed line), and for the limit where 100% of baryons are converted into stars (solid line). While our sample size is small, these curves help to indicate the number of sources whose mass is probably physically unlikely, under the typical assumptions of ΛCDM. We find one source at $z = 5.5$ and five sources at $z \gtrsim 6.5$ that are either improbably high mass, or imply an extremely efficient baryon conversion ($>20\%$) compared to typical assumptions.

In Sections [2.3.3](#) and [4](#) we noted that a number of the photometric and spectroscopic solutions allowed revision to lower redshift upon detailed inspection (thus also allowing further reduction in the stellar masses even after inclusion of MIRI + ALMA data). However, in particular for the high-mass objects, IDs 90354, 121710, 200576, and 219000, we were unable to justify the possibility of lower-redshift solutions. Further, while we identified a tentative emission line for ID 132229 (where the spectroscopic solution is $\Delta z \sim 1$ lower in redshift than the photometric redshift inferred with `prospector`), this galaxy still remains at a problematically high mass. We note that the last photometric candidate with unprobably high mass, ID 203749, has an uncertain redshift solution (we identified two comparable solutions at $z = 2.41$ and $z \sim 7$, the latter we use for the analysis; we note that its LRD colors and unresolved morphology would make it an outlier among known $z < 3$ galaxies). Both redshift solutions are poor fits to the rest-frame UV photometry due to the presence of UV excess (Section [5.2.5](#)). While we do not understand the nature of this object, we conclude it is likely to have alternative explanations besides being a massive high-redshift object and do not consider it in the following discussion.

For the other five objects with less redshift ambiguity however (all are LRDs except ID 200576, and are relatively red) we find that under typical SED-modeling assumptions, these galaxies remain well above the stellar mass expectations for their redshifts. None of them are well fit with the Sonora Cholla brown dwarf atmospheric models, as their 2–3 μm colors are redder than what are observed in ultracool dwarfs. Three of these sources also meet the double-break criteria used to identify extremely massive candidates in Labbé et al. ([2023b](#)), and exhibit clear evidence of Balmer breaks (as discussed in Section [5.2.4](#)). In fact, they all have very similar rest-frame SED shapes, with a strong Balmer break, a clear turnover at 1.6 μm due to the stellar bump, and with deep ALMA limits, are best fit by moderately aged (mass-weighted age $\sim$ 500 Gyr) and dusty ($A_V \sim 1$) SEDs (see Figure [10](#)). Due to our excellent wavelength sampling including at least four NIRCam medium bands and seven MIRI bands, it is extremely unlikely we would not be able to account for emission line boosting. All except ID 90354 exhibit significant MIRI detections even out to 10 μm, making it less possible that we still overestimated the rest-frame near-infrared continuum due to having only upper limits from MIRI.

While there exists the possibility that these stellar masses are accurate, and these objects trace a population of galaxies that demonstrate highly efficient mass growth (e.g., Boylan-Kolchin [2023](#); Labbé et al. [2023b](#); Xiao et al. [2023a](#)), we
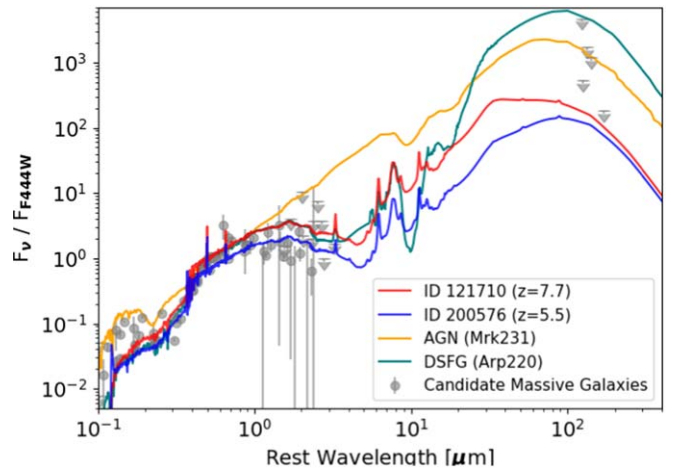
Figure 10. The normalized rest-frame SEDs of the five most confident candidate massive galaxies in Figure [9](#), which include four LRDs, plus a Balmer break non-LRD, at $z \sim 5.5$–8 (gray points; ID 203749 is excluded). All sources exhibit similar double-break SEDs exhibiting well-constrained Lyman and Balmer breaks, evidence for a turnover at 1.6 μm, and are consistent with a high mass-weighted age ($\sim$500 Myr) and moderate dust ($A_V \sim 1$). Shown for comparison are a dust-reddened AGN (yellow) and a DSFG (teal; Polletta et al. [2007](#)). While all SED types look very similar in the rest-frame optical (probed by HST + NIRCam) the SEDs diverge at $\lambda_{rest} > 1$ μm, where MIRI shows a clear flattening due to the stellar bump, and ALMA rules out cold dust emission.

offer a few other possible explanations that would require additional data to disentangle. We note that five out of the six high-mass sources are LRDs, and there remains large ambiguity about the nature of such objects. However, despite the evidence presented in Section [5.2.2](#) that the rest-frame optical SEDs are not dominated by a rising AGN continuum, it remains possible that the redder rest-frame optical SEDs of LRDs are (still) poorly described by stars alone. There is also the obvious possibility that various stellar population assumptions are incorrect at higher redshift (i.e., locally calibrated models do not apply to high-redshift phenomena where the stellar properties and environmental conditions may be dramatically different). Below we outline a few hypotheses based on the potential impact of AGN and modeling assumptions that could be tested with future high-resolution spectroscopy.

6.2.1. Subdominant Active Galactic Nucleus Contamination

One possibility is that some subdominant (but perhaps still impactful) fraction of AGN flux in the rest-frame optical and near-infrared is still driving up the stellar mass estimates of these four LRDs (ignoring for now ID 203749 with an ambiguous redshift). We showed in Section [5.2.2](#) that the CIGALE modeling of the rest-frame optical SED of LRDs predicted much larger discrepancies with the MIRI data, primarily due to their redder NIRCam long-wavelength photometry. The AGN model that overpredicted the MIRI flux included two components: blackbody emission from the accretion disk in the rest-frame optical (e.g., a "big blue bump"), plus hot + warm dust emission in the near- and mid-infrared. While we have shown that the strongly rising continuum from the hot + warm dust emission component does not agree with our MIRI data, this does not directly constrain the contribution from an accretion disk, unless the relative contributions are physically linked. However, some

examples exist where the relative contribution of an accretion disk could be larger than we assumed (e.g., hot or warm dust-deficient AGN; Lyu et al. 2017). In that case, the blackbody emission from an accretion disk could still contribute a small fraction of light to the rest-frame optical without being so visible in the rest-frame near- to mid-infrared. This could be plausible (and could be an explanation given the high confirmation fraction of broad-line AGN among LRDs with these colors; Greene et al. 2023) but we do not have the data or evidence to determine whether this is the case. AGN contribution from an accretion disk is not definitively ruled out by our relatively flat MIRI SEDs. This could in part explain the large inferred stellar masses. We are not aware of analogous sources at lower redshifts, except for dust-deficient quasars.

Recently, similarities have been drawn between JWST-discovered sources with blue rest-frame UV colors ($\sim$0 mag) and red rest-frame optical colors ($>$1.5 mag; e.g., Barro et al. 2023; Matthee et al. 2023) with so-called blue-excess dust-obscured galaxies (bluDOGs) at $z \sim 2.5$ (Noboriguchi et al. 2023). They exhibit both composite rest-frame UV and optical SEDs, with excess blue emission suggestive of leaked or scattered AGN light, similar to our LRDs. However, we find that our sample is qualitatively different from this population, despite clear similarities in the UV and optical. While our sources show relative flat mid-IR SEDs, bluDOGs do exhibit strongly rising SEDs into the mid-infrared, characteristic of hot AGN-heated dust (Noboriguchi et al. 2019, 2022).

We note that while strong rest-frame optical emission lines driven by AGN can also impact the interpretation of high stellar mass (Endsley et al. 2023; Kocevski et al. 2023), our inclusion of at least four NIRCam medium bands plus the longer-wavelength MIRI data to anchor the SED beyond the wavelength range with the most contamination is a strong mitigator of this uncertainty.

Future spectroscopy of this sample (in particular to measure rest-frame optical Hα, Hβ, and [O III] equivalent widths and line profile shapes) could potentially reveal the origin of the rest-frame optical continuum and validate the photometric measurements. In addition to confirming the likely presence of an AGN accretion disk via the broad lines, Greene et al. (2023) use the relatively low Hα equivalent widths to argue that the continuum is not likely dominated by dust-obscured young stars. However, low equivalent widths could also be explained by older stars and low level star formation over the past 10 Myr (which is consistent with our SED-modeling results). Given that these sources typically have high attenuation ($A_V \sim 1$–3), deeper spectroscopy than was obtained with FRESCO is likely required to adequately measure both the broad- and narrow-line components (if they exist). High spectral resolution will also improve the differentiation between emission line broadening due to outflowing gas versus AGN.

6.2.2. Potentially Errant Modeling Assumptions

We note that we use mostly conservative assumptions in our modeling, including a flexible-slope attenuation curve that allows extra attenuation in the UV to avoid "hiding" stellar mass with a fixed flat slope model (noting that the assumed attenuation curve slope can impact the recovered mass by almost an order of magnitude; Lo Faro et al. 2017; Williams et al. 2019). Additionally, while nonparametric SFHs have been shown to raise stellar mass by 0.3 dex on average based on representative galaxies at lower redshifts (e.g., Leja et al.

2019), these objects would still remain systematically too high (unless the typical systematic offset is not representative for such extreme and red galaxies).

A number of works now report that the choice of prior on the SFH can significantly impact the ages and masses inferred by a nonparametric SFH (e.g., Leja et al. 2019; Lower et al. 2020; Ji & Giavalisco 2022; Tacchella et al. 2022b; Whitler et al. 2023). Therefore, we test whether our choice of continuity prior for the SFH has weighted against bursty SFH solutions, which could result in lower mass solutions by enabling us to explain the SEDs with a larger fraction of stars at younger stellar ages. We rerun our prospector modeling for these six high-mass sources instead using the Dirichlet prior (Leja et al. 2017), which allows for sudden and extreme changes in the SFR in adjacent time bins (and is a weaker prior on the inferred shape of the SFH compared to the continuity prior). We find that the differences in stellar mass measured with the burstier Dirichlet prior do not cause a systematic shift in mass of our high-mass sample, and further, are all consistent within the uncertainties of the stellar masses based on the continuity prior. We do find that the best SFH shapes do change with the Dirichlet solution and appear more stochastic (indicating that robust stellar ages will require spectroscopy). This typical difference to the SFR in the most recent 30 Myr is only $\sim$1 $M_\odot$, but we note that our most active source among the massive sample (ID 219000) sees a 30% decrease in its recent SFR with the Dirichlet prior. However, our stellar masses, and thus primary conclusions, do not rely heavily on our prior choice.

Importantly, while the stellar masses from the Dirichlet prior are still consistent within their uncertainties with those inferred using the continuity prior (typical difference is $<$0.1 dex) we note that the uncertainties in mass derived from the posteriors of each set of modeling do not marginalize over these assumptions. Unfortunately, this is also the case for a number of assumptions that have gone into our modeling, including IMF shape (see, e.g., Wang et al. 2023; Woodrum et al. 2023). Thus, the true uncertainty in stellar mass is larger than implied in Figure 9. We conclude that more advanced priors or an alternative IMF, among other assumptions, may be able to help lower the stellar masses and account for this tension. Otherwise, these targets are likely excellent test beds for studying modeling systematics, or the potential for more exotic explanations in the future with near-infrared spectroscopy.

7. Conclusions

We study a sample of optically faint sources at $z > 3$ that are below the detection limits of the deepest HST and ALMA surveys to date, and have previously been missed from the galaxy census at $3 < z < 8$. We find that these sources are relatively abundant within the JADES survey (66), and study a subset of those (29) for which deep multiwavelength MIRI data are also available. Our findings include the following.

1. The population of red optically faint galaxies are diverse in morphology (including both extremely extended sources as well as compact unresolved sources) and in SED shape, including sources resembling dust-obscured star-forming galaxies, poststarburst galaxies, and some objects exhibiting evidence of strong Balmer breaks despite being high redshift.
2. We find that stellar population modeling for sources using HST + NIRCam data alone can result in large

masses and SFRs. When MIRI + ALMA data are included, we find a median decrease of 0.6 dex in stellar mass and a median decrease of $10\times$ for sources sources where HST + NIRCam data alone infer $\log_{10}(M^*/M_\odot) > 10$ and SFR $> 100\ M_\odot$ yr^{-1}, respectively. Thus, caution should be exercised when interpreting the SEDs of very red sources from HST + NIRCam data alone.

3. Our sample includes $\sim$30% candidate AGN (selected as LRDs) and the fraction of LRDs is 100% among red galaxies above $z > 6.5$. Novel measurements with MIRI out to 25 μm for this population confidently rule out that their very red rest-frame optical continuum primarily originates as an obscured AGN continuum. Instead, evidence for a turnover in the SED between rest-frame 1–3 μm suggests we are seeing the 1.6μm stellar bump, and the red rest-frame optical continuum is stellar in origin. We cannot rule out the presence of an AGN that becomes dominant in the rest-frame mid-infrared SED, which requires longer-wavelength data.

4. Noting that AGN are not likely dominating the rest-frame optical emission, we use our stellar population modeling to assess the contribution to the galaxy census of this previously hidden population of galaxies. We estimate lower limits to the cosmic SFRD and find that galaxies at $\log_{10}(L_{\rm IR}/L_\odot) < 12$ and $4 < z < 6$ may contribute $5\times$ more to the obscured fraction of the SFR than previously estimated based on extrapolation of the infrared luminosity function, which could effectively double the obscured SFRD in this redshift range.

5. We also assess the stellar masses we measure in the context of the limited area we probe in our survey, finding that five sources between $z \sim 5.5 - 8$ have very high mass for our small survey area, despite the revision to lower stellar mass provided by the MIRI data. These sources have strong Balmer breaks and SED turnovers consistent with the stellar bump in the rest-frame near-infrared, well described by moderately old and dusty SEDs (age ~ 500 Myr, $A_V \sim 1$). We discuss plausible reasons for the overestimated stellar masses, based on existing assumptions of the stellar population and AGN modeling, motivating future work to characterize the physical properties of very red high-redshift galaxies.

Acknowledgments

Appendix

In this appendix we present Figure 11 which presents the NIRCam and MIRI image cutouts for each source within the SMILES footprint (our primary sample), as well as its observed SED and its `prospector` modeling results. In Figure 12, we show the FRESCO or JADES/NIRSpec data, line identifications, and spectroscopic redshift for all objects with available spectroscopy.
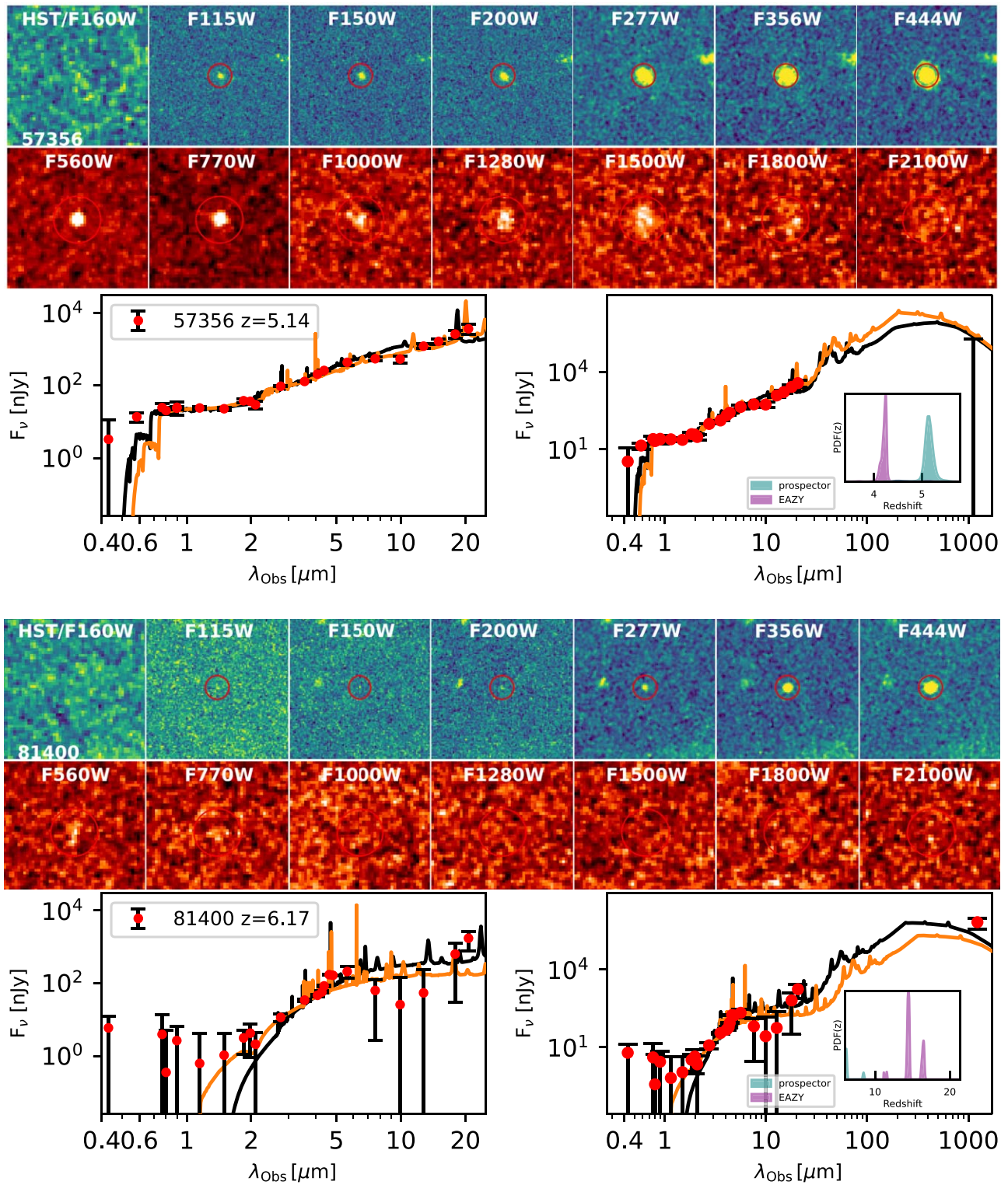
Figure 11. Top panels: cutouts for sources that lie inside our MIRI footprint (NIRCam cutouts in blue green, MIRI cutouts in red). The bottom panel shows the photometry (points) and best SED model fit to only HST + NIRCam data (black) and best SED model fit to HST + NIRCam + MIRI + ALMA data (orange). Left is zoomed in on the rest-frame optical and near-infrared SEDs. The subpanel shows the PDF(z) from both our preliminary EAZY modeling (purple) and from our full prospector modeling including the MIRI and ALMA data (teal), unless a spectroscopic redshift was used (black dotted line). Both distributions are scaled to a peak of one for easy comparison. The photometry for sources with spectroscopic redshifts is shown in blue (for spectroscopically confirmed objects). Sources which meet the LRD AGN selection are flagged. The brown dwarf (BD) candidate based on colors and proper motion is also flagged.
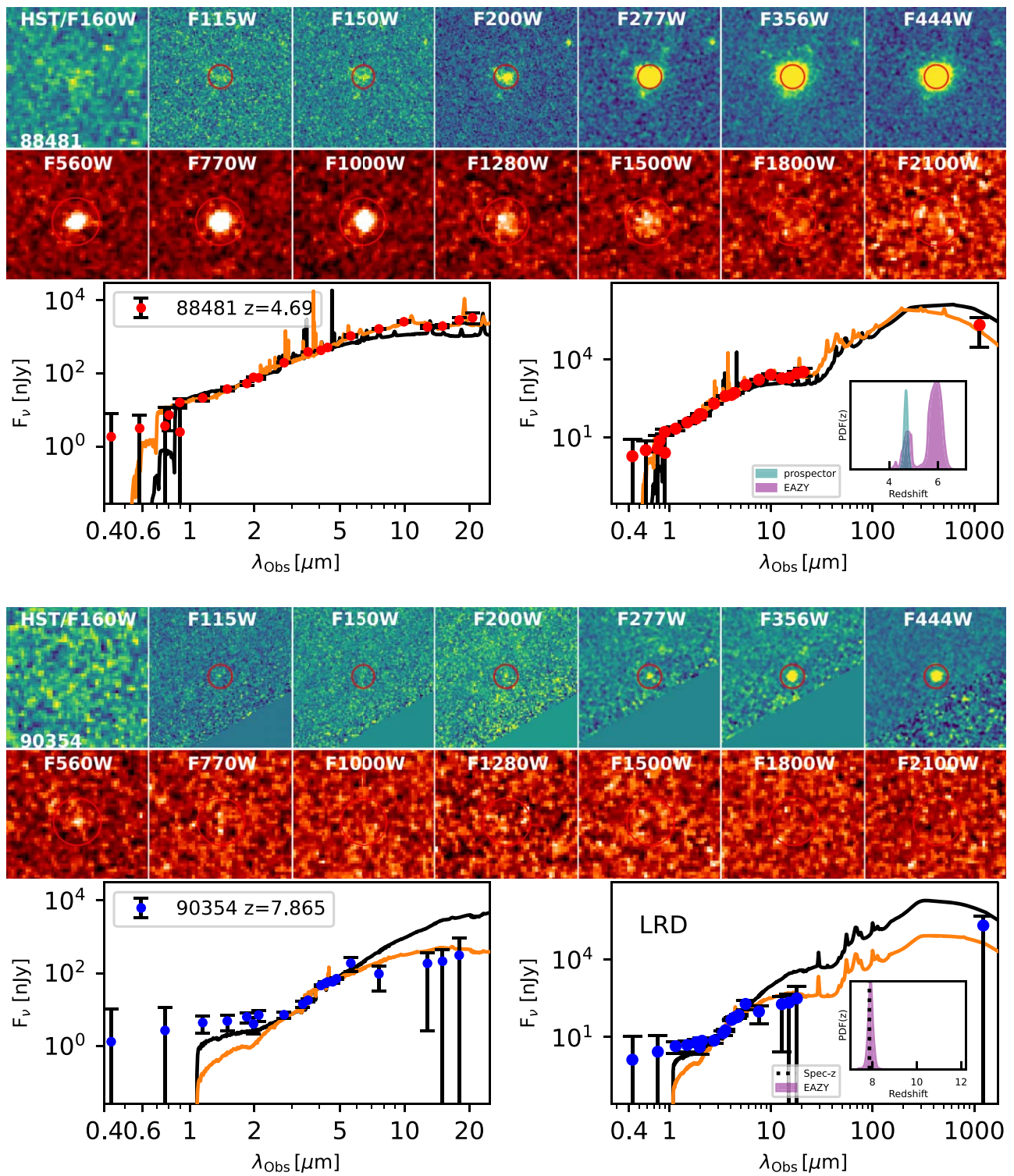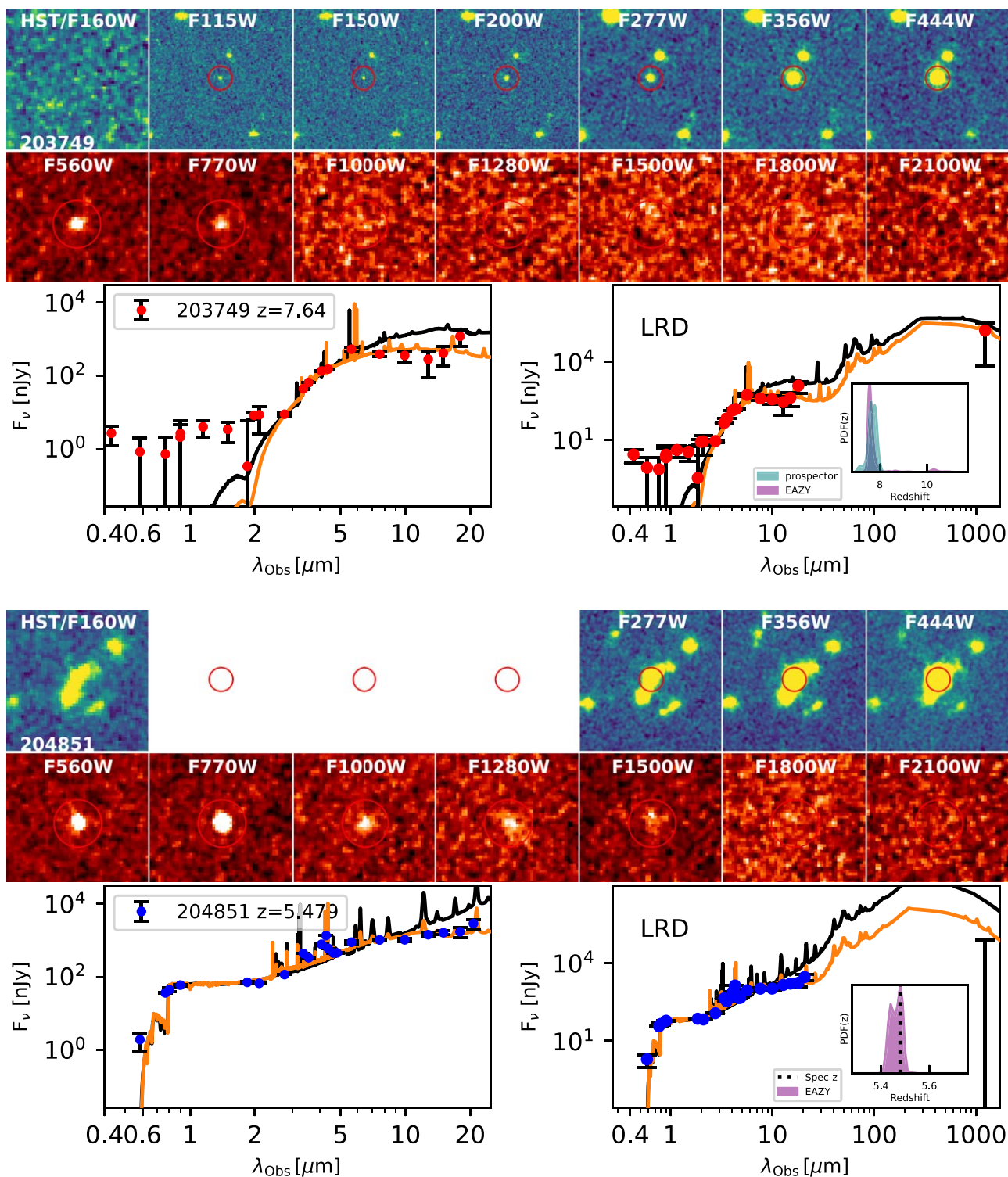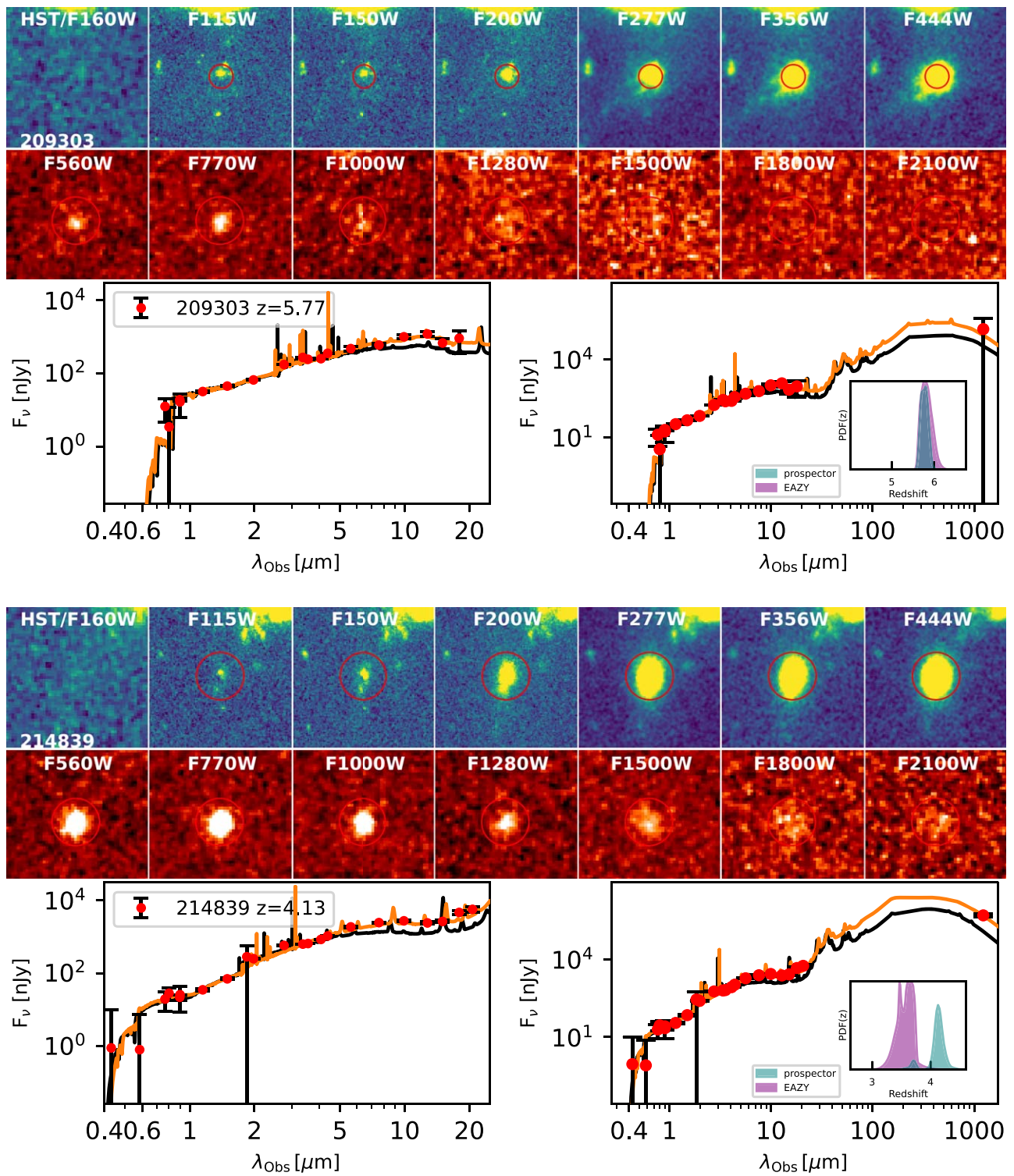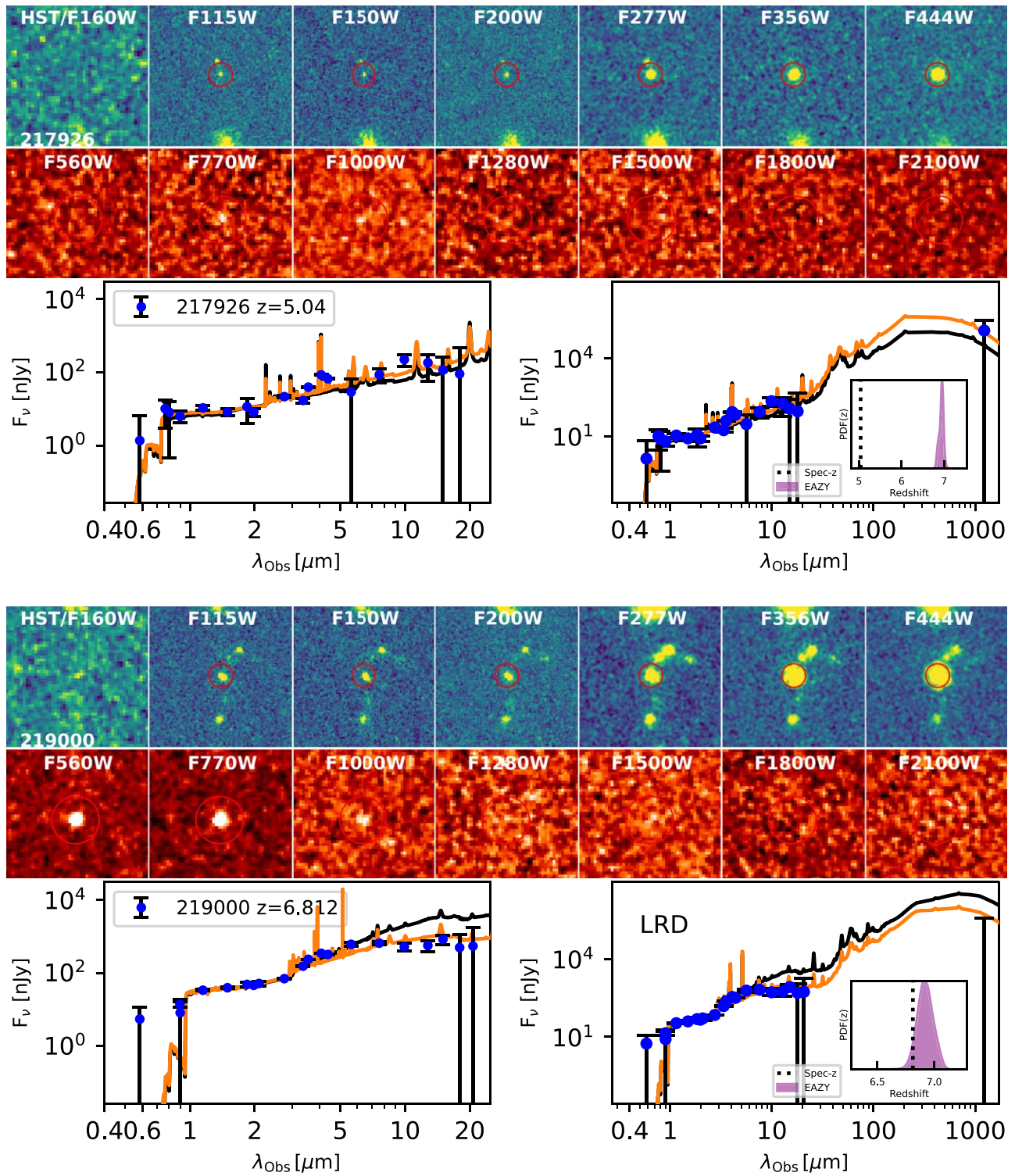
Figure 11. (Continued.)
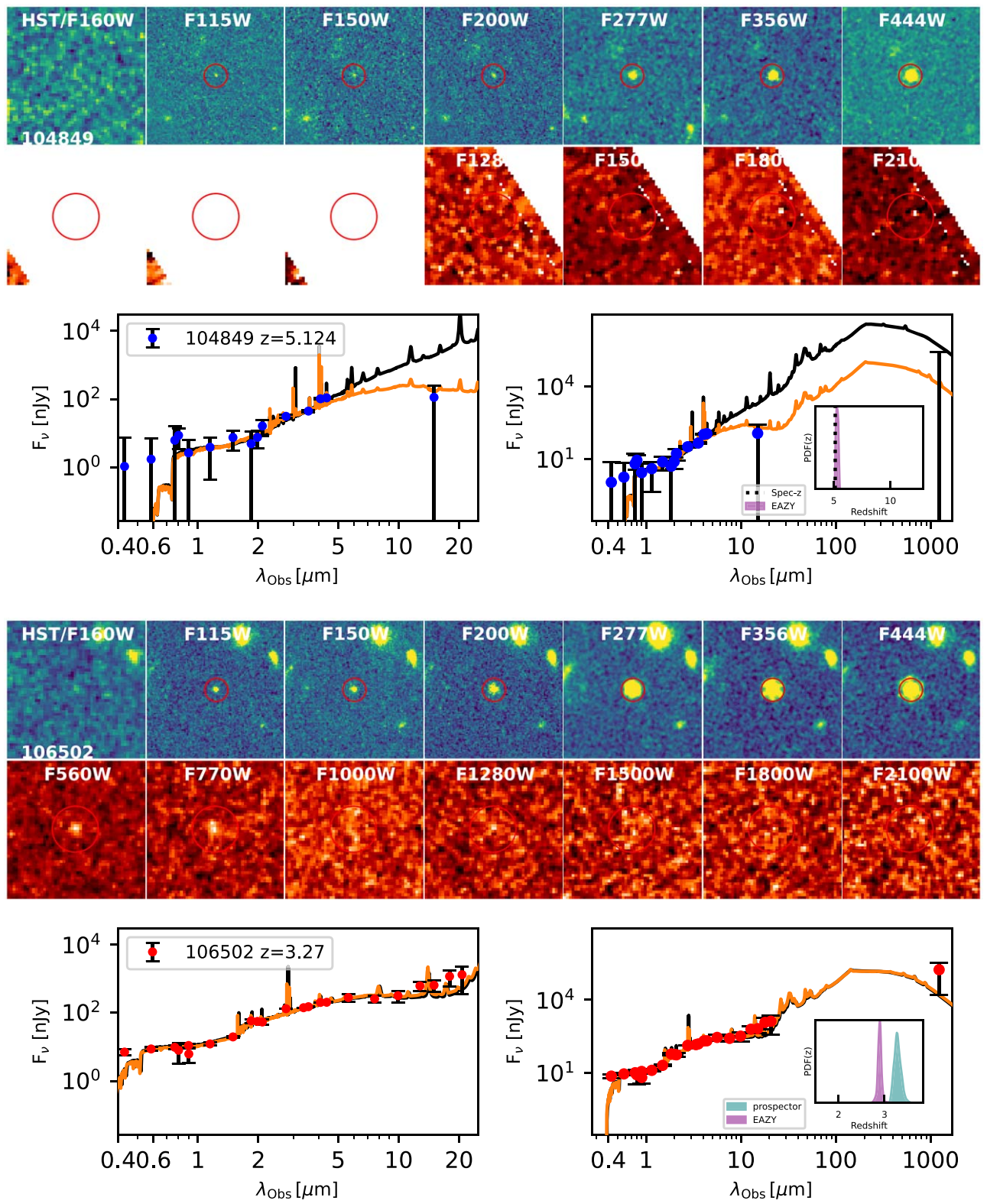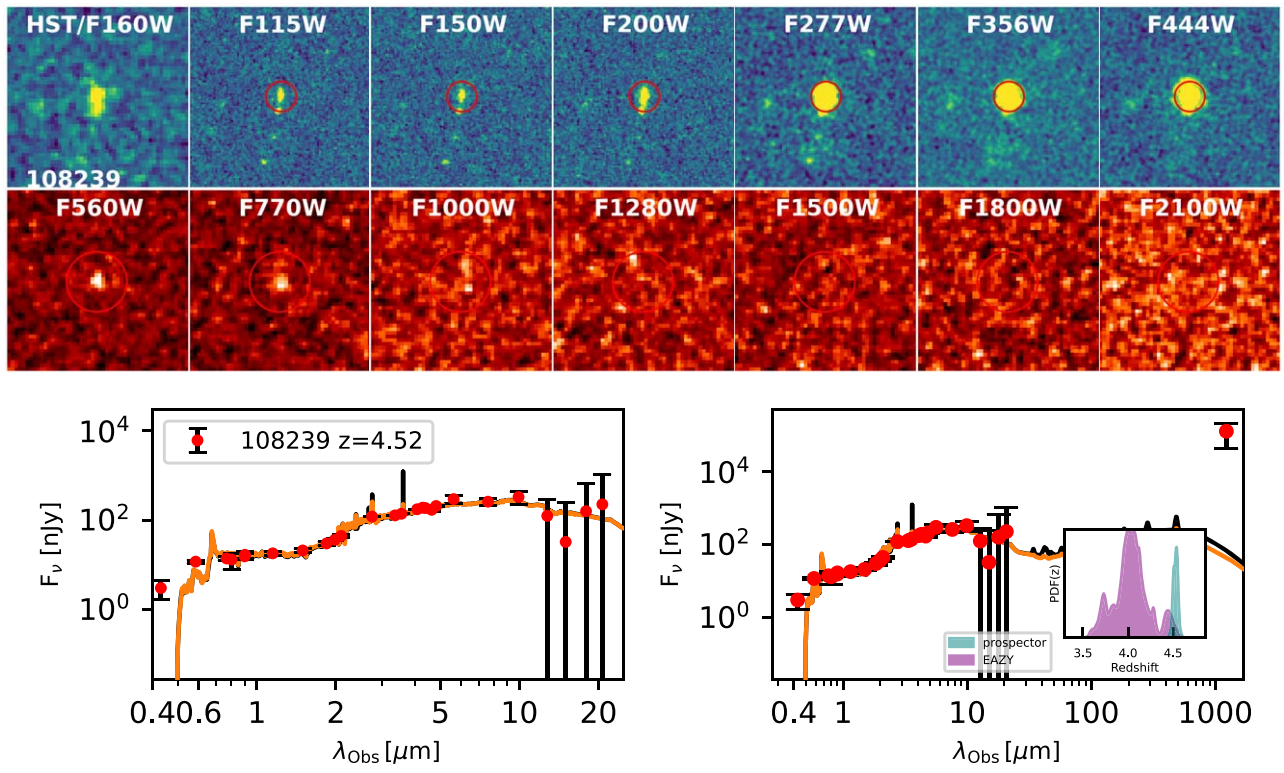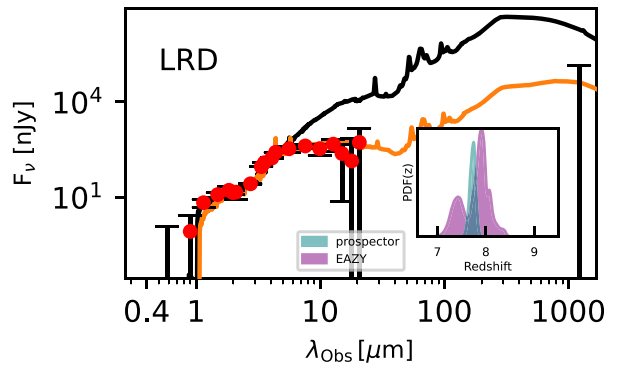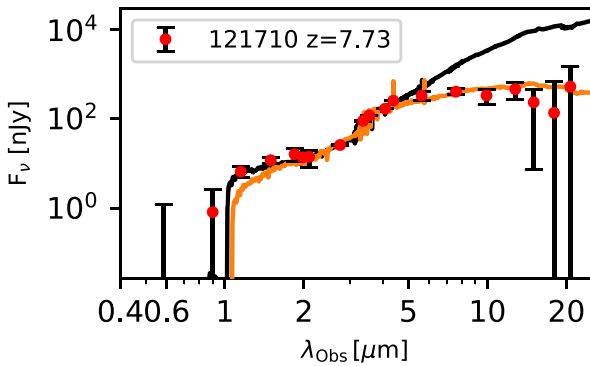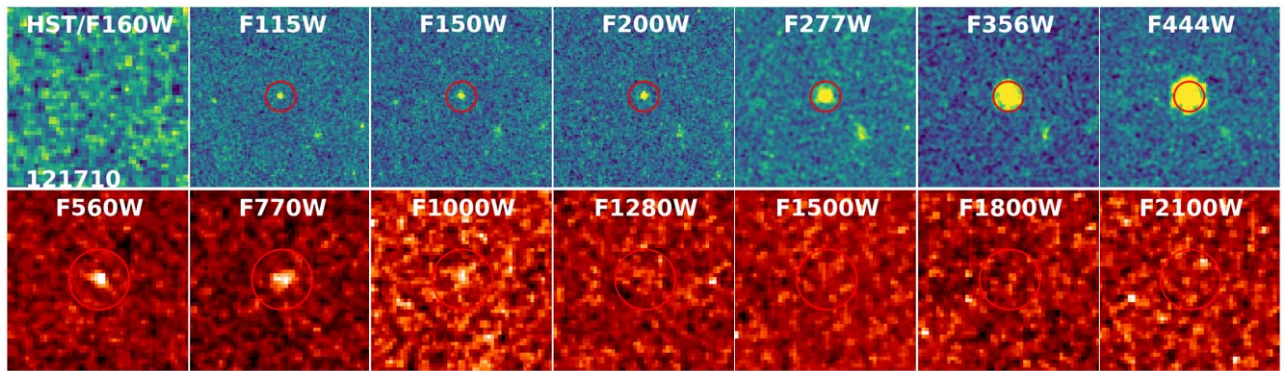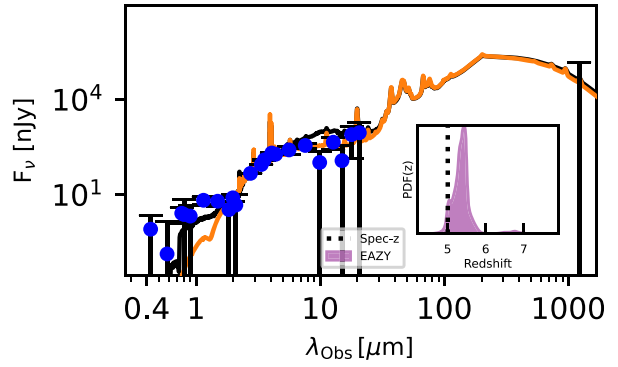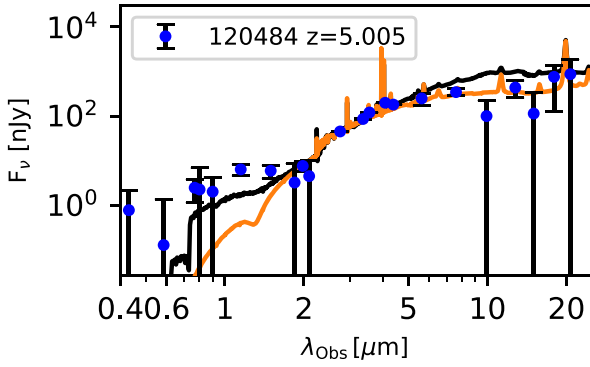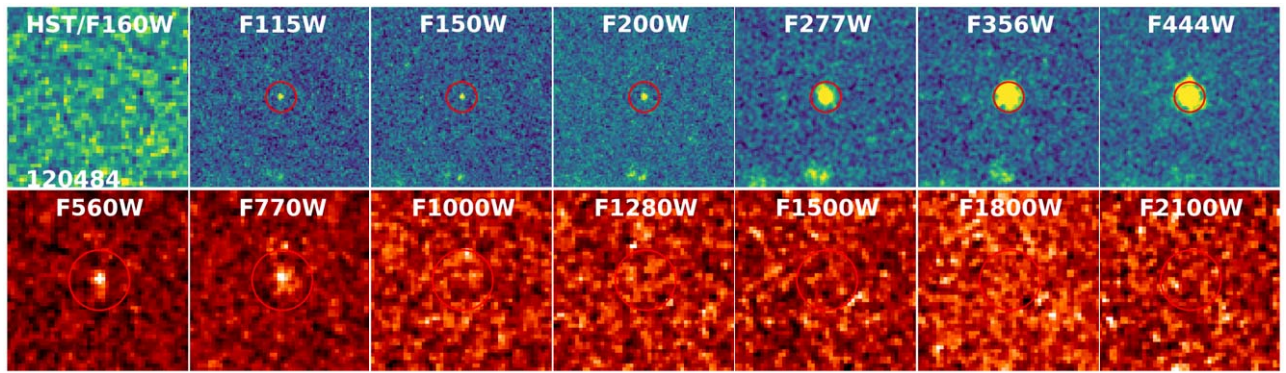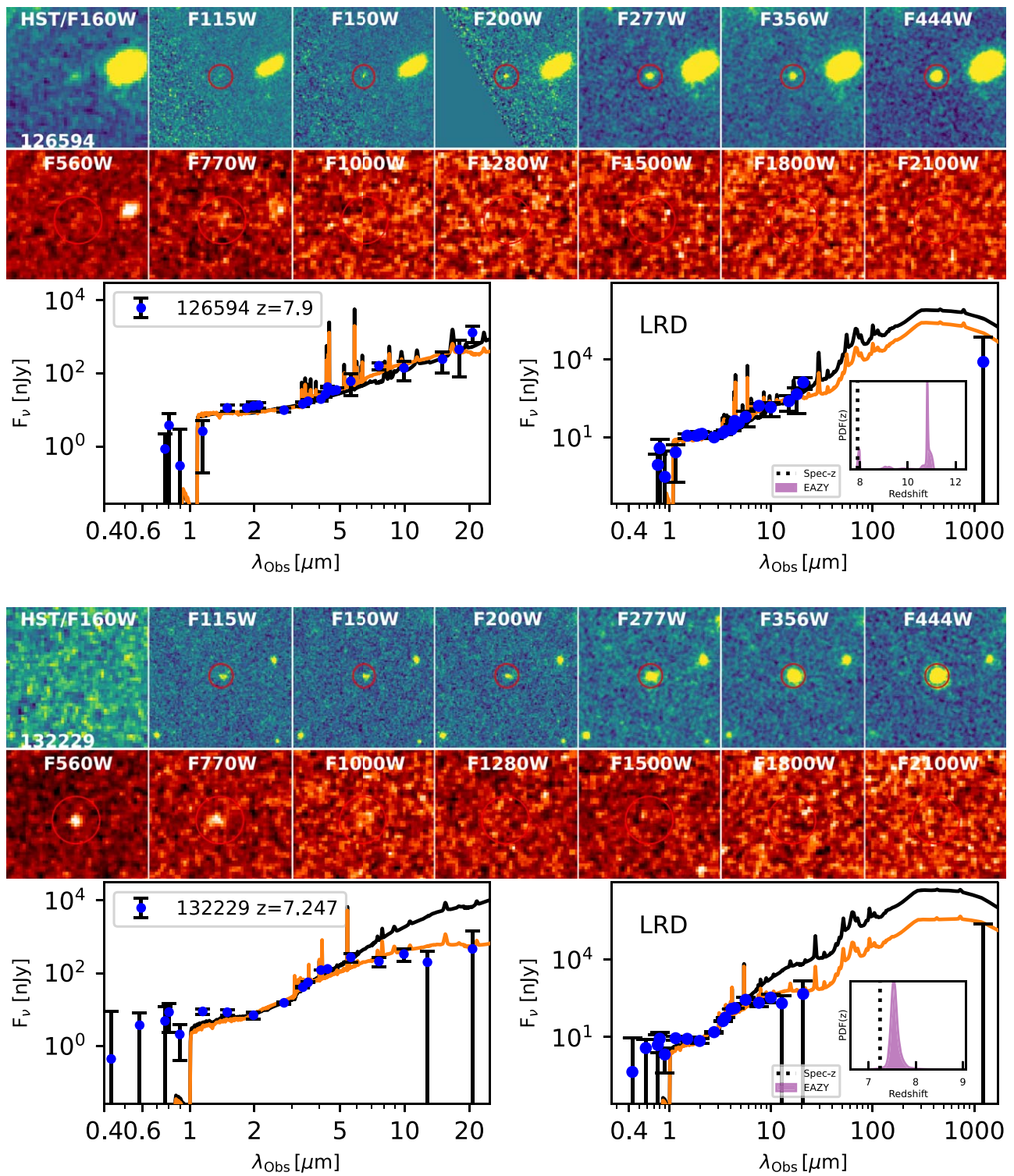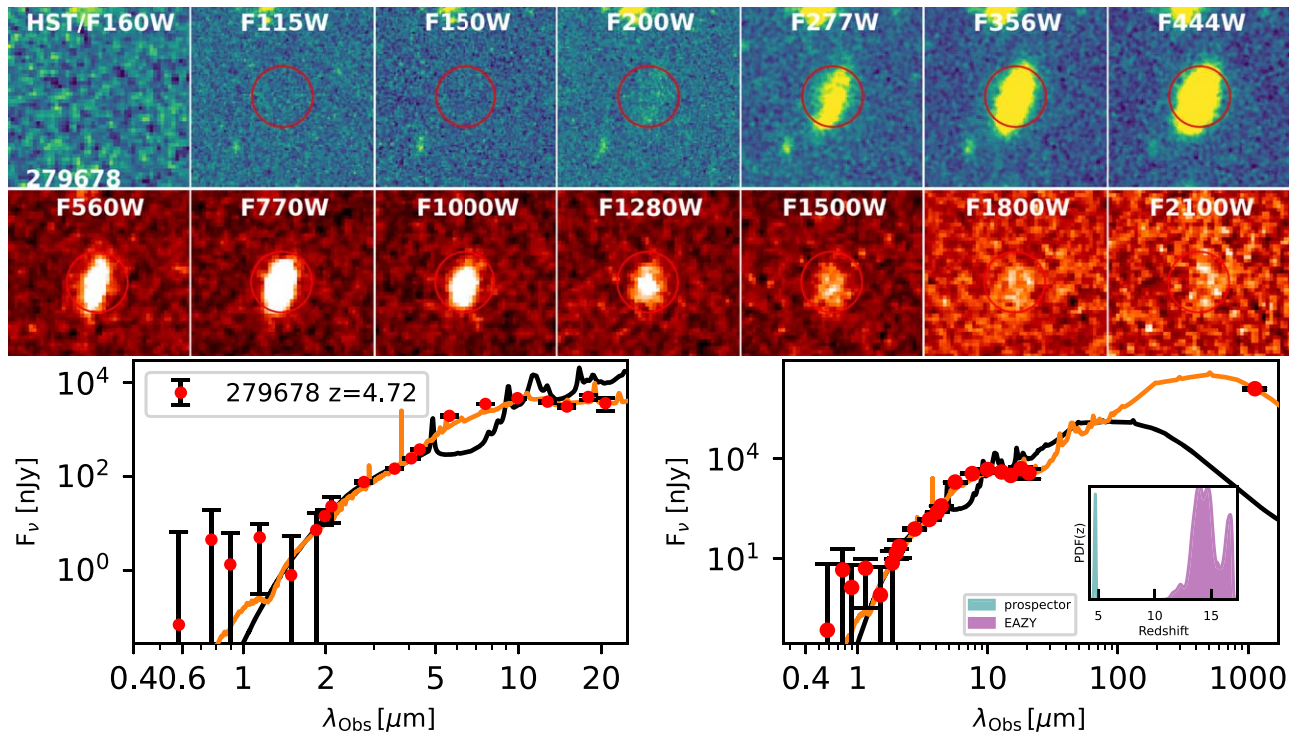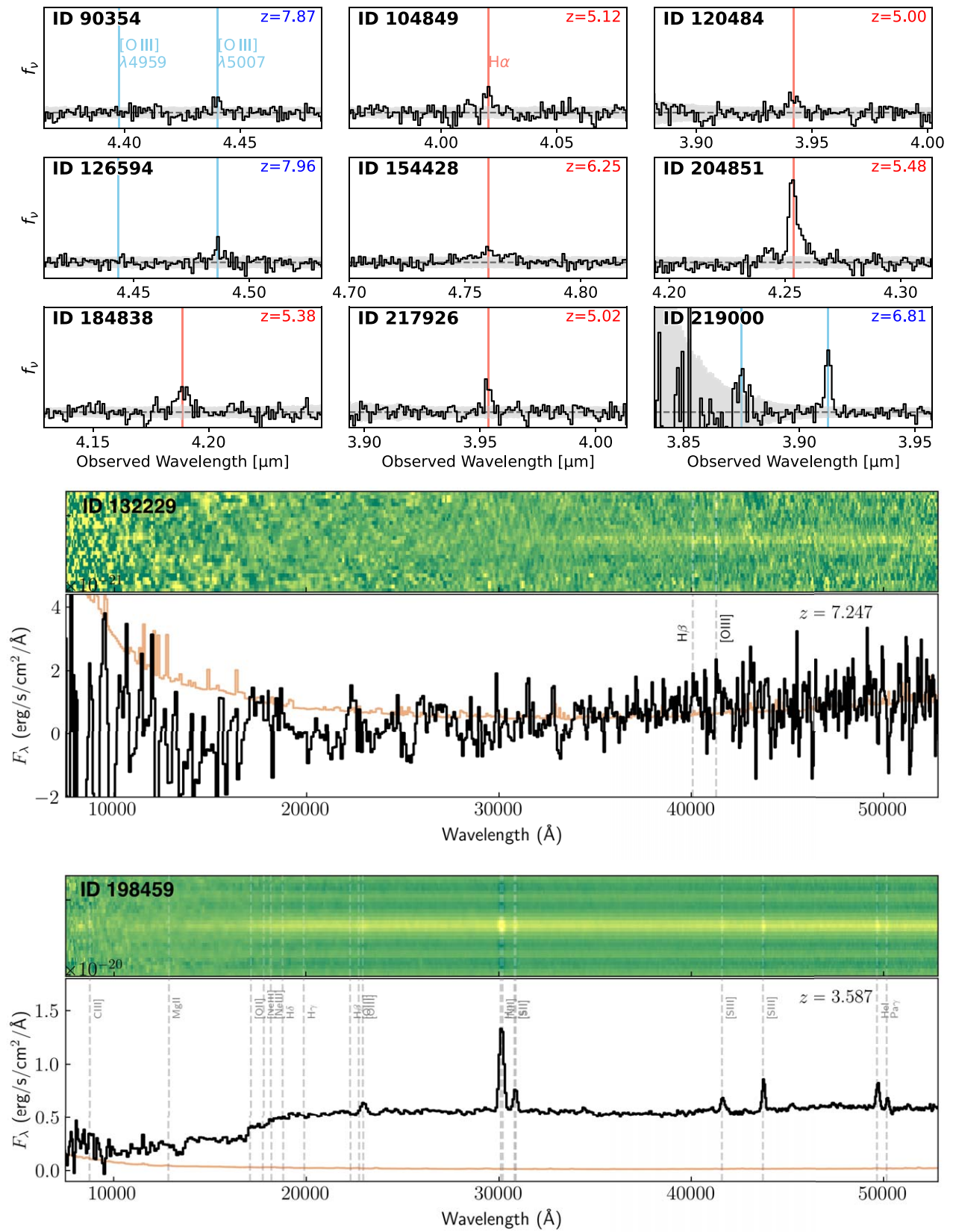
Figure 11. (Continued.)

Figure 11. (Continued.)

Figure 11. (Continued.)

Figure 11. (Continued.)
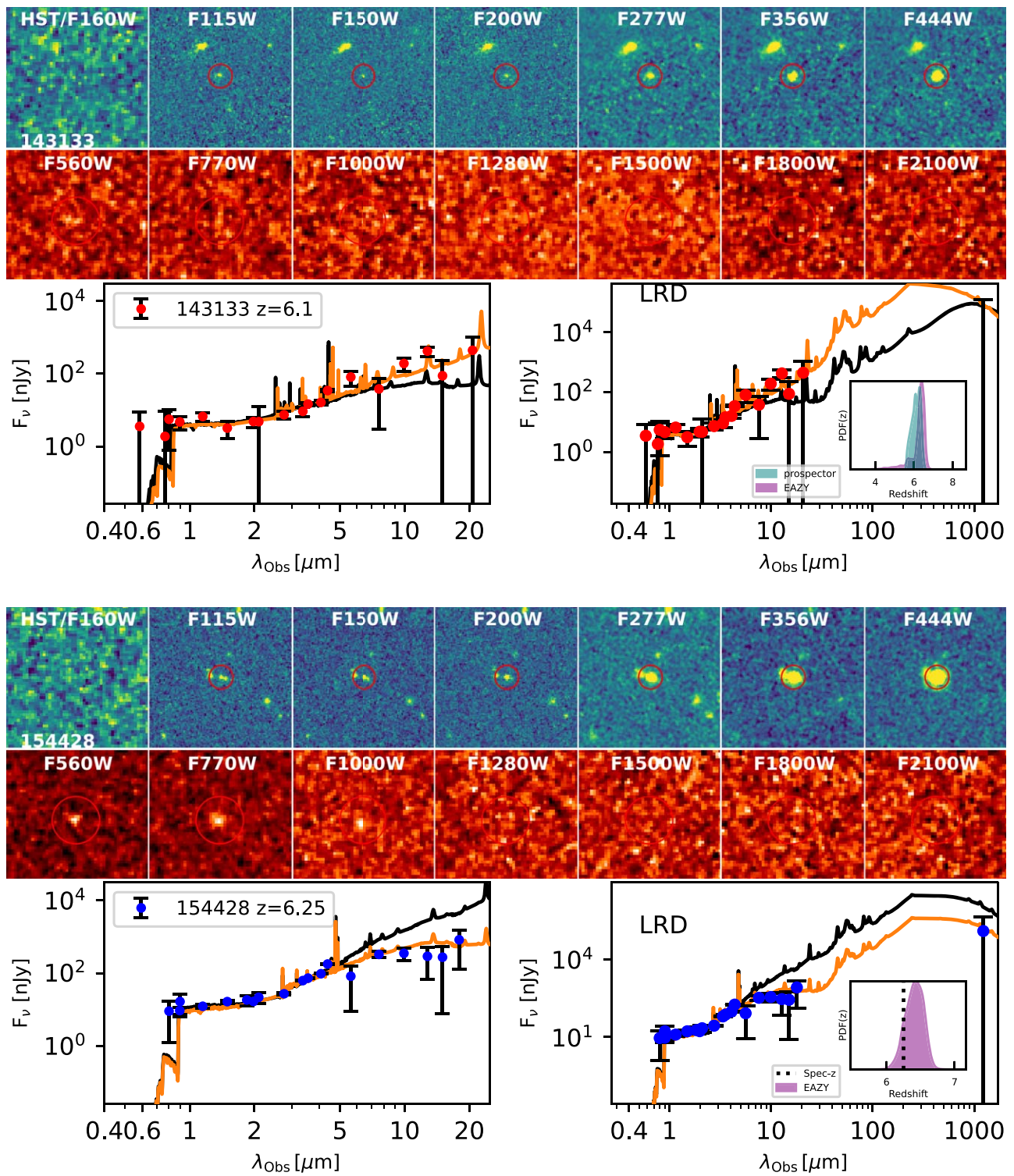
Figure 11. (Continued.)
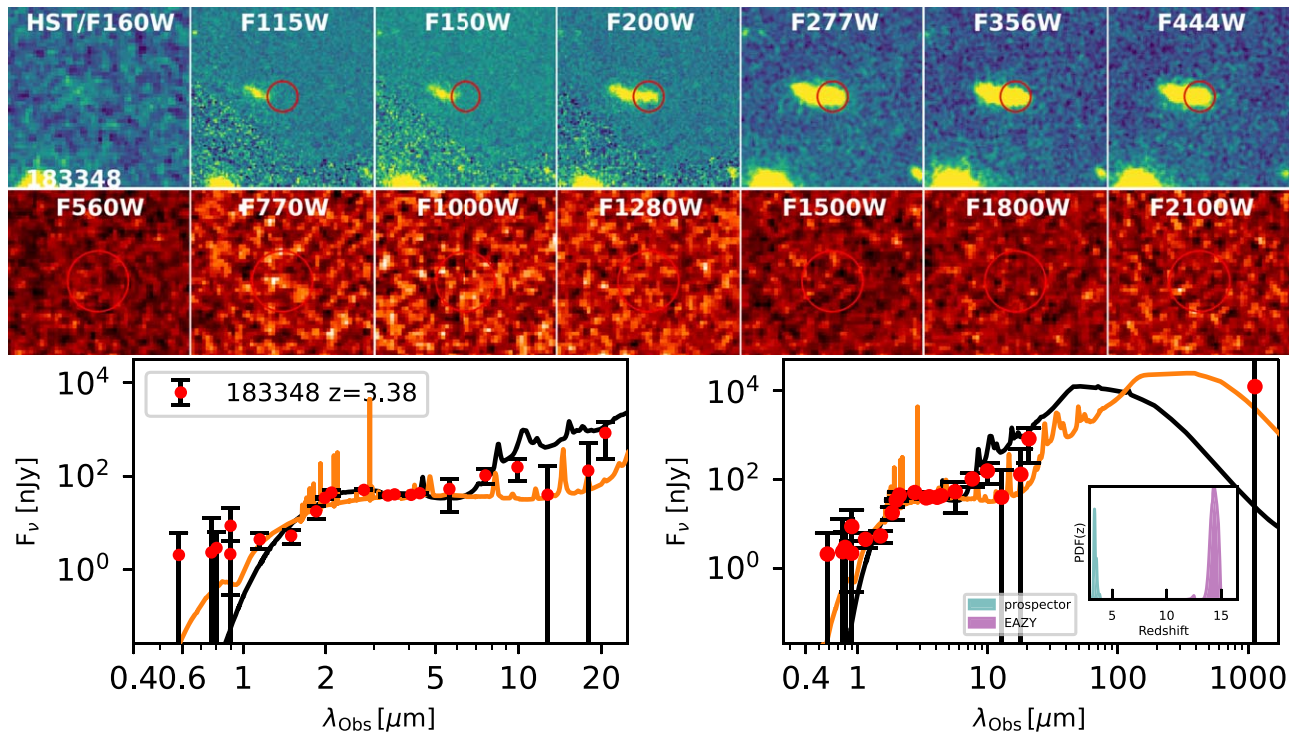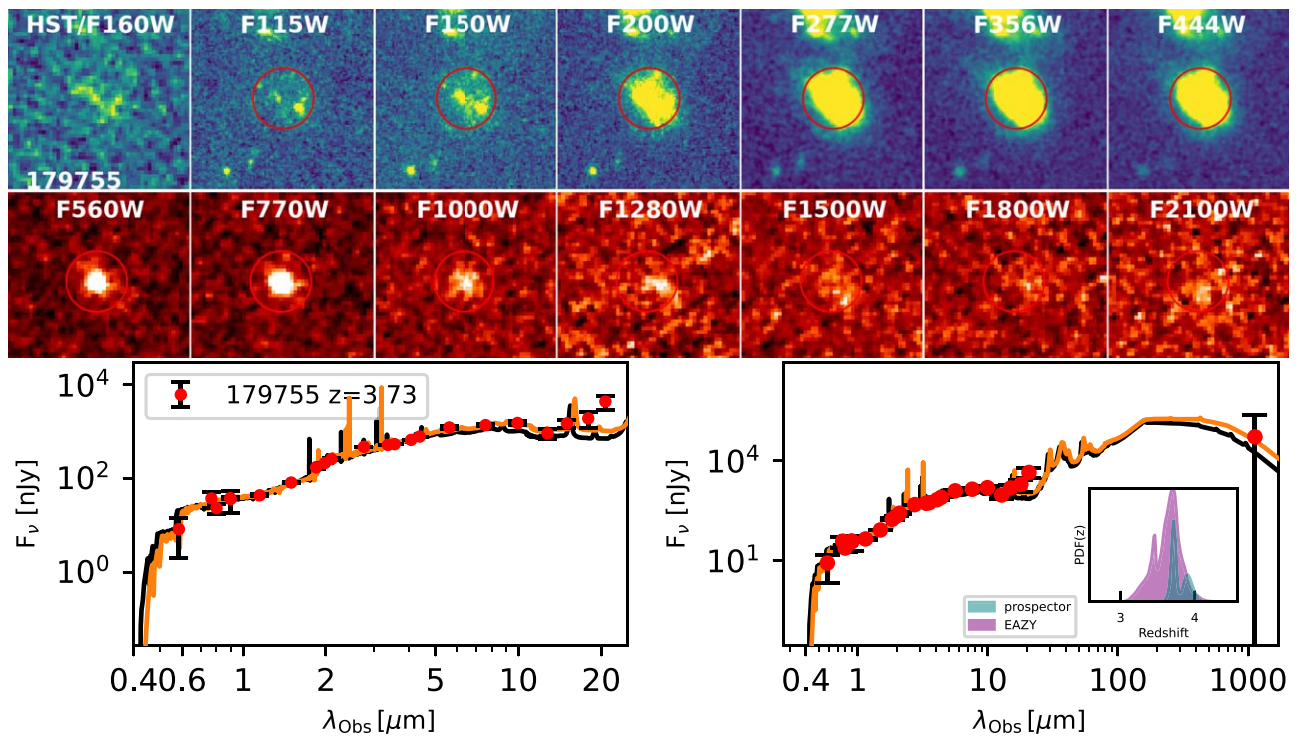
Figure 11. (Continued.)
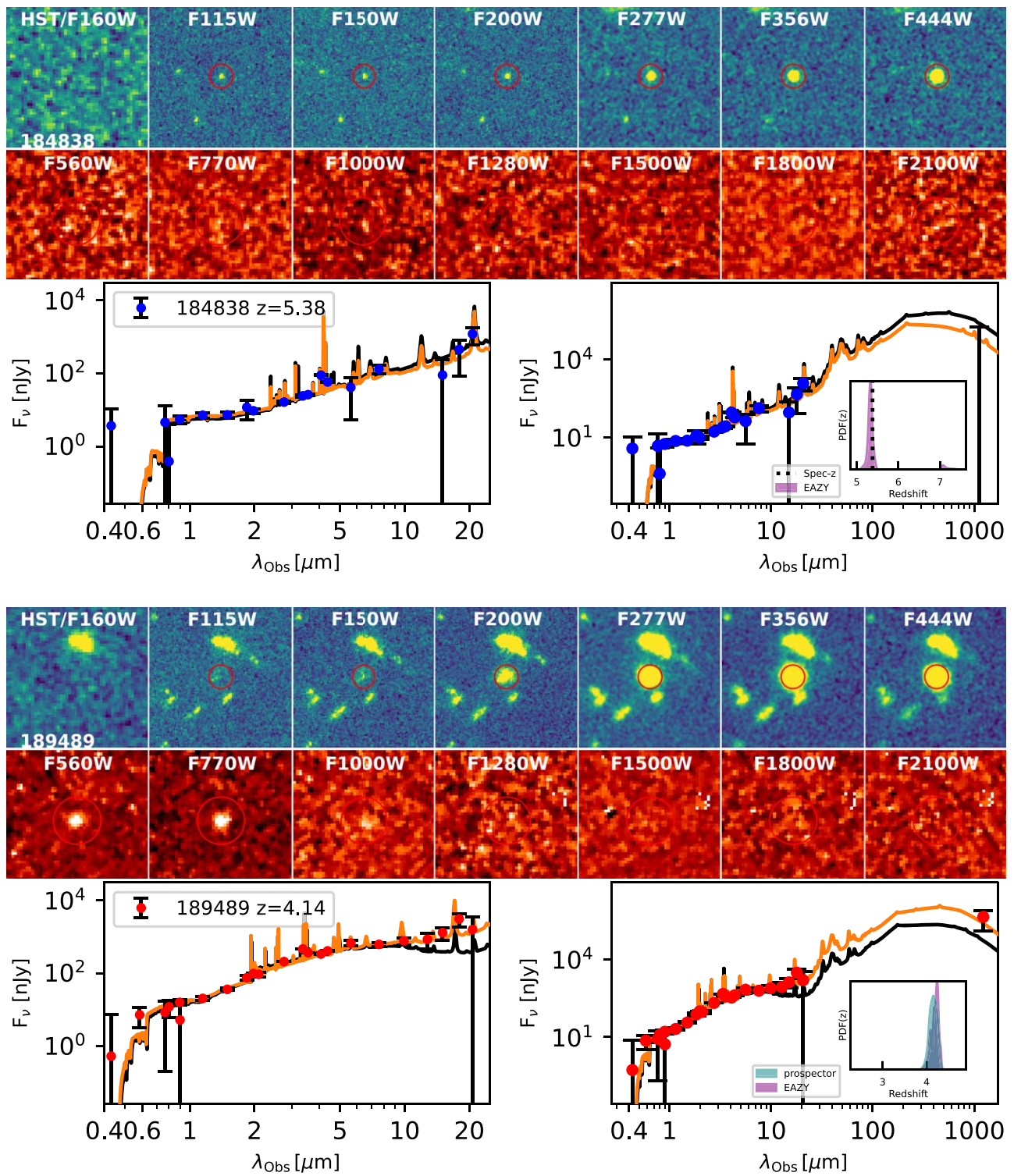
Figure 11. (Continued.)
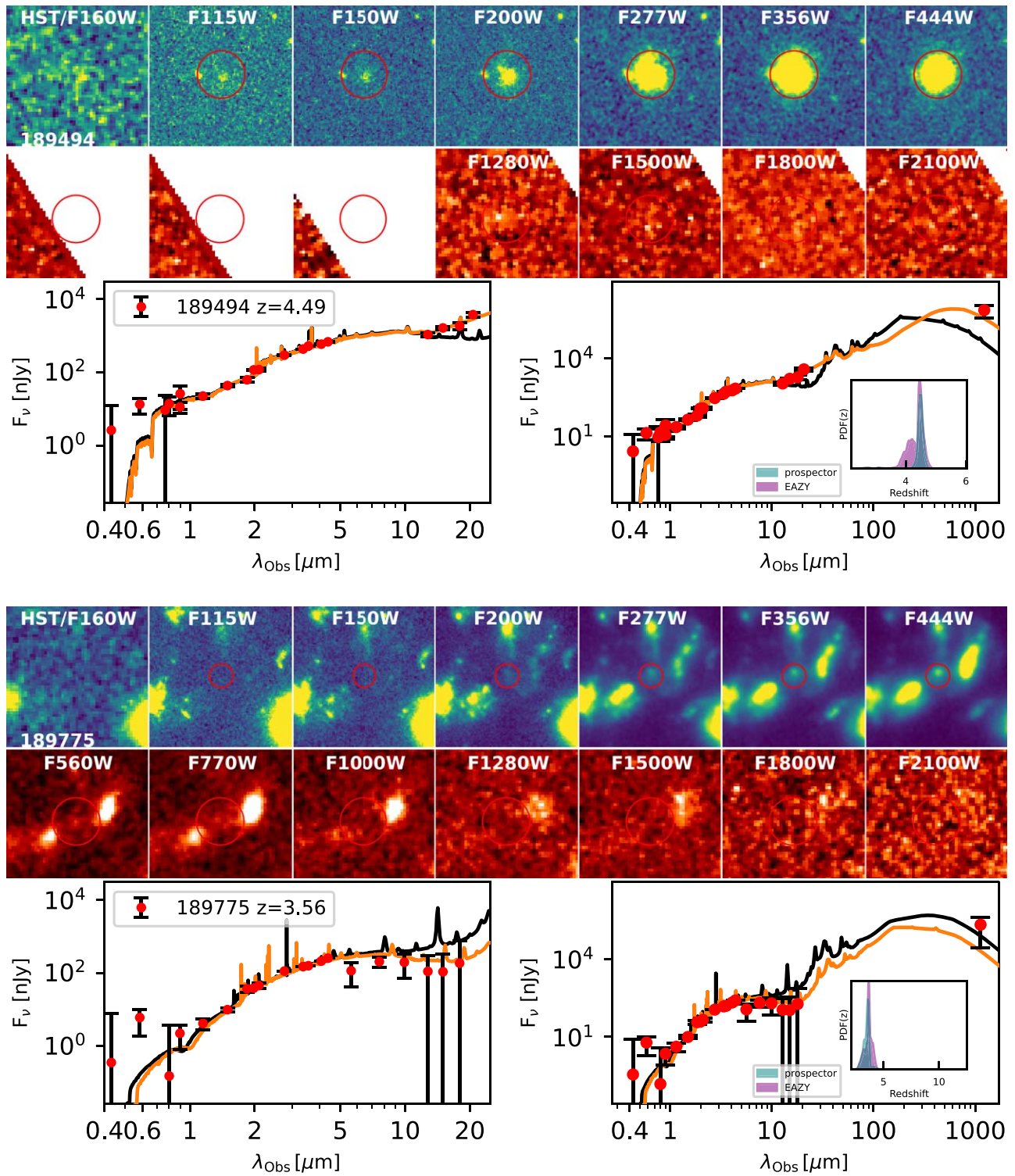
Figure 11. (Continued.)
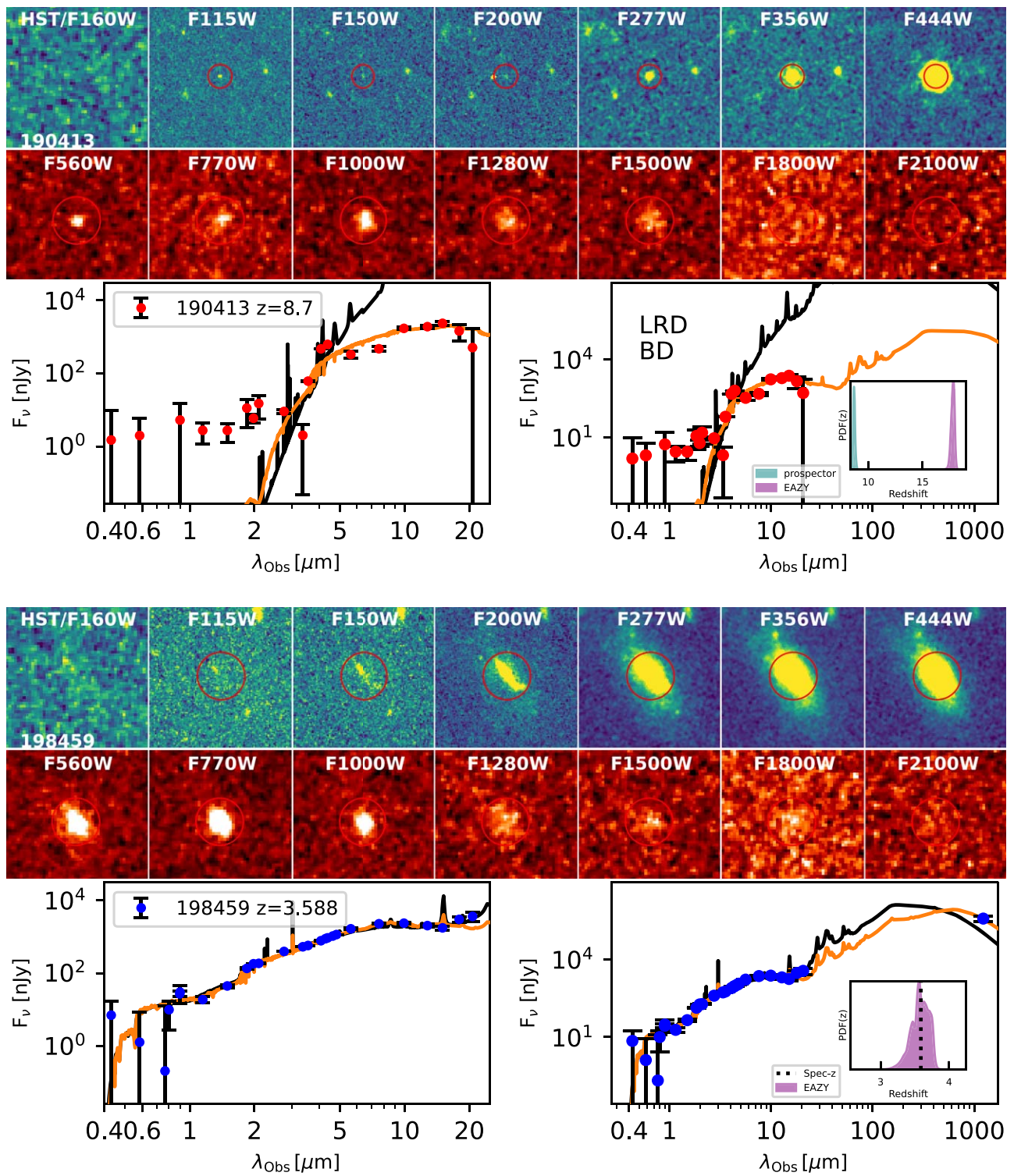
Figure 11. (Continued.)
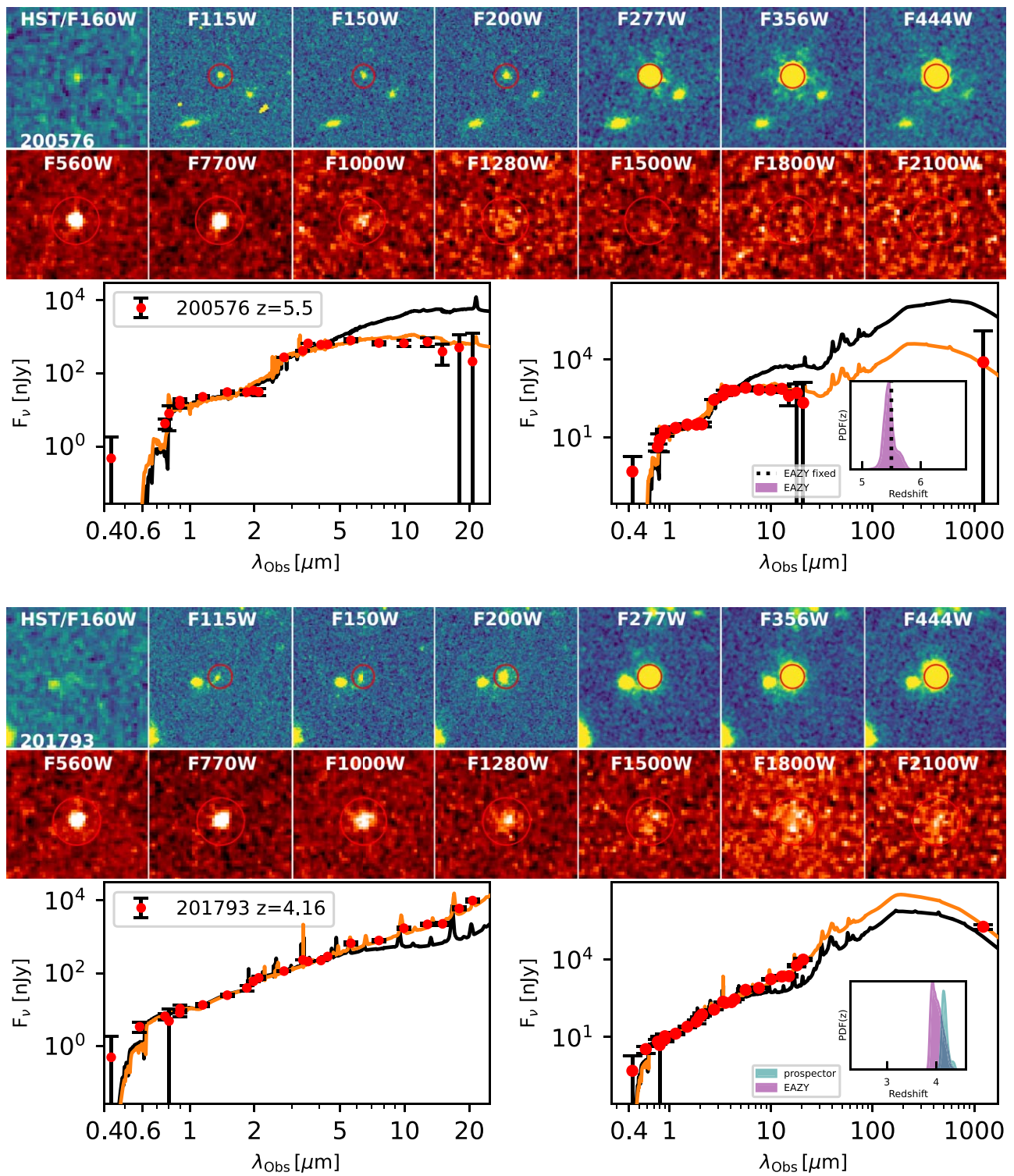
Figure 11. (Continued.)

Figure 11. (Continued.)

Figure 11. (Continued.)

Figure 11. (Continued.)

Figure 11. (Continued.)

Figure 12. Spectroscopic data used in this work from FRESCO (top grid) and JADES/NIRSpec (bottom two panels).

ORCID iDs

Christina C. Williams ● https://orcid.org/0000-0003-2919-7495

Stacey Alberts ● https://orcid.org/0000-0002-8909-8782

Zhiyuan Ji ● https://orcid.org/0000-0001-7673-2257

Kevin N. Hainline ● https://orcid.org/0000-0003-4565-8239

Jianwei Lyu ● https://orcid.org/0000-0002-6221-1829

George Rieke ● https://orcid.org/0000-0003-2303-6519

Ryan Endsley ● https://orcid.org/0000-0003-4564-2771

Katherine A. Suess ● https://orcid.org/0000-0002-1714-1905

Fengwu Sun ● https://orcid.org/0000-0002-4622-6617

Benjamin D. Johnson ● https://orcid.org/0000-0002-9280-7594

Michael Florian ● https://orcid.org/0000-0001-5097-6755

Irene Shivaei ● https://orcid.org/0000-0003-4702-7561

Wiphu Rujopakarn ● https://orcid.org/0000-0002-0303-499X

William M. Baker ● https://orcid.org/0000-0003-0215-1104

Rachana Bhatawdekar ● https://orcid.org/0000-0003-0883-2226

Kristan Boyett ● https://orcid.org/0000-0003-4109-304X

Andrew J. Bunker ● https://orcid.org/0000-0002-8651-9879

Alex J. Cameron ● https://orcid.org/0000-0002-0450-7306

Stefano Carniani ● https://orcid.org/0000-0002-6719-380X

Stephane Charlot ● https://orcid.org/0000-0003-3458-2275

Emma Curtis-Lake ● https://orcid.org/0000-0002-9551-0534

Christa DeCoursey ● https://orcid.org/0000-0002-4781-9078

Anna de Graaff ● https://orcid.org/0000-0002-2380-9801

Eiichi Egami ● https://orcid.org/0000-0003-1344-9475

Daniel J. Eisenstein ● https://orcid.org/0000-0002-2929-3121

Justus L. Gibson ● https://orcid.org/0000-0003-1903-9813

Ryan Hausen ● https://orcid.org/0000-0002-8543-761X

Jakob M. Helton ● https://orcid.org/0000-0003-4337-6211

Roberto Maiolino ● https://orcid.org/0000-0002-4985-3819

Michael V. Maseda ● https://orcid.org/0000-0003-0695-4414

Erica J. Nelson ● https://orcid.org/0000-0002-7524-374X

Pablo G. Pérez-González ● https://orcid.org/0000-0003-4528-5639

Marcia J. Rieke ● https://orcid.org/0000-0002-7893-6170

Brant E. Robertson ● https://orcid.org/0000-0002-4271-0364

Aayush Saxena ● https://orcid.org/0000-0001-5333-9970

Sandro Tacchella ● https://orcid.org/0000-0002-8224-4505

Christopher N. A. Willmer ● https://orcid.org/0000-0001-9262-9997

Chris J. Willott ● https://orcid.org/0000-0002-4201-7367

References

Akins, H. B., Casey, C. M., Allen, N., et al. 2023, ApJ, 956, 61
Alberts, S., Lyu, J., Shivaei, I., et al. 2024, arXiv:2405.15972
Alberts, S., Williams, C. C., Helton, J. M., et al. 2023, arXiv:2312.12207
Alcalde Pampliega, B., Pérez-González, P. G., Barro, G., et al. 2019, ApJ, 876, 135
Alexander, D. M., & Hickox, R. C. 2012, NewAR, 56, 93
Algera, H. S. B., Inami, H., Oesch, P. A., et al. 2023, MNRAS, 518, 6142
Álvarez-Márquez, J., Crespo Gómez, A., Colina, L., et al. 2023, A&A, 671, A105
Astropy Collaboration, Price-Whelan, A. M., Lim, P. L., et al. 2022, ApJ, 935, 167
Astropy Collaboration, Price-Whelan, A. M., Sipőcz, B. M., et al. 2018, AJ, 156, 123
Astropy Collaboration, Robitaille, T. P., Tollerud, E. J., et al. 2013, A&A, 558, A33
Bakx, T. J. L. C., Tamura, Y., Hashimoto, T., et al. 2020, MNRAS, 493, 4294
Barger, A. J., & Cowie, L. L. 2023, ApJ, 956, 95
Barro, G., Perez-Gonzalez, P. G., Kocevski, D. D., et al. 2024, ApJ, 963, 182
Barrufet, L., Oesch, P. A., Bouwens, R., et al. 2023a, MNRAS, 522, 3926

Barrufet, L., Oesch, P. A., Weibel, A., et al. 2023b, MNRAS, 522, 449
Beckwith, S. V. W., Stiavelli, M., Koekemoer, A. M., et al. 2006, AJ, 132, 1729
Behrens, C., Pallottini, A., Ferrara, A., Gallerani, S., & Vallini, L. 2018, MNRAS, 477, 552
Behroozi, P. S., Wechsler, R. H., & Conroy, C. 2013, ApJ, 770, 57
Béthermin, M., Daddi, E., Magdis, G., et al. 2015, A&A, 573, A113
Betti, S. K., Pope, A., Scoville, N., et al. 2019, ApJ, 874, 53
Bisigello, L., Caputi, K. I., Colina, L., et al. 2019, ApJS, 243, 27
Boquien, M., Burgarella, D., Roehlly, Y., et al. 2019, A&A, 622, A103
Boylan-Kolchin, M. 2023, NatAs, 7, 731
Bradley, L., Sipőcz, B., Robitaille, T., et al. 2022, astropy/photutils: v1.5.0, Zenodo, doi:10.5281/zenodo.6825092
Brammer, G. B., van Dokkum, P. G., & Coppi, P. 2008, ApJ, 686, 1503
Brisbin, D., Miettinen, O., Aravena, M., et al. 2017, A&A, 608, A15
Bunker, A. J., Cameron, A. J., Curtis-Lake, E., et al. 2023, arXiv:2306.02467
Burgasser, A. J., Bezanson, R., Labbe, I., et al. 2024, ApJ, 962, 177
Bushouse, H., Eisenhamer, J., Dencheva, N., et al. 2023, JWST Calibration Pipeline, v1.10.0, Zenodo, doi:10.5281/zenodo.7795697
Byler, N., Dalcanton, J. J., Conroy, C., & Johnson, B. D. 2017, ApJ, 840, 44
Calzetti, D., Armus, L., Bohlin, R. C., et al. 2000, ApJ, 533, 682
Caputi, K. I., Dunlop, J. S., McLure, R. J., et al. 2012, ApJL, 750, L20
Carnall, A. C., McLure, R. J., Dunlop, J. S., et al. 2023, Natur, 619, 716
Casey, C. M., Narayanan, D., & Cooray, A. 2014, PhR, 541, 45
Casey, C. M., Zavala, J. A., Manning, S. M., et al. 2021, ApJ, 923, 215
Charlot, S., & Fall, M. 2000, ApJ, 539, 718
Choi, J., Dotter, A., Conroy, C., et al. 2016, ApJ, 823, 102
Cochrane, R. K., Anglés-Alcázar, D., Cullen, F., & Hayward, C. C. 2024, ApJ, 961, 37
Conroy, C., Gunn, J. E., & White, M. 2009, ApJ, 699, 486
Cooper, O. R., Casey, C. M., Zavala, J. A., et al. 2022, ApJ, 930, 32
da Cunha, E., Groves, B., Walter, F., et al. 2013, ApJ, 766, 13
Danielson, A. L. R., Swinbank, A. M., Smail, I., et al. 2017, ApJ, 840, 78
De Rossi, M. E., Rieke, G. H., Shivaei, I., Bromm, V., & Lyu, J. 2018, ApJ, 869, 4
Desprez, G., Martis, N. S., Asada, Y., et al. 2024, MNRAS, 530, 2935
Dey, A., Graham, J. R., Ivison, R. J., et al. 1999, ApJ, 519, 610
Dotter, A. 2016, ApJS, 222, 8
Draine, B. T., Aniano, G., Krause, O., et al. 2014, ApJ, 780, 172
Draine, B. T., & Li, A. 2007, ApJ, 657, 810
Dudzevičiūtė, U., Smail, I., Swinbank, A. M., et al. 2020, MNRAS, 494, 3828
Dudzevičiūtė, U., Smail, I., Swinbank, A. M., et al. 2021, MNRAS, 500, 942
Dunlop, J. S., McLure, R. J., Biggs, A. D., et al. 2017, MNRAS, 466, 861
Dunlop, J. S., McLure, R. J., Yamada, T., et al. 2004, MNRAS, 350, 769
Eisenstein, D. J., Johnson, B. D., Robertson, B., et al. 2023a, arXiv:2310.12340
Eisenstein, D. J., Willott, C., Alberts, S., et al. 2023b, arXiv:2306.02465
Endsley, R., Stark, D. P., Whitler, L., et al. 2023, MNRAS, 524, 2312
Enia, A., Talia, M., Pozzi, F., et al. 2022, ApJ, 927, 204
Faisst, A. L., Capak, P. L., Yan, L., et al. 2017, ApJ, 847, 21
Falcón-Barroso, J., Sánchez-Blázquez, P., Vazdekis, A., et al. 2011, A&A, 532, A95
Ferland, G. J., Porter, R. L., van Hoof, P. A. M., et al. 2013, RMxAA, 49, 137
Franco, M., Elbaz, D., Béthermin, M., et al. 2018, A&A, 620, A152
Frayer, D. T., Reddy, N. A., Armus, L., et al. 2004, AJ, 127, 728
Fudamoto, Y., Oesch, P. A., Schouws, S., et al. 2021, Natur, 597, 489
Fujimoto, S., Bezanson, R., Labbe, I., et al. 2023b, arXiv:2309.07834
Fujimoto, S., Kohno, K., Ouchi, M., et al. 2023a, arXiv:2303.01658
Furtak, L. J., Labbé, I., Zitrin, A., et al. 2024, Natur, 628, 57
Furtak, L. J., Zitrin, A., Plat, A., et al. 2023, ApJ, 952, 142
Gardner, J. P., Mather, J. C., Abbott, R., et al. 2023, PASP, 135, 068001
Gáspár, A., Rieke, G. H., Guillard, P., et al. 2021, PASP, 133, 014504
Giavalisco, M., Ferguson, H. C., Koekemoer, A. M., et al. 2004, ApJL, 600, L93
Glazebrook, K., Nanayakkara, T., Jacobs, C., et al. 2023, ApJL, 947, L25
Gómez-Guijarro, C., Elbaz, D., Xiao, M., et al. 2022, A&A, 658, A43
Gottumukkala, R., Barrufet, L., Oesch, P. A., et al. 2024, MNRAS, 530, 966
Greene, J. E., Labbe, I., Goulding, A. D., et al. 2024, ApJ, 964, 39
Gruppioni, C., Béthermin, M., Loiacono, F., et al. 2020, A&A, 643, A8
Hainline, K. N., Helton, J. M., Johnson, B. D., et al. 2024a, ApJ, 964, 66
Hainline, K. N., Johnson, B. D., Robertson, B., et al. 2024b, ApJ, 964, 71
Hainline, K. N., Reines, A. E., Greene, J. E., & Stern, D. 2016, ApJ, 832, 119
Hamann, F., Zakamska, N. L., Ross, N., et al. 2017, MNRAS, 464, 3431
Harikane, Y., Zhang, Y., Nakajima, K., et al. 2023, ApJ, 959, 39
Hatsukade, B., Kohno, K., Yamaguchi, Y., et al. 2018, PASJ, 70, 105
Hodge, J. A., & da Cunha, E. 2020, RSOS, 7, 200556

Hu, E. M., & Ridgway, S. E. 1994, AJ, 107, 1303
Hughes, D. H., Serjeant, S., Dunlop, J., et al. 1998, Natur, 394, 241
Illingworth, G. 2015, Hubble Legacy Fields ("HLF"), STScI/MAST, doi:10.17909/T91019
Illingworth, G., Magee, D., Bouwens, R., et al. 2016, arXiv:1606.00841
Ji, Z., & Giavalisco, M. 2022, ApJ, 935, 120
Ji, Z., Williams, C. C., Tacchella, S., et al. 2023, arXiv:2305.18518
Johnson, B. D., Leja, J., Conroy, C., & Speagle, J. S. 2021, ApJS, 254, 22
Kauffmann, O. B., Le Fèvre, O., Ilbert, O., et al. 2020, A&A, 640, A67
Kemp, T. W., Dunlop, J. S., McLure, R. J., et al. 2019, MNRAS, 486, 3087
Kennicutt, R. C., & Evans, N. J. 2012, ARA&A, 50, 531
Kocevski, D. D., Onoue, M., Inayoshi, K., et al. 2023, ApJL, 954, L4
Kokorev, V., Fujimoto, S., Labbe, I., et al. 2023, ApJL, 957, L7
Koprowski, M. P., Dunlop, J. S., Michałowski, M. J., et al. 2017, MNRAS, 471, 4155
Kroupa, P. 2001, MNRAS, 322, 231
Labbé, I., Greene, J. E., Bezanson, R., et al. 2023a, arXiv:2306.07320
Labbé, I., Huang, J., Franx, M., et al. 2005, ApJL, 624, L81
Labbé, I., Oesch, P. A., Illingworth, G. D., et al. 2015, ApJS, 221, 23
Labbé, I., van Dokkum, P., Nelson, E., et al. 2023b, Natur, 616, 266
Leja, J., Carnall, A. C., Johnson, B. D., Conroy, C., & Speagle, J. S. 2019, ApJ, 876, 3
Leja, J., Johnson, B. D., Conroy, C., van Dokkum, P. G., & Byler, N. 2017, ApJ, 837, 170
Li, Q., Conselice, C. J., Adams, N., et al. 2024, MNRAS, 531, 617
Lo Faro, B., Buat, V., Roehlly, Y., et al. 2017, MNRAS, 472, 1372
Lower, S., Narayanan, D., Leja, J., et al. 2020, ApJ, 904, 33
Lyu, J., Alberts, S., Rieke, G. H., & Rujopakarn, W. 2022, ApJ, 941, 191
Lyu, J., Alberts, S., Rieke, G. H., et al. 2024, ApJ, 966, 229
Lyu, J., & Rieke, G. 2022, Univ, 8, 304
Lyu, J., & Rieke, G. H. 2018, ApJ, 866, 92
Lyu, J., Rieke, G. H., & Alberts, S. 2016, ApJ, 816, 85
Lyu, J., Rieke, G. H., & Shi, Y. 2017, ApJ, 835, 257
Madau, P. 1995, ApJ, 441, 18
Madau, P., & Dickinson, M. 2014, ARA&A, 52, 415
Maiolino, R., Scholtz, J., Curtis-Lake, E., et al. 2023, arXiv:2308.01230
Manning, S. M., Casey, C. M., Zavala, J. A., et al. 2022, ApJ, 925, 23
Marley, M. S., Saumon, D., Visscher, C., et al. 2021, ApJ, 920, 85
Matthee, J., Naidu, R. P., Brammer, G., et al. 2024, ApJ, 963, 129
McKinney, J., Manning, S. M., Cooper, O. R., et al. 2023, ApJ, 956, 72
Murray, S. G., Power, C., & Robotham, A. S. G. 2013, MNRAS, 434, L61
Muzzin, A., Marchesini, D., Stefanon, M., et al. 2013, ApJ, 777, 18
Narayanan, D., Lower, S., Torrey, P., et al. 2024, ApJ, 961, 73
Nelson, E. J., Suess, K. A., Bezanson, R., et al. 2023, ApJL, 948, L18
Nenkova, M., Sirocky, M. M., Ivezić, Ž., & Elitzur, M. 2008a, ApJ, 685, 147
Nenkova, M., Sirocky, M. M., Nikutta, R., Ivezić, Ž., & Elitzur, M. 2008b, ApJ, 685, 160
Noboriguchi, A., Inoue, A. K., Nagao, T., Toba, Y., & Misawa, T. 2023, ApJL, 959, L14
Noboriguchi, A., Nagao, T., Toba, Y., et al. 2019, ApJ, 876, 132
Noboriguchi, A., Nagao, T., Toba, Y., et al. 2022, ApJ, 941, 195
Noll, S., Burgarella, D., Giovannoli, E., et al. 2009, A&A, 507, 1793
Oesch, P. A., Brammer, G., Naidu, R. P., et al. 2023, MNRAS, 525, 2864
Papovich, C., Cole, J. W., Yang, G., et al. 2023, ApJL, 949, L18
Pérez-González, P. G., Barro, G., Annunziatella, M., et al. 2023, ApJL, 946, L16
Perrin, M. D., Long, J., Sivaramakrishnan, A., et al., 2015 WebbPSF: James Webb Space Telescope PSF Simulation Tool, Astrophysics Source Code Library, ascl:1504.007
Perrin, M. D., Sivaramakrishnan, A., Lajoie, C.-P., et al. 2014, Proc. SPIE, 9143, 91433X
Polletta, M., Tajer, M., Maraschi, L., et al. 2007, ApJ, 663, 81
Pope, A., McKinney, J., Kamieneski, P., et al. 2023, ApJL, 951, L46
Pope, A., Montaña, A., Battisti, A., et al. 2017, ApJ, 838, 137
Quadri, R., Marchesini, D., van Dokkum, P., et al. 2007, AJ, 134, 1103
Reines, A. E., Greene, J. E., & Geha, M. 2013, ApJ, 775, 116
Rieke, M., Robertson, B., Tacchella, S., et al. 2023c, Data from the JWST Advanced Deep Extragalactic Survey (JADES) DR2, STScI/MAST, doi:10.17909/Z2GW-MK31
Rieke, M. J., Kelly, D. M., Misselt, K., et al. 2023a, PASP, 135, 028001
Rieke, M. J., Robertson, B. E., Tacchella, S., et al. 2023b, ApJS, 269, 16
Rieke 2024, Systematic Mid-infrared Instrument Legacy Extragalactic Survey (SMILES), MAST, doi:10.17909/et3f-zd57
Rodighiero, G., Bisigello, L., Iani, E., et al. 2023, MNRAS, 518, L19
Ross, N. P., Hamann, F., Zakamska, N. L., et al. 2015, MNRAS, 453, 3932
Sawicki, M. 2002, AJ, 124, 3050
Schreiber, C., Elbaz, D., Pannella, M., et al. 2018, A&A, 609, A30
Shivaei, I., Popping, G., Rieke, G., et al. 2022, ApJ, 928, 68
Shu, X., Yang, L., Liu, D., et al. 2022, ApJ, 926, 155
Simpson, J. M., Swinbank, A. M., Smail, I., et al. 2014, ApJ, 788, 125
Skilling, J. 2004, in AIP Conf. Ser. 735, Bayesian Inference and Maximum Entropy Methods in Science and Engineering: 24th Int. Workshop on Bayesian Inference and Maximum Entropy Methods in Science and Engineering, ed. R. Fischer, R. Preuss, & U. V. Toussaint (Melville, NY: AIP), 395
Smail, I., Dudzeviciute, U., Gurwell, M., et al. 2023, ApJ, 958, 36
Smail, I., Dudzevičiūtė, U., Stach, S. M., et al. 2021, MNRAS, 502, 3426
Sommovigo, L., Ferrara, A., Pallottini, A., et al. 2020, MNRAS, 497, 956
Sommovigo, L., Ferrara, A., Pallottini, A., et al. 2022, MNRAS, 513, 3122
Speagle, J. S. 2020, MNRAS, 493, 3132
Stalevski, M., Fritz, J., Baes, M., Nakos, T., & Popović, L. Č. 2012, MNRAS, 420, 2756
Stalevski, M., Ricci, C., Ueda, Y., et al. 2016, MNRAS, 458, 2288
Steinhardt, C. L., Kokorev, V., Rusakov, V., Garcia, E., & Sneppen, A. 2023, ApJL, 951, L40
Sun, F., Egami, E., Pérez-González, P. G., et al. 2021, ApJ, 922, 114
Tacchella, S., Conroy, C., Faber, S. M., et al. 2022a, ApJ, 926, 134
Tacchella, S., Finkelstein, S. L., Bagley, M., et al. 2022b, ApJ, 927, 170
Talia, M., Cimatti, A., Giulietti, M., et al. 2021, ApJ, 909, 23
Traina, A., Gruppioni, C., Delvecchio, I., et al. 2024, A&A, 681, A118
Umehata, H., Smail, I., Swinbank, A. M., et al. 2020, A&A, 640, L8
Wang, B., Leja, J., Atek, H., et al. 2024, ApJ, 963, 74
Wang, T., Elbaz, D., Schreiber, C., et al. 2016, ApJ, 816, 84
Wang, T., Schreiber, C., Elbaz, D., et al. 2019, Natur, 572, 211
Whitaker, K. E., Ashas, M., Illingworth, G., et al. 2019, ApJS, 244, 16
Whitaker, K. E., Labbé, I., van Dokkum, P. G., et al. 2011, ApJ, 735, 86
Whitler, L., Stark, D. P., Endsley, R., et al. 2023, MNRAS, 519, 5859
Williams, C., Tacchella, S., & Maseda, M. 2023b, Data from the JWST Extragalactic Medium-band Survey (JEMS), STScI/MAST, doi:10.17909/FSC4-DT61
Williams, C. C., Labbe, I., Spilker, J., et al. 2019, ApJ, 884, 154
Williams, C. C., Tacchella, S., Maseda, M. V., et al. 2023a, ApJS, 268, 64
Williams, R. J., Quadri, R. F., Franx, M., van Dokkum, P., & Labbé, I. 2009, ApJ, 691, 1879
Woodrum, C., Rieke, M., Ji, Z., et al. 2023, arXiv:2310.18464
Wright, G. S., Rieke, G. H., Glasse, A., et al. 2023, PASP, 135, 048003
Xiao, M., Oesch, P., Elbaz, D., et al. 2023a, arXiv:2309.02492
Xiao, M. Y., Elbaz, D., Gómez-Guijarro, C., et al. 2023b, A&A, 672, A18
Zavala, J. A., Casey, C. M., Manning, S. M., et al. 2021, ApJ, 909, 165
Zhou, L., Elbaz, D., Franco, M., et al. 2020, A&A, 642, A155